# MID-AMERICA TRANSPORTATION CENTER

UNIVERSITY OF Nebraska Lincoln

THE UNIVERSITY OF IOWA

KU THE UNIVERSITY OF KANSAS

MISSOURI S&T

LINCOLN UNIVERSITY MISSOURI

NICC NEBRASKA INDIAN COMMUNITY COLLEGE

UNIVERSITY OF Nebraska Omaha

University of Nebraska Medical Center

KU MEDICAL CENTER The University of Kansas

# Automated Bridge Inspection using Digital Image Correlation Phase II: Application of Digital Image Correlation Techniques for In-Service Inspection Conditions

## William Collins, PhD, PE
Assistant Professor
Department of Civil, Environmental &
Architectural Engineering
The University of Kansas

## Caroline Bennett, PhD, PE
Professor

## Jian Li, PhD, PE
Associate Professor

## Elaina J. Sutley, PhD
Assistant Professor

## Mary Juno
Research Assistant

## Hayder Al-Salih
Research Assistant

KU THE UNIVERSITY OF KANSAS

2023

MATC

Automated Bridge Inspection using Digital Image Correlation Phase II: Application of Digital Image Correlation Techniques for In-Service Inspection Conditions

William Collins, Ph.D., P.E.
Assistant Professor
CEAE Department
University of Kansas

Elaina J. Sutley, Ph.D.
Assistant Professor
CEAE Department
University of Kansas

Caroline Bennett, Ph.D., P.E.
Professor
CEAE Department
University of Kansas

Mary Juno
Research Assistant
CEAE Department
University of Kansas

Jian Li, Ph.D., P.E.
Associate Professor
CEAE Department
University of Kansas

Hayder Al-Salih
Research Assistant
CEAE Department
University of Kansas

A Report on Research Sponsored by

Mid-America Transportation Center

University of Nebraska–Lincoln

September 2023

# TECHNICAL REPORT DOCUMENTATION PAGE

| 1. Report No.<br>25-1121-0005-151-2 | 2. Government Accession No. | 3. Recipient's Catalog No. |
|---|---|---|
| 4. Title and Subtitle<br>Automated Bridge Inspection using Digital Image Correlation Part II: Application of Digital Image Correlation Techniques for In-Service Inspection Conditions | | 5. Report Date<br>September 2023 |
| | | 6. Performing Organization Code |
| 7. Author(s)<br>William Collins, Ph.D., Caroline Bennett, Ph.D., Jian Li, Ph.D., Elaina Sutley, Ph.D., Mary Juno, Hayder Al-Salih, and Landon Dellenbaugh | | 8. Performing Organization Report No.<br>25-1121-0005-151-2 |
| 9. Performing Organization Name and Address<br>University of Kansas<br>2150 Learned Hall, 1530 W. 15th St. Lawrence, KS 66049 | | 10. Work Unit No. |
| | | 11. Contract or Grant No.<br>69A3551747107 |
| 12. Sponsoring Agency Name and Address<br>Mid-America Transportation Center | | 13. Type of Report and Period Covered<br>Final Report<br>Dec 2017 – Dec 2019 |
| | | 14. Sponsoring Agency Code |

15. Supplementary Notes
Conducted in cooperation with the U.S. Department of Transportation, Federal Highway Administration.

16. Abstract
A major concern for aging steel bridges in the United States is the initiation and propagation of distortion-induced fatigue cracks, which accounts for the majority of fatigue cracks in bridges. Despite recent studies proving that visual inspections consistently fail to identify realistically sized fatigue cracks, Departments of Transportation are forced to rely primarily on the use of visual inspections to locate and characterize fatigue cracking. Many detection methodologies have been examined for fatigue crack detection, but the methods are dependent on detection equipment that is physically attached to the bridge, such as sensor networks, which limits the flexibility of the methods for analyzing the multiple fatigue susceptible regions present on highway bridges. The development of an inspection technique that is not dependent on human visual inspection or physical attachments would have the potential to decrease the time and cost of performing inspections, as well as decrease the risk of injury to inspectors and increase reliability.

The efficacy of vision-based technologies as an alternative to manual inspections of highway bridges is an area of active research. While many vision-based technologies have been proven to detect macro-indicators of damage, digital image correlation (DIC) has shown potential for detecting and characterizing fatigue cracks. Since DIC measurements have the ability to capture full-field displacements and surface strains, it is proven that developed DIC methodologies have the ability to identify and characterize both in-plane and out-of-plane fatigue cracks, allowing application to steel bridges exposed to differential girder displacement. This report summarizes the development of a crack-detection methodology using DIC and aims to quantify the impact of lighting and focus on the developed methodology. An evaluation of seven open-source DIC alternatives is also presented, as the use of free open-source software has the potential to reduce initial costs and allow for modifications that are tailored to the specific needs of bridge inspections.

| 17. Key Words<br>Fatigue, cracking, bridge, steel, inspection, digital image correlation | 18. Distribution Statement<br>No restrictions. This document is available through the National Technical Information Service, Springfield, VA 22161. | | |
|---|---|---|---|
| 19. Security Classif. (of this report) | 20. Security Classif. (of this page) | 21. No. of Pages<br>78 | 22. Price |

Form DOT F 1700.7 (8-72)      Reproduction of completed page authorized

<p style="text-align: center">Table of Contents</p>

## List of Figures

Disclaimer

The contents of this report reflect the views of the authors, who are responsible for the facts and the accuracy of the information presented herein. This document is disseminated in the interest of information exchange. The report is funded, partially or entirely, by a grant from the U.S. Department of Transportation's University Transportation Centers Program. However, the U.S. Government assumes no liability for the contents or use thereof.

Abstract

A major concern for aging steel bridges in the United States is the initiation and propagation of distortion-induced fatigue cracks, which accounts for the majority of fatigue cracks in bridges. Despite recent studies proving that visual inspections consistently fail to identify realistically sized fatigue cracks, Departments of Transportation are forced to rely primarily on the use of visual inspections to locate and characterize fatigue cracking. Many detection methodologies have been examined for fatigue crack detection, but the methods are dependent on detection equipment that is physically attached to the bridge, such as sensor networks, which limits the flexibility of the methods for analyzing the multiple fatigue susceptible regions present on highway bridges. The development of an inspection technique that is not dependent on human visual inspection or physical attachments would have the potential to decrease the time and cost of performing inspections, as well as decrease the risk of injury to inspectors and increase reliability.

The efficacy of vision-based technologies as an alternative to manual inspections of highway bridges is an area of active research. While many vision-based technologies have been proven to detect macro-indicators of damage, digital image correlation (DIC) has shown potential for detecting and characterizing fatigue cracks. Since DIC measurements have the ability to capture full-field displacements and surface strains, it is proven that developed DIC methodologies have the ability to identify and characterize both in-plane and out-of-plane fatigue cracks, allowing application to steel bridges exposed to differential girder displacement. This report summarizes the development of a crack-detection methodology using DIC and aims to quantify the impact of lighting and focus on the developed methodology. An evaluation of seven open-source DIC alternatives is also presented, as the use of free open-source software has the

potential to reduce initial costs and allow for modifications that are tailored to the specific needs

of bridge inspections.

Chapter 1 Digital Image Correlation Background

1.1 Introduction

Bridges are vital to the movement of goods and people across the country but are prone to damage and deterioration from repetitive loads over their long service life. In their most recent Infrastructure Report Card, the American Society of Civil Engineers gave bridges in the United States a grade of C+ and found that over 9 percent of bridges are considered structurally deficient (ASCE 2017). Identifying and repairing potential issues is vital to properly maintaining bridges and ensuring that they remain in-service for at least the entirety of their intended service life.

One of the major issues impacting older steel bridges is the initiation and propagation of fatigue cracks (Fisher 1984), specifically distortion-induced fatigue cracks, which account for almost 90% of fatigue cracks in aging steel bridges in the United States (Connor and Fisher 2006). Steel bridges built prior to the 1980s in the United States were regularly designed without a connection between the flanges and connection plate, which can increase the rate of initiation for distortion-induced fatigue cracks (Zhao and Roddis 2004). When a bridge with this detail experiences traffic loads, the girders are subjected to differential deflection. The differential deflection can allow the cross-frame to push or pull on the girder web which causes out-of-plane stresses to be applied to the weak web gap region, resulting in distortion-induced fatigue cracks.

To minimize the potential impact of distortion-induced fatigue cracking, bridges are required to be repaired or retrofitted based on the findings of regular inspections. Bridge inspections are typically performed on a 24-month cycle (FHWA 2004), and the most common method for fatigue crack detection is through visual inspection. Fatigue cracks are caused by cyclic traffic loads, and they are initially very small and challenging to detect through visual inspection. When cracks go undetected, however, they have the potential to propagate to a

critical size, which could compromise a bridge's structural integrity. Although bridge inspections are necessary to ensure the safety of bridge infrastructure, visual inspections have significant monetary and time costs, as well as present safety risks to both inspectors and the travelling public. Additionally, the identification of realistic fatigue cracks has been proven to be extremely difficult and inconsistent (Campbell et al. 2020; Whitehead 2015; Zhao and Haldar 1996).

Technologies to detect and monitor cracking has been evaluated by researchers interested in structural health monitoring (SHM) and non-destructive testing (NDT). While sensing technologies have been used successfully to detect and monitor both in- and out-of-plane cracks, many of these approaches require the use of sensors or other components that physically attach to a particular location on a bridge, preventing these methodologies from effectively monitoring the various regions of fatigue susceptibility on steel bridges. The development of a computer vision-based detection methodology that would operate without depending on a physical attachment would allow large sections of steel bridges to be surveyed safely and efficiently.

Some research has been performed on vision-based crack detection methodologies, but the majority of testing conducted was under highly idealized conditions that only evaluated in-plane fatigue loading or non-metallic materials (Vanlanduit et al. 2009; Rupil et al. 2011; Nowell et al. 2010). Very few research programs have evaluated vision-based crack detection methods on out-of-plane fatigue loading or with the complex geometries commonly found on steel highway bridges. A vision-based crack detection methodology that utilizes digital image correlation (DIC) is being evaluated for performance on both ideal and non-ideal in-plane lab setups and out-of-plane test setups with complex geometry and distortion-induced fatigue cracking.

1.2 Digital Image Correlation Methodology

*1.2.1 Computer Vision*

Computer vision refers to the branch of technology that utilizes computer algorithms and optics to collect information from pictures and videos. Researchers in engineering and material sciences have evaluated the use of computer vision for different applications, particularly to characterize mechanical parameters. The ability of computer vision to detect cracks has been evaluated by many researchers using a variety of materials. Edge detection methodologies have been proven to be able to successfully identify edge-like features on digital images, allowing for detection and localization of cracks in concrete surfaces (Abdel-Qader et al. 2003). Due to inadvertent detection of corrosion, surface textures, component boundaries, and defects, edge detection in metallic materials continues to have a high rate of false positives (Yeum and Dyke 2015).

Research has been conducted to develop algorithms that could remove thick, short, or exceedingly linear edges that are typically not created by cracking, with the goal of creating a reliable crack detection methodology (Yu et al. 2007). Complex algorithms for detecting cracking in asphalt and concrete pavements have been developed by other researchers (Yamaguchi and Hashimoto 2010; Zou et al. 2012; Cha et al. 2017). Typically, asphalt and concrete pavements have larger crack openings than metallic materials, as well as higher contrast between cracked and uncracked regions, meaning that the application of edge detection methodologies to steel bridges is challenging. Additionally, most computer vision studies focus on macro-indicators of damage, such as extensive corrosion, concrete deck deterioration, and large displacements caused by substructure movement. A computer vision strategy to detect

3

fatigue cracks through the tracking of structural surface motion in a video has been developed,

but crack tip identification remains a challenge (Kong and Li 2018).

*1.2.2 Digital Image Correlation Background*

DIC is a subset of computer vision that utilizes medium- to high-resolution cameras and

post-processing computer software to analyze images and outputs full-field surface

displacement. A three-dimensional strain field can be developed from the full-field surface

displacement. DIC software is capable of analyzing both two- and three-dimensional data,

depending on how many cameras are utilized during testing. DIC compares a series of images

that are collected during loading and generates relative strain and displacement for each point on

the image. DIC has been proven to have potential for detecting and characterizing fatigue cracks,

but the majority of testing has been limited to simplified test setups, such as in-plane loading or

simple geometry.

DIC has been used in the place of tradition sensing methods, such as strain gauges and

extensometers, to determine both strain and deformation (Yuan et al. 2014). Crack detection

using DIC has been applied to crack detection in a concrete structure (Küntz et al. 2006) and in

the calculation of stress intensity factors (Zhang and He 2012; Hamam et al. 2007). The

applications and limitations of 3D DIC have been evaluated using simplified test setups since the

mid-1990s (Helm 1996). Test setups with four cameras have been used to determine out-of-plane

displacements, but additional cameras result in challenges with the experimental setup and

calibration (Chen et al. 2013). A stereoscopic camera setup with a high shutter speed has been

used to measure full-field out-of-plane vibrations, but the use of high-speed cameras resulted in a

lack of image resolution (Helfrick et al. 2011). Some complex loading scenarios have been tested

using clevis fixtures to generate mixed mode loading on compact (C(T)) test specimens. For

Mode I (opening) and Mode II (in-plane shear) loading, DIC displacement results agreed with results developed using a finite element analysis of the crack (Sutton et al. 2007).

DIC has been used to evaluate in-plane displacements for a variety of civil infrastructure. A primary application of DIC is to measure deflections of critical bridge members when subjected to service loading. Bridge deflection has been measured from digital videos through a combination of DIC and an inverse compositional algorithm (Pan et al. 2016). This methodology was validated by testing an in-service railway bridge. An advanced DIC system was used to investigate the deflections of two historic masonry arch bridges under service loads (Dhanasekar et al. 2018). Similar work was performed by Cigada et al. (2014) and Alipour et al. (2019). 3D-DIC has also been used with an unmanned aerial vehicle to examine surface cracking on a concrete bridge (Reagan et al. 2018). While there have been successful applications of DIC for evaluating deflections of in-service structures, challenges to field deployment have been identified, particularly lighting conditions (Ribeiro et al. 2014) and limitations on how large of a distance there is between the camera and the material surface (Lee and Shinozuka 2006).

Extensive research has been performed on applications of DIC for identifying fatigue cracks in metallic materials, but the research has primarily been conducted in an idealized laboratory setting. Studies have examined in-plane fatigue cracking with the goal of identifying and characterizing cracks. In-plane loading studies have been performed on steel C(T) specimens (Rupil et al. 2011), aluminum channels (Vanlanduit et al. 2008), notched tension specimens (Carrol et al. 2009; Carrol et al. 2012), and tension plates with center drilled bolt holes (Lorenzino et al. 2014; Hutt and Cawley 2009). These studies have contributed to understanding the limitations and abilities of DIC for crack detection. Most of these studies, however, focus on qualitative crack identification and characterization, and the development of a

quantifiable methodology for automated steel bridge inspections has only been minimally investigated. Additionally, out-of-plane loading conditions have not been as thoroughly researched as in-plane fatigue loading. This is likely due to the complexity of the test setup required for out-of-plane fatigue loading (Sutton et al. 2007). Work was performed to begin to evaluate how DIC works for complex, out-of-plane test setups, and initial testing found that the developed methodology had the ability to detect and predict the length of distortion-induced fatigue cracks (Dellenbaugh et al. 2020).

*1.2.3 Digital Image Correlation Setup*

In theory, accurate DIC results are dependent on the specimen preparation, camera setup, calibration, and image collection. The preparation of the specimen primarily refers to the application of a speckle pattern. The ideal pattern is made of consistent dot sizes that are high contrast and random. The speckle pattern is what provides points of reference for the DIC software. Without a speckle pattern, images cannot be compared to evaluate the movement of the specimen. The camera setup depends on the test specimen's complexity and whether two- or three- dimensional analysis is desired. For two-dimensional analysis, one camera will suffice, since no out-of-plane deformations are expected, which allows for a simplified test setup and easier calibration. When testing for out-of-plane displacements, two or more cameras are needed to capture the three-dimensional strain field. Calibration is the process of converting the images from pixels to real dimensions, ensuring realistic evaluation of the specimen. Additionally, calibration accounts for the location of the cameras relative to one another in test setups with two or more cameras. After calibrating, images are collected at a constant interval while the test specimen is being loaded. These images are analyzed using DIC software to determine full-field displacements and stresses.

Chapter 2 Year One Overview

<u>2.1 Initial In-Plane Testing</u>

*2.1.1 Initial Testing and Methodology Development*

To develop an automated fatigue crack inspection methodology, a method for quantifying

cracking was needed. The initial methodology was developed using a DIC test setup with a

single camera and a C(T) specimen subjected to in-plane loading in a servo-hydraulic testing

machine. The C(T) specimen tested was 6.35 mm (0.25 in.) thick and 127 mm (5.0 in.) wide. The

specimen size was chosen such that a single specimen could accommodate extensive crack

growth and testing at multiple crack lengths. Since bridges are subjected to highly variable

loadings, multiple load cases were defined for testing on the C(T) specimen. Stress intensity

ranges of 11, 22, 33, 44, and 55 MPa$\sqrt{}$m (10, 20, 30, 40, and 50 ksi$\sqrt{}$in) were chosen to emulate

realistic bridge loading, and the stress intensity ranges were tested from lowest to highest to limit

crack tip plasticity during testing. Images for DIC processing were collected for each loading

case at crack lengths of 12.7, 25.4, 38.1, and 50.8 mm (0.5, 1.0, 1.5, and 2.0 in.). The general

location of the crack was identifiable through visual inspection of the DIC results, but a

methodology to determine the crack length from the DIC data was developed to move towards

automation. The twenty data sets for in-plane testing were used to develop a crack length

quantification methodology.

*2.1.2 Crack Characterization Methodology*

Original testing was performed on a C(T) specimen to ensure that the crack location was

easily identified. Using the known crack path, the coordinates of the crack path were extended

beyond the crack tip, assuming that crack growth would continue linearly. After identifying the

crack path, inspection lines were plotted orthogonal to the crack path at consistent intervals along

the crack path and projected crack path. From each orthogonal inspection line, two hundred data points were extracted to determine the relative displacement between the two sides of the crack. The difference between the displacement on either side of the crack was defined as the relative displacement. Relative displacements were plotted along the length of the crack path, and the best fit line for each side of the crack was determined using an algorithm. The relative displacement for each point along the crack path, $\Delta_i$, was divided by the maximum relative displacement for the data set, $\Delta_{max}$. Convergence of the crack was defined as the difference between 100% and the ratio of relative to maximum displacement, shown below as

$$Convergence = 100\% - \frac{\Delta_i}{\Delta_{max}}. \tag{2.1}$$

Theoretically, convergence should equal 100% at the crack tip as there is no relative displacement on either side of the crack, while at the crack opening where relative displacement is the greatest, compliance should equal 0%. However, initial results indicated this was rarely true, likely due to non-ideal testing conditions such as speckle pattern and image resolution. Initial testing showed that the crack tip was located at a convergence between 90% and 95%. This was then tested in an out-of-plane test setup to determine the accuracy and efficacy of the developed methodology.

2.2 Initial Distortion-Induced Fatigue Testing

*2.2.1 Distortion-Induced Fatigue Test Setup and Loading*

After the crack characterization methodology was developed using a simplified in-plane C(T) specimen, the methodology was evaluated on a crack developed on a half-scale girder-to-cross-frame subassembly. The test specimen was an I-shaped plate girder sub-assembly

fabricated from A36 steel. The half-scale girder had a length of 2845 mm (112 in.), a depth of 917 mm (36.1 in.), and a web thickness of 10 mm (0.375 in.). To approximate the axial stiffness provided by the concrete deck attached to the top flange of a girder, the top of the girder sub-assembly was connected to the reaction floor of the laboratory, which prevented the top flange from experiencing out-of-plane motion. A cross-frame was installed at the mid-span of the girder, which was attached through a connection plate welded only to the girder web.

The girder was loaded out-of-plane by applying a vertical displacement to the far end of the cross-frame, producing a distortion-induced fatigue crack. Fatigue cracking was initiated in the web-gap region between the connection plate and the flange. A fatigue crack was initiated and propagated on the girder through loading for 21,000 cycles at a load range of 2.2 to 25.5 kN (0.5 to 5.75 kips). This crack spanned between the connection plate weld and the girder web and contained two vertical segments connected by a short diagonal segment, all of which were idealized as linear. The crack was measured to have a total length of 44.5 mm (1.75 in.).

A loading protocol was developed for the out-of-plane testing to have varying and realistic loads that simulate the varying traffic loads that bridges are subjected to. Realistic loading levels were determined using a finite element model of a bridge based on the full-scale proportions of the testing setup. Realistic differential vertical deflections between adjacent girders were determined by applying the AASHTO fatigue truck. On the full-scale finite element model, the differential deflection was 2.54 mm (0.1 in.), so the target differential deflection for the half-scale test setup was 1.25 mm (0.05 in.), which corresponds to an actuator load of 6.6 kN (1.5 kips) applied to the end of the cross-frame. Seven load cases were defined for loads above and below the target load. All loading cases had a minimum applied load of 0.89 kN (0.2 kip) to

simulate the dead load of the bridge, and the load cases had a maximum applied load of 2.2, 4.4, 6.7, 8.9, 11.1, 13.3, and 15.6 kN (0.5, 1.0, 1.5, 2.0, 2.5, 3.0, and 3.5 kips).

*2.2.2 Distortion-Induced Fatigue DIC Configuration*

The main difference between the DIC configuration for in-plane C(T) testing and distortion-induced fatigue testing is that out-of-plane testing requires the use of a two-camera stereo setup, rather than a single camera (see fig. 2.1a and b). A speckle pattern was applied to the fatigue susceptible region to provide reference points for the DIC processing (see fig. 2.1c). For the purpose of processing the DIC data, the web-to-flange weld was defined as the x-axis, the stiffener-to-web weld was established as the y-axis, and the z-axis was located along the direction of the cross-frame.
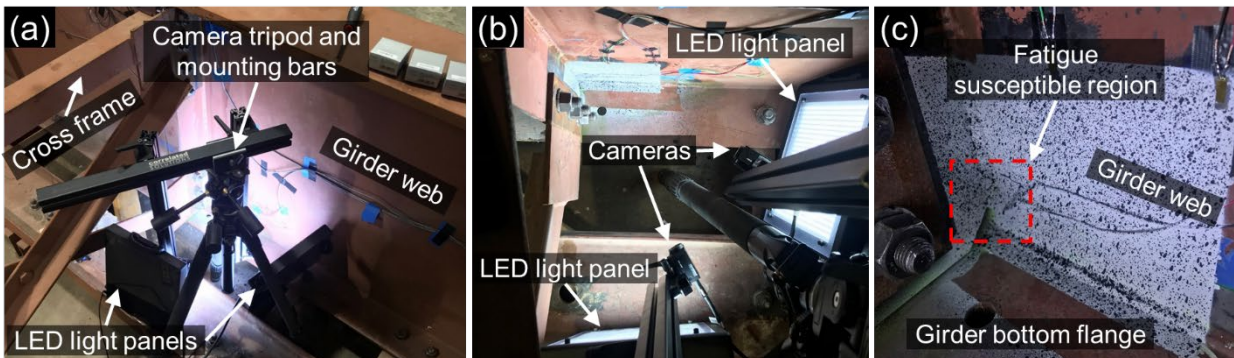


Figure 2.1 (a) Hardware locations for out-of-plane testing, (b) hardware orientation as seen from above, and (c) fatigue susceptible region with speckle pattern applied

*2.2.3 Distortion-Induced Fatigue Crack Characterization Methodology*

The same methodology was used to analyze distortion-induced fatigue specimens as the in-plane specimens. For the initial analysis of distortion-induced fatigue cracks, the displacement values along the z-axis were used to determine convergence. Despite the more complicated geometry, the crack path could be determined through visual inspection of the DIC displacement

contours. Orthogonal lines were drawn along the length of the crack in the web gap region. The relative displacements were determined for the entire length of the crack and extended beyond the crack tip. Convergence was calculated for the out-of-plane crack in the same manner as the in-plane crack using equation 2.1.

The relative displacements for the load case ranging from 0.89 to 2.2 kN (0.2 to 0.5 kip) were very small for the entirety of the crack length, which resulted in large variations in convergence. The high variability of the convergence indicates that the developed methodology is not applicable at low load levels. This applicability threshold will need to be investigated further in future testing.

Because the C(T) specimen testing resulted in typical convergences of 90% to 95%, the known crack length for the distortion-induced fatigue specimen was compared to the 90% and 95% convergence values to determine the accuracy of the developed DIC results. The optically measured crack length was 44.5 mm (1.75 in.). The 90% convergence values tended to under-predict the crack length. On average, the 90% convergence value corresponded to a 40.6 mm (1.59 in.) crack, which is 9% lower than the actual crack. The 95% convergence tended to over-predict the crack length, but only by an average of 1%, corresponding to a predicted crack length of 45.0 mm (1.77 in.). This indicated that the developed methodology for crack length determination was accurate for simple out-of-plane cracks.

Chapter 3 In-Plane Light, Focus, and Aperture Testing

3.1 In-Plane C(T) Test Setup

*3.1.1 Lighting and Focus Background*

The accuracy of DIC output is dependent on the preparation of the specimen, camera setup, calibration, and image collection. Work performed during year one was primarily proof-of-concept and was applied under idealized conditions. For DIC to be implementable in the field, the system and methodology needs to be robust enough to handle the varying conditions found on in-service structures. The objective of this study was to evaluate the ability of the developed DIC methodology to characterize an in-plane crack under non-idealized lighting and camera focus conditions.

*3.1.2 Test Setup and Loading*

Light and focus testing was performed on steel C(T) specimens loaded in a uniaxial servo-hydraulic loading frame. Testing was performed in a similar manner to the testing that developed the in-plane methodology. Images were collected during loading using a PGR Grasshopper3 camera with a 17 mm (0.67 in.) lens mounted on an adjustable tripod. External adjustable LED lighting panels were used to control lighting on the steel C(T) specimen. High contrast was ensured on the specimen by coating the surface with white paint and then applying black spray paint in a random speckle pattern that covered approximately one third of the specimen surface.

The C(T) specimen was 6.35 mm (0.25 in.) thick with a width of 127 mm (5.0 in.). The fatigue crack investigated had four different crack lengths of 12.7, 25.4, 38.1, and 50.8 mm (0.5, 1.0, 1.5, and 2.0 in.), as measured from the end of the machined notch. To emulate the variability of highway bridge loadings, five load cases were defined and cyclically applied to achieve stress

intensity ranges of 11, 16, 22, 27, and 33 MPa√m (10, 15, 20, 25, and 30 ksi√in). These loading cases are respectively designated LC1 through LC5. The five load cases were modified from year one testing to limit plasticity at the crack tip and to provide a more realistic loading range.

*3.1.3 Lighting and Focus Conditions*

Lighting conditions were controlled using two adjustable LED lighting panels. Camera focus was controlled through physically moving the camera further from or closer to the specimen to increase or decrease the focal length. The different light and focus conditions were evaluated using the DIC software and a built-in uncertainty estimate. Three lighting conditions and three focus conditions were defined and combinations of each were tested at three nominal camera-to-specimen spacings.

The three lighting conditions were chosen to represent high, medium, and low light conditions. High light was the brightest, achieved when the two LED lamps were set to maximum brightness, measuring up to 6600 lumen on the specimen surface. This created an overexposed image with a washed-out speckle pattern. Medium light and low light were recorded at approximately 4600 and 2000 lumen, or 70% and 30% of the high light condition, respectively. Ideal lighting occurs at approximately 85% of the high light condition, 5600 lumen, meaning that all lighting conditions were non-ideal. Due to interference and reflection from the test setup and the DIC equipment, light on the specimen surface varied, especially for sections with shadows cast by the clevises. To account for this variation, a lumen range for each lighting condition was determined. Minimum and maximum light readings on the surface of the specimen were collected before testing to ensure that the lighting was within an adequate range. The lumen ranges for each lighting condition are shown in Table 3.1.

During the development of the crack characterization methodology, the camera was located 216 mm (8.5 in.) from the surface of the specimen. Two additional camera distances, 432 and 648 mm (17.0 and 25.5 in.), were evaluated in this study. At each of the three camera distances, the ideal focus and two additional levels of focus resulting in a 5% and 10% reduction from the ideal focus, respectively, were chosen for testing. Using the uncertainty estimate from the DIC software, ideal focus was defined as having an uncertainty of 0.0003 mm (0.00001 in.) or better under the high lighting condition. Focus was initially varied by manually adjusting the rotation of the camera's focus ring. However, the focus ring used does not measure rotation, therefore an alternative definition for quantifying focus was developed. Focus was redefined in terms of camera distance from the specimen. By first focusing the camera at the ideal distances of 216, 432, and 648 mm (8.5, 17.0, and 25.5 in.), the camera was then moved closer to the specimen, reducing the focal length by 5% and 10% to create the fair and poor focus conditions, respectively. The uncertainty estimates for the fair and poor focus conditions were 0.0007 and 0.0010 mm (0.00003 and 0.00004 in.), respectively.

Six combinations of lighting and focus conditions were evaluated for each of the three camera distances for in-plane crack lengths of 12.7, 25.4, 38.1, and 50.8 mm (0.5, 1.0, 1.5, and 2.0 in.). For the first three conditions, the camera was kept at the primary distance of 216, 432, or 648 mm (8.5, 17.0, or 25.5 in.) from the specimen while the lighting varied between the high, medium, and low light conditions. Conditions 4 and 5 had fair focus at a camera distance of 205, 410, or 615 mm (8.1, 16.2, or 24.2 in.) and evaluated the high and medium light levels. Data obtained in the fair focus, low light combination was not able to be post-processed with the DIC software. The poor focus condition utilizing a camera distance of 195, 389, or 583 mm (7.7, 15.3, or 22.9 in.) was only evaluated using the high light condition. The low and medium light

14

conditions with poor focus provided data that was unable to be post-processed using DIC

software. This indicates that if focus is not ideal, the lighting must be at or above ideal levels. All

six of the condition combinations evaluated are sub-optimal, ignoring the recommended

calibration needs of the DIC system. The lighting and focus conditions for the 648 mm (25.5 in.)

primary camera distance are summarized in Table 3.1. The lighting and focus conditions for

primary camera distances of 216 and 432 mm (8.5 and 17.0 in.) are shown in Appendix A.

Table 3.1 Light and focus conditions for 648 mm (25.5 in.) camera distance

| Condition | Focus | Focal Length, mm (in.) | Lighting | Light Range, lumens |
|---|---|---|---|---|
| 1 | Ideal | 648 (25.5) | High | 5850 – 6600 |
| 2 | Ideal | 648 (25.5) | Medium | 4450 – 5000 |
| 3 | Ideal | 648 (25.5) | Low | 2000 – 2350 |
| 4 | Fair | 615 (24.2) | High | 5850 – 6600 |
| 5 | Fair | 615 (24.2) | Medium | 4450 – 5000 |
| 6 | Poor | 583 (22.9) | High | 5850 – 6600 |

3.2 Lighting and Focus Testing Results

*3.2.1 Camera to Specimen Distance of 648 mm (25.5 in.)*

DIC data for the primary camera distance of 648 mm (25.5 in.) was collected for crack

lengths of 12.7, 25.4, 38.1, and 50.8 mm (0.5, 1.0, 1.5, and 2.0 in.) under the five specified load

cases and the six lighting and focus conditions. Typical outputs from the DIC software for LC5

with a crack length of 25.4 mm (1.0 in.) are shown in Figures 3.1 and 3.2, showing conditions 1

and 5, respectively.
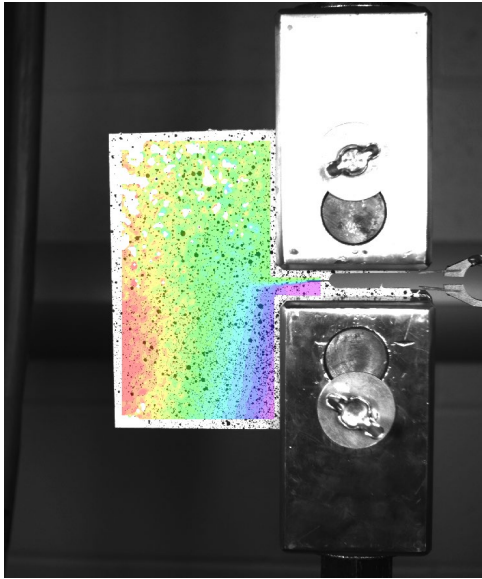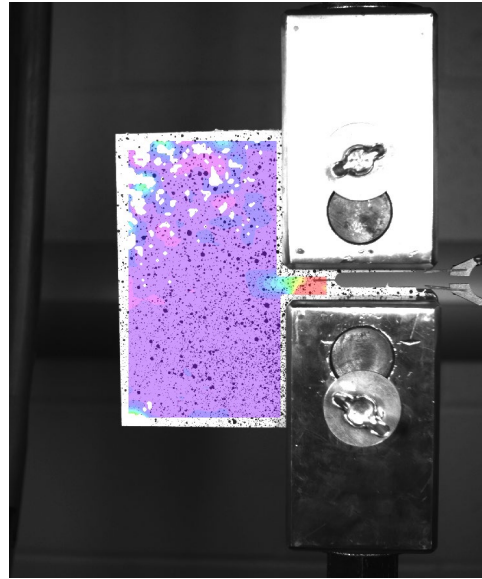
(a)            (b)

Figure 3.1 DIC results for a 25.4 mm (1.0 in.) crack with 648 mm (25.5 in.) camera distance under LC5 and Condition 1 in terms of (a) displacement and (b) strain
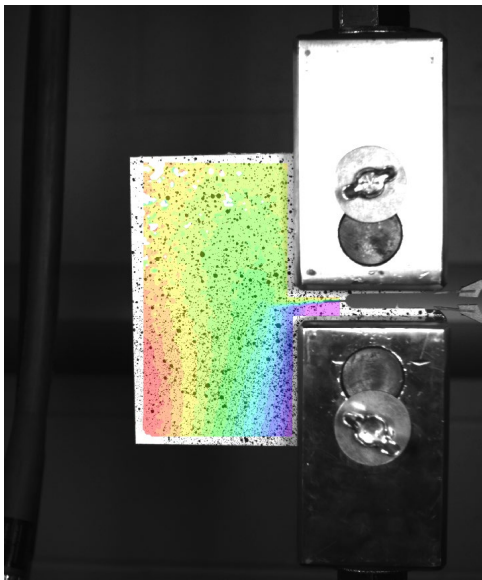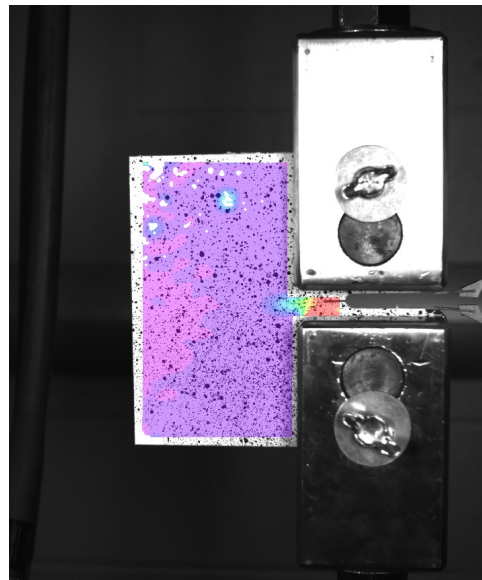


(a)            (b)

Figure 3.2 DIC results for a 25.4 mm (1.0 in.) crack with 648 mm (25.5 in.) camera distance under LC5 and Condition 5 in terms of (a) displacement and (b) strain

The expected deflections for C(T) specimens are exclusively in-plane, so relative displacements perpendicular to the crack path were utilized in accordance with the developed crack characterization methodology to calculate the convergence. Due to the distance between the camera and the specimen, the crack was not clearly visible in the DIC strain and displacement data images. Representative relative displacement and convergence values are shown in Figures 3.3 and 3.4 for LC5. In each plot, the vertical dotted line represents the actual crack length, as verified through specimen compliance and visual observation. Convergence plots for additional crack lengths and load cases are shown in Appendix A. The high, medium, and low light conditions are denoted using HL, ML, and LL, respectively, while the ideal, fair, and poor focus conditions are denoted by IF, FF, and PF, respectively. Thus, the first condition combining high light and ideal focus is termed HLIF.
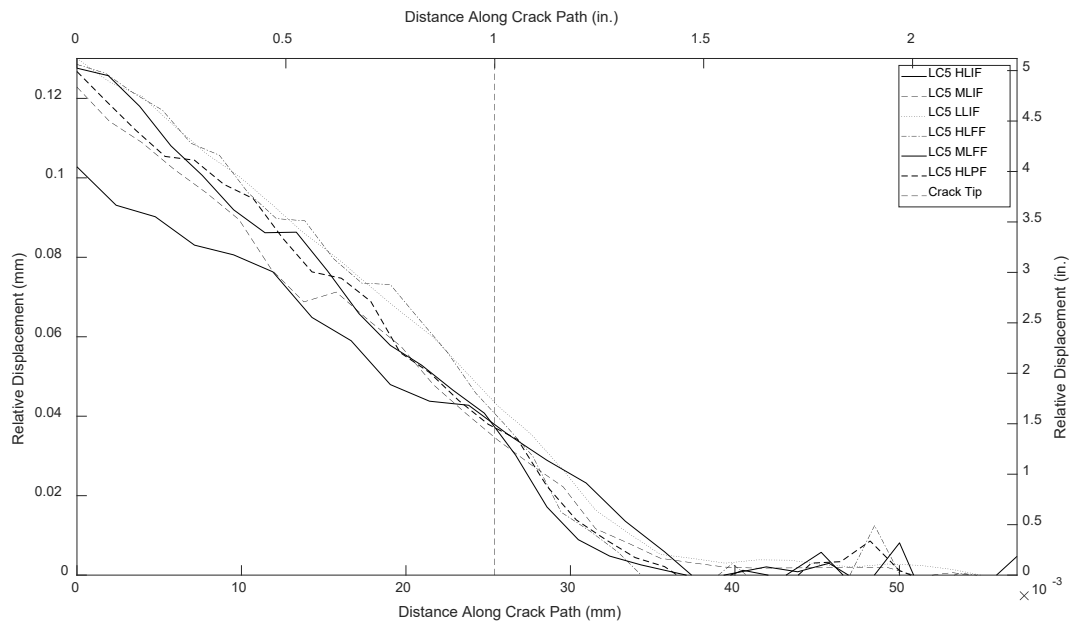


Figure 3.3 Relative displacement of a 25.4 mm (1.0 in.) crack under LC5
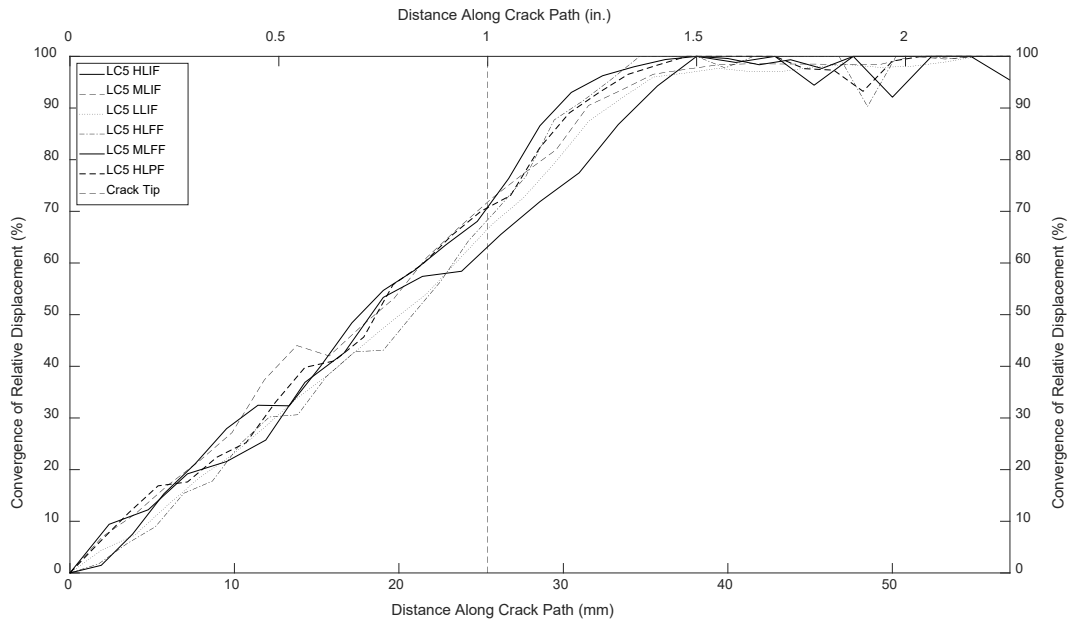
Figure 3.4 Convergence of relative displacement of a 25.4 mm (1.0 in.) crack under LC5

Convergence values for each lighting and focus condition combination were averaged across all five load cases for a crack length of 25.4 mm (1.0 in.) and are compared to the ideal case in Table 3.2. The convergence for each condition and load case is shown visually in Figure 3.5. Because of the modified loading cases from the initial methodology development, the non-ideal cases can only be directly compared with the ideal results for load cases 1, 3, and 5. The lines are presented for clarity.

Table 3.2 Average convergence at 25.4 mm (1.0 in.) crack
tip for 648 mm (25.5 in.) camera distance

| Light and Focus Condition | Average Convergence | Difference |
|---|---|---|
| Ideal | 92.6% | N/A |
| 1 | 71.5% | 21.1% |
| 2 | 72.3% | 20.3% |
| 3 | 69.6% | 23.0% |
| 4 | 73.3% | 19.3% |
| 5 | 66.2% | 26.4% |
| 6 | 73.1% | 19.5% |
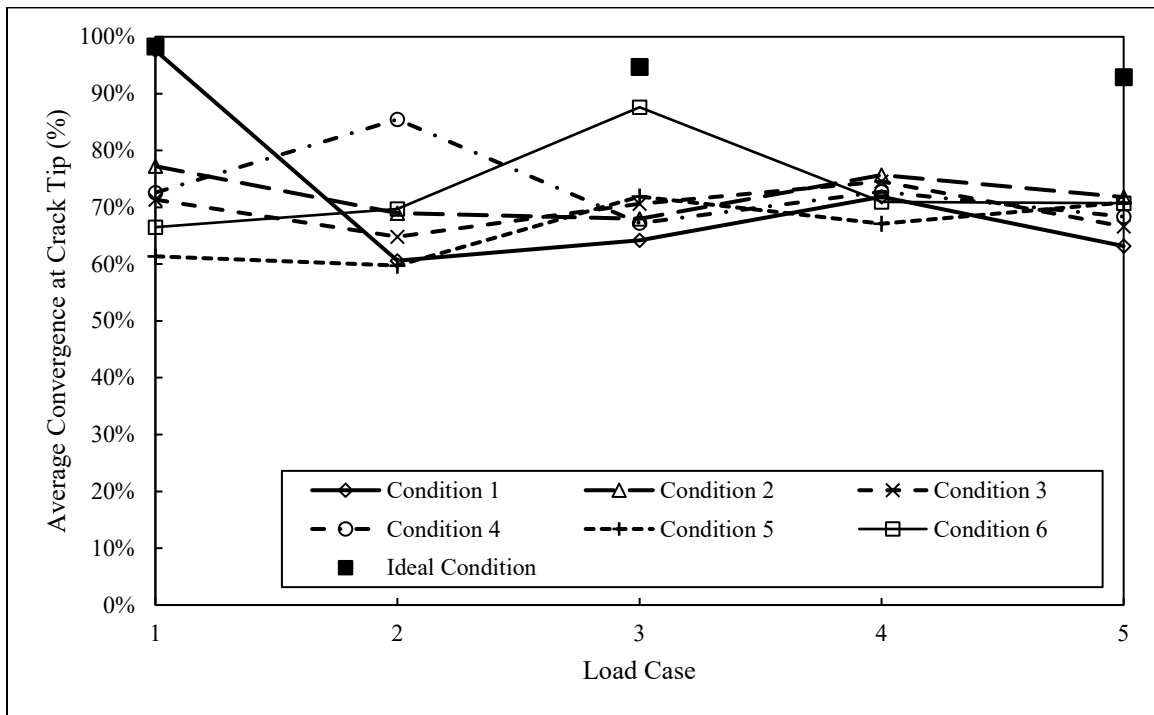


Figure 3.5 Average convergence at crack tip for each load case and condition for a 25.4 mm (1.0 in.) crack with a camera distance of 648 mm (25.5 in.)

Convergence values for non-ideal conditions exhibit a significant increase in variability compared to the results from the ideal test conditions. Each of the six lighting and focus conditions were sub-optimal, and this resulted in an average decrease in calculated convergence

at the crack tip of 21.6% for the 25.4 mm (1.0 in.) crack. While the non-ideal conditions resulted

in a significant decrease in crack convergence and DIC output quality, the presence of a crack

was still detected. This indicates that sub-optimal conditions may not result in accurate crack

length measurements, but can be used to detect cracks and flag them for further inspection.

Similar results were seen for 12.7, 25.4, 38.1, and 50.8 mm (0.5, 1.0, 1.5, and 2.0 in.) crack

lengths, as shown in Tables 3.3, 3.4, and 3.5, respectively.

Table 3.3 Average convergence at 12.7 mm (0.5 in.) crack
tip for 648 mm (25.5 in.) camera distance

| Light and Focus Condition | Average Convergence | Difference |
|---|---|---|
| Ideal | 75.0% | N/A |
| 1 | 50.6% | 24.4% |
| 2 | 49.5% | 25.5% |
| 3 | 61.5% | 13.5% |
| 4 | 49.1% | 25.9% |
| 5 | 52.4% | 22.6% |
| 6 | 49.4% | 25.6% |

Table 3.4 Average convergence at 38.1 mm (1.5 in.) crack
tip for 648 mm (25.5 in.) camera distance

| Light and Focus Condition | Average Convergence | Difference |
|---|---|---|
| Ideal | 94.9% | N/A |
| 1 | 68.3% | 26.6% |
| 2 | 72.5% | 22.4% |
| 3 | 71.7% | 23.2% |
| 4 | 72.9% | 22.0% |
| 5 | 73.6% | 21.3% |
| 6 | 71.8% | 23.1% |

Table 3.5 Average convergence at 50.8 mm (2.0 in.) crack
tip for 648 mm (25.5 in.) camera distance

| Light and Focus Condition | Average Convergence | Difference |
|---|---|---|
| Ideal | 98.2% | N/A |
| 1 | 75.7% | 22.5% |
| 2 | 78.8% | 19.4% |
| 3 | 76.3% | 21.9% |
| 4 | 73.1% | 25.1% |
| 5 | 75.4% | 22.8% |
| 6 | 72.0% | 26.2% |

*3.2.2 Camera to Specimen Distance of 432 mm (17.0 in.)*

DIC data for the primary camera distance of 432 mm (17.0 in.) was collected for crack

lengths of 12.7 and 25.4 mm (0.5 and 1.0 in.) under the five specified load cases and the six

lighting and focus conditions. Typical outputs from the DIC software for LC5 with a crack

length of 25.4 mm (1.0 in.) are shown in Figures 3.6 and 3.7, showing conditions 1 and 5,

respectively.
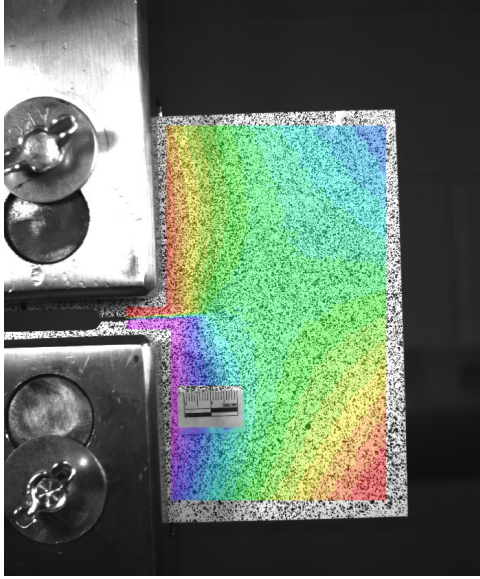
<center>(a)</center>
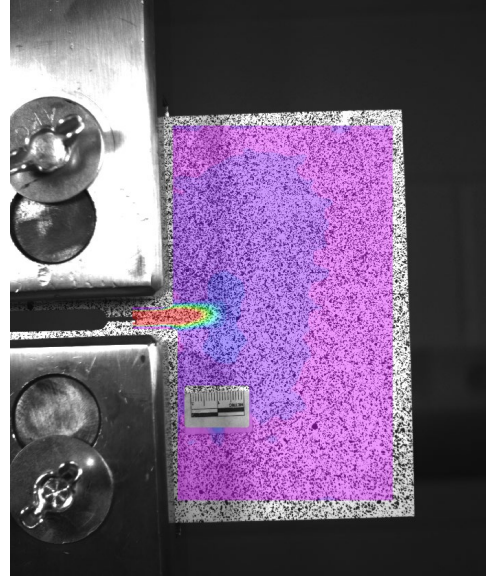


<center>(b)</center>

Figure 3.6 DIC results for a 25.4 mm (1.0 in.) crack with 432 mm (17.0 in.) camera distance under LC5 and Condition 1 in terms of (a) displacement and (b) strain
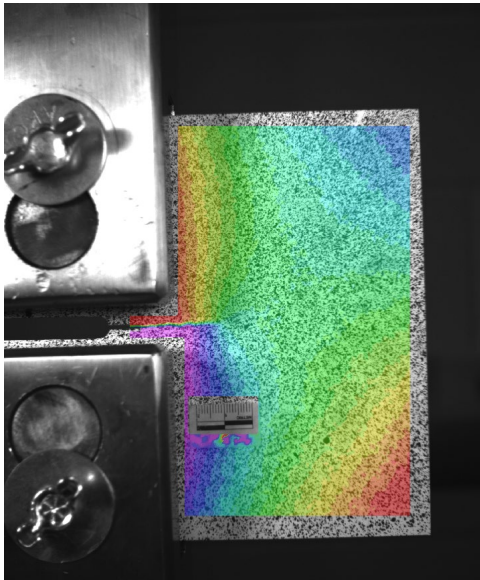


<center>(a)</center>
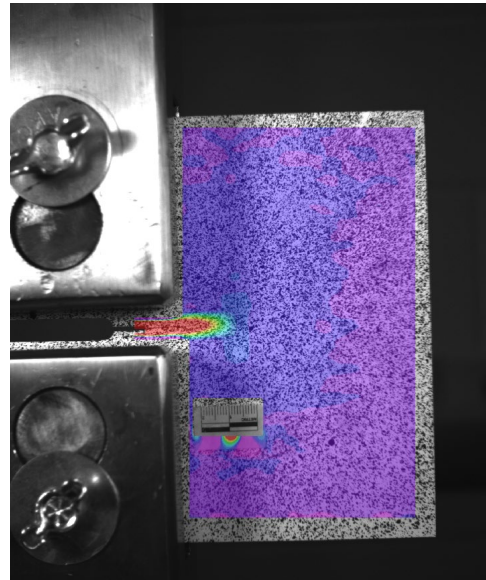


<center>(b)</center>

Figure 3.7 DIC results for a 25.4 mm (1.0 in.) crack with 432 mm (17.0 in.) camera distance under LC5 and Condition 5 in terms of (a) displacement and (b) strain

Compared to the 648 mm (25.5 in.) camera spacing, the crack is more clearly visible in the DIC displacement and strain fields. Figure 3.8 shows representative convergence values for LC5, with the vertical dotted line representing the actual crack length. Convergence plots for LC1 through LC4 are shown in Appendix A. Convergence was calculated using in-plane displacement values and the developed crack characterization methodology.
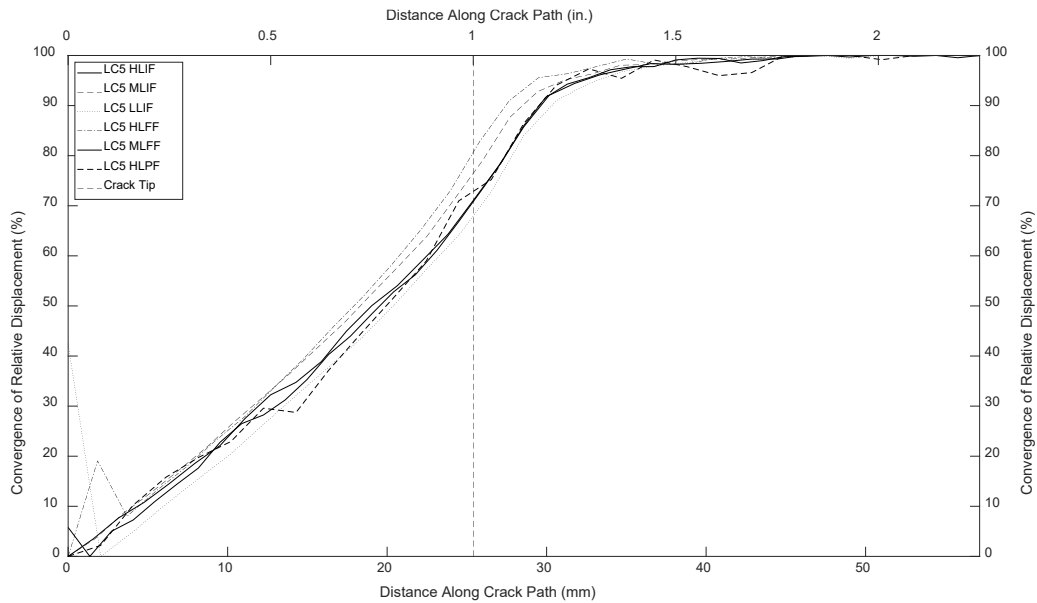


Figure 3.8 Convergence of relative displacement of a 25.4 mm (1.0 in.) crack under LC5

The distribution of convergence values for the 432 mm (17.0 in.) camera spacing shows a significant decrease in scatter compared to the furthest camera distance shown in Figure 3.4. Convergence values for the different lighting and focus condition combinations are shown in Table 3.6, averaged across all five load cases for a crack length of 25.4 mm (1.0 in.). Convergence for each condition and load case is represented visually in Figure 3.9. The ideal results for load cases 1, 3, and 5 are shown for comparison and lines are shown for clarity.

Table 3.6 Average convergence at 25.4 mm (1.0 in.) crack
tip for 432 mm (17.0 in.) camera distance

| Light and Focus Condition | Average Convergence | Difference |
|---|---|---|
| Ideal | 92.6% | N/A |
| 1 | 70.7% | 21.9% |
| 2 | 76.6% | 16.0% |
| 3 | 69.9% | 22.7% |
| 4 | 80.5% | 12.1% |
| 5 | 72.0% | 20.6% |
| 6 | 72.9% | 19.7% |
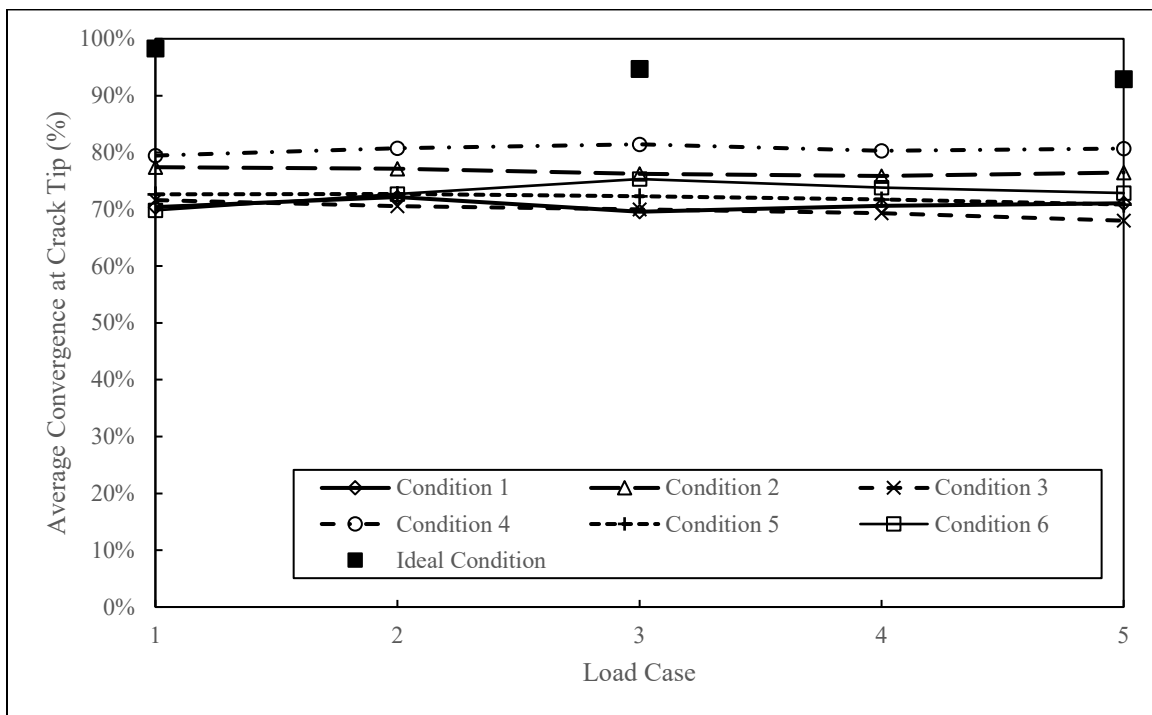


Figure 3.9 Average convergence at crack tip for each load case and condition for a 25.4 mm (1.0 in.) crack with a camera distance of 432 mm (17.0 in.)

Decreasing the distance between the camera decreases the variability of the convergence at the crack tip, as seen in Figure 3.9. As with the 642 mm (25.5 in.) camera spacing, there is a noticeable decrease in the convergence for non-ideal testing conditions. On average, there is a

decrease of calculated convergence at the crack tip of 18.8% for the 25.4 mm (1.0 in.) crack,

slightly improved from the average of 21.6% from the furthest camera spacing. Table 3.7 shows

the decrease in convergence for a crack length of 12.7 mm (0.5 in.).

Table 3.7 Average convergence at 12.7 mm (0.5 in.) crack
tip for 432 mm (17.0 in.) camera distance

| Light and Focus Condition | Average Convergence | Difference |
|---|---|---|
| Ideal | 75.0% | N/A |
| 1 | 58.0% | 17.0% |
| 2 | 54.6% | 20.4% |
| 3 | 56.4% | 18.6% |
| 4 | 54.0% | 21.0% |
| 5 | 59.2% | 15.8% |
| 6 | 57.0% | 18.0% |

*3.2.3 Camera to Specimen Distance of 216 mm (8.5 in.)*

DIC data for the primary camera distance of 216 mm (8.5 in.), emulating the spacing used in the development of the crack characterization methodology, was collected for crack lengths of 12.7 and 25.4 mm (0.5 and 1.0 in.) under the five specified load cases and the six lighting and focus conditions. Typical outputs from the DIC software for LC5 with a crack length of 25.4 mm (1.0 in.) are shown in Figures 3.10 and 3.11, showing conditions 1 and 5, respectively.
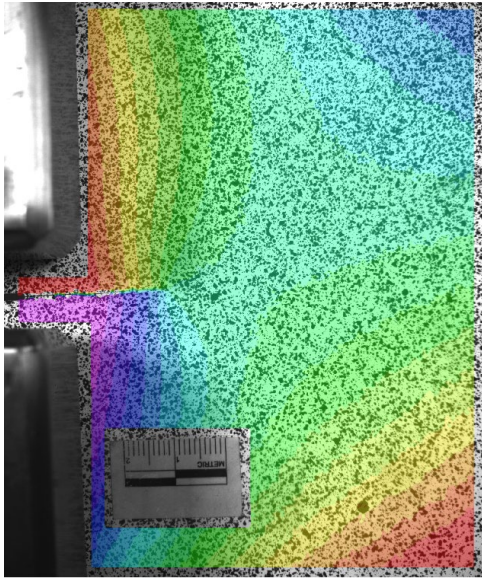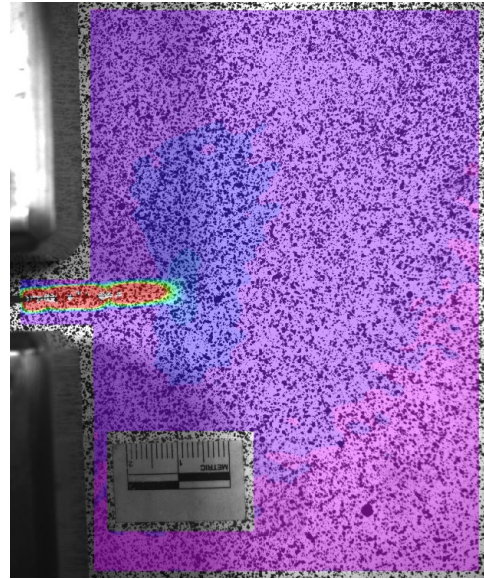
(a)                                                              (b)

Figure 3.10 DIC results for a 25.4 mm (1.0 in.) crack with 216 mm (8.5 in.) camera distance under LC5 and Condition 1 in terms of (a) displacement and (b) strain
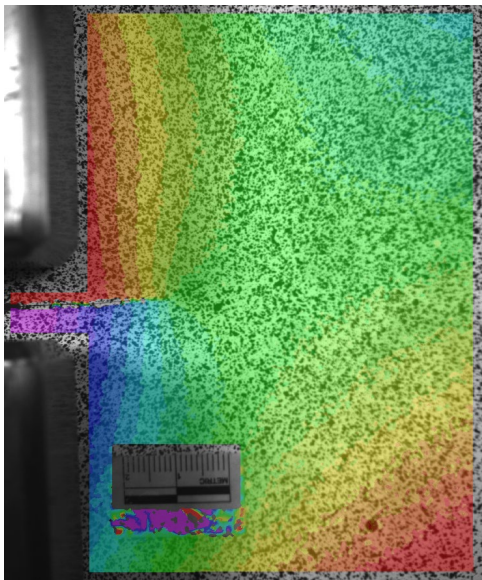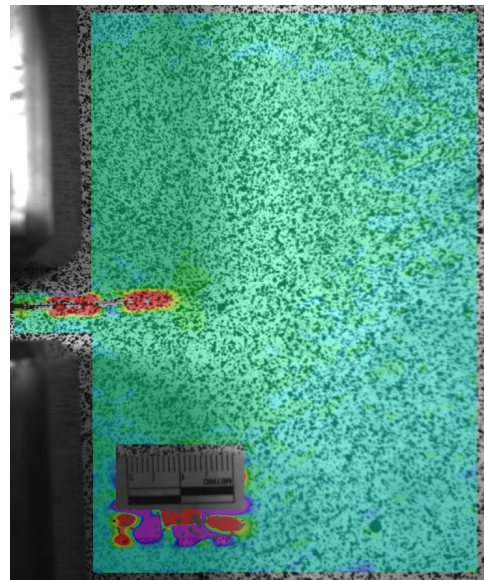


(a)                                                              (b)

Figure 3.11 DIC results for a 25.4 mm (1.0 in.) crack with 216 mm (8.5 in.) camera distance under LC5 and Condition 5 in terms of a) displacement and b) strain

Once again, the reduced camera distance results in a clearer indication of cracking in the DIC output. Figure 3.12 shows representative convergence values for LC5, with the vertical dotted line representing the actual crack length. Convergence plots for LC1 through LC4 are shown in Appendix A. Convergence was calculated using in-plane displacement values and the developed crack characterization methodology.
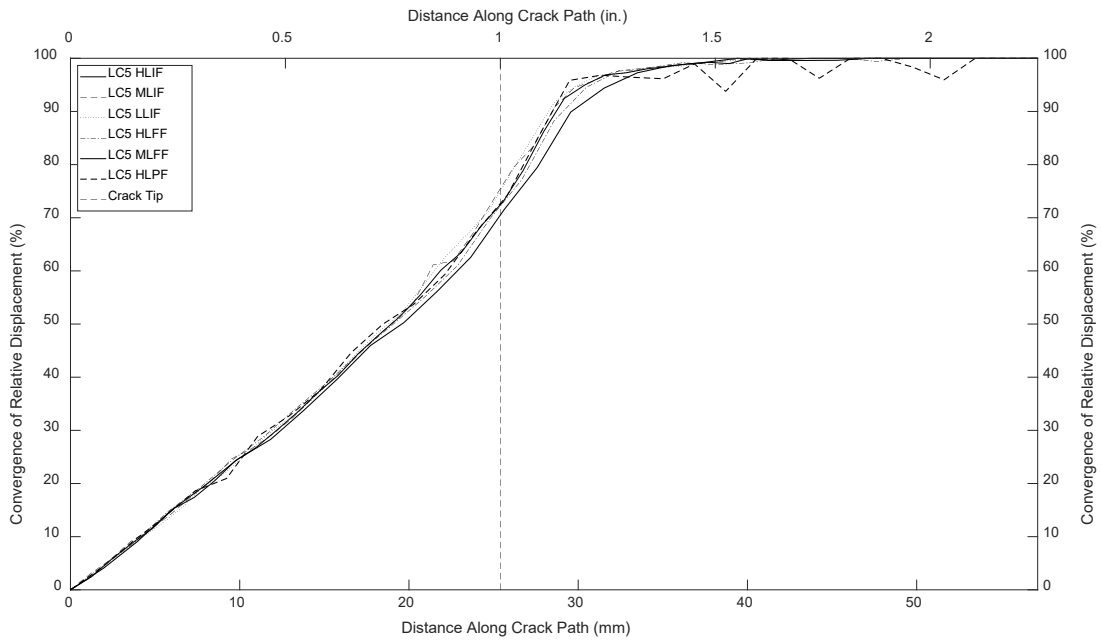


Figure 3.12 Convergence of relative displacement of a 25.4 mm (1.0 in.) crack under LC5

As with the 432 mm (17.0 in.) camera spacing, the distribution of convergence values is further reduced for the closest camera spacing. Convergence values for the different lighting and focus condition combinations are shown in Table 3.8, with values averaged across all five load cases for a crack length of 25.4 mm (1.0 in.). Convergence for each condition and load case is represented visually in Figure 3.13. The ideal results for load cases 1, 3, and 5 are shown for comparison and lines are shown for clarity.

Table 3.8 Average convergence at 25.4 mm (1.0 in.) crack
tip for 216 mm (8.5 in.) camera distance

| Light and Focus Condition | Average Convergence | Difference |
|---|---|---|
| Ideal | 92.6% | N/A |
| 1 | 73.0% | 19.6% |
| 2 | 75.7% | 16.9% |
| 3 | 75.6% | 17.0% |
| 4 | 72.6% | 20.0% |
| 5 | 70.1% | 22.5% |
| 6 | 72.8% | 19.8% |



Figure 3.13 Average convergence at crack tip for each load case and condition for a 25.4 mm
(1.0 in.) crack with a camera distance of 216 mm (8.5 in.)

Similar to the two further camera spacings, Figure 3.13 shows how the non-ideal

conditions decreases the convergence at the crack tip compared to the ideal conditions. Using a

smaller distance between the camera and the specimen greatly reduces the variability of the

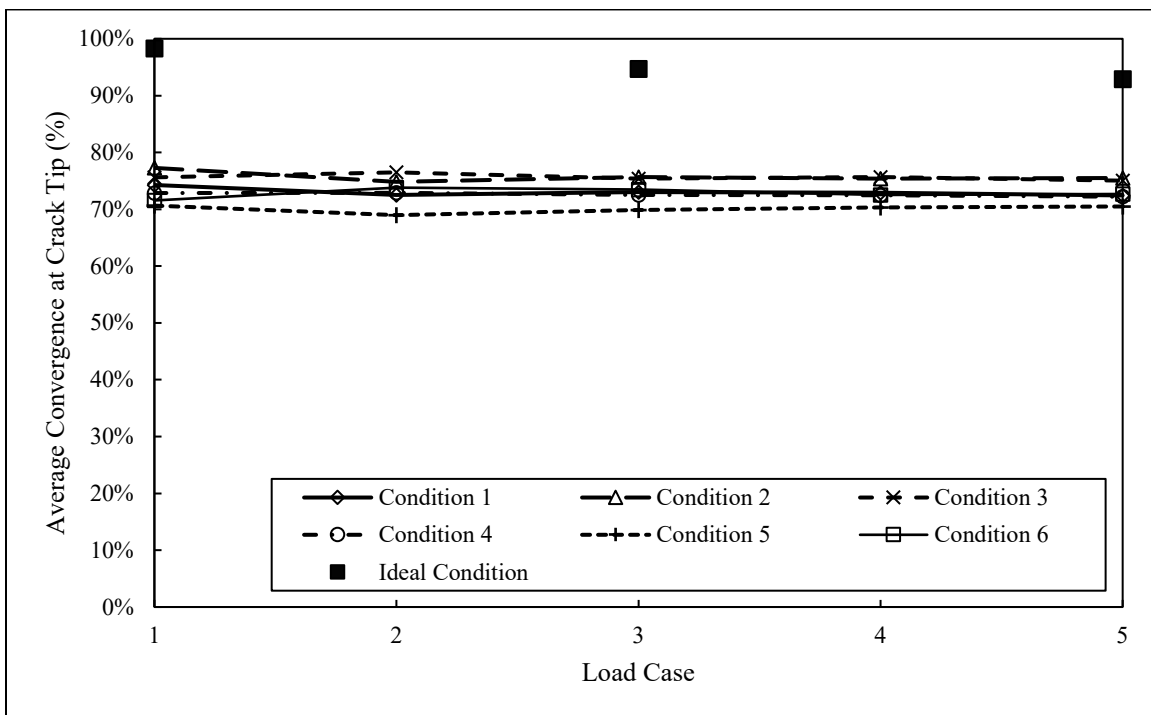convergence from sub-optimal conditions, but still results in an average decrease in calculated

convergence at the crack tip from ideal conditions of 19.3% for the 25.4 mm (1.0 in.) crack.

Across all lighting and focus condition tests, the only clear trend that emerged was that

reduced camera distance improved the accuracy and precision of convergence calculations. The

smallest camera to specimen distance in particular had a noticeable impact on the results for the

12.7 mm (0.5 in.) crack. For a camera to specimen spacing of 648 mm (25.5 in.), the average

decrease in convergence at the crack tip was 22.9% for a 12.7 mm (0.5 in.) crack, while the

average decrease was 16.5% for a spacing of 216 mm (8.5 in.), shown in Table 3.9. This

indicates that for shorter crack lengths, the most important condition is the camera to specimen

distance, rather than lighting or focus. Once again, while the convergence values are significantly

lower under sub-optimal conditions, the crack is still being detected.

Table 3.9 Average convergence at 12.7 mm (0.5 in.) crack
tip for 216 mm (8.5 in.) camera distance

| Light and Focus Condition | Average Convergence | Difference |
|---|---|---|
| Ideal | 75.0% | N/A |
| 1 | 58.6% | 16.4% |
| 2 | 56.7% | 18.3% |
| 3 | 56.1% | 18.9% |
| 4 | 57.7% | 17.3% |
| 5 | 63.1% | 11.9% |
| 6 | 59.1% | 15.9% |

3.3 Study on the Impact of Aperture

*3.3.1 Aperture Background*

      Aperture is a measure of how open the lens of a camera is. This is the component that controls the physical amount of light allowed into the camera. Aperture is defined based on the "f-stop" number, where f/1.4 allows a large amount of light into the camera and f/11 or higher lets a very small amount of light in. Figure 3.14 shows a comparison between different aperture values on a C(T) specimen with a camera to specimen distance of 305 mm (12.0 in.). All photographs were taken with the same external lighting conditions, from the same location, and have no post-processing or editing.



      (a)                       (b)                     (c)
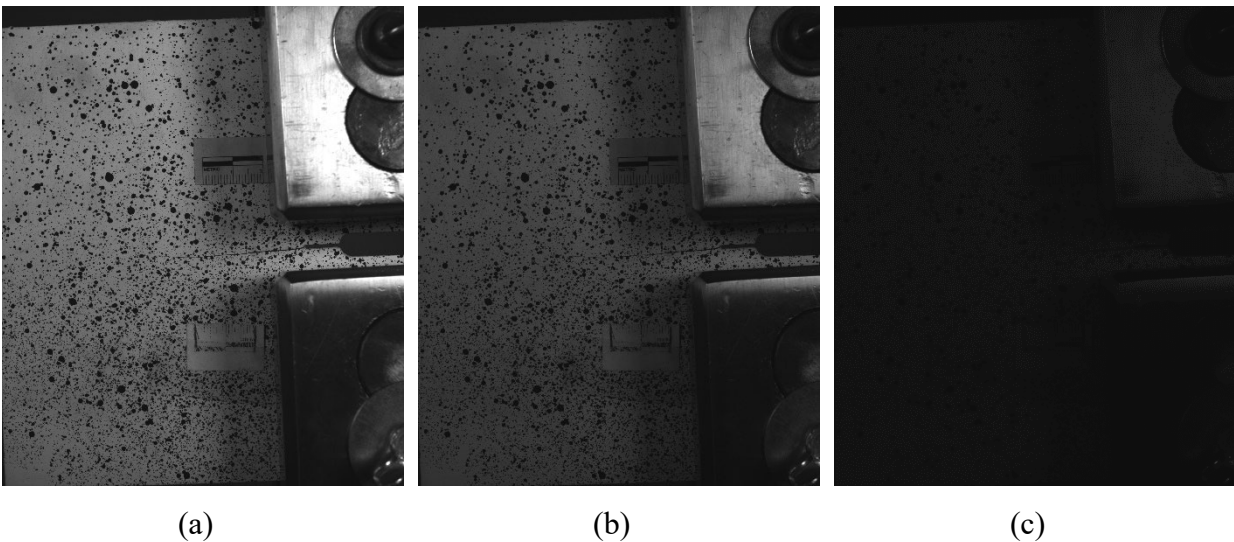
Figure 3.14 C(T) specimen photographed with apertures of (a) f/2.8; (b) f/4; and (c) f/11

      Aperture also has some impact on the camera field depth. The larger the camera opening is, the smaller the field depth , and the closer the camera would need to be to the specimen. Some cameras have lenses that can automatically adjust aperture, but the cameras utilized in this study

must be changed manually, making understanding the impact of the aperture on DIC results important.

### 3.3.2 Aperture Testing Setup and Loading

Testing for the impact of aperture was performed on the same C(T) specimen after the conclusion of the lighting and focus study, so it was performed on a single crack length of 50.8 mm (2.0 in.) under LC5. Images were collected for four different camera-to-specimen distances and for four different aperture values with idealized light and focus conditions. The four camera-to-specimen distances were 203, 305, 457, and 610 mm (8.0, 12.0, 18.0, and 24.0 in.). Data was collected for apertures of f/1.4, f/2.8, f/4, and f/11, but due to low light and poor quality of the f/4 and f/11 images, only images taken with apertures of f/1.4 and f/2.8 were analyzed using DIC.

### 3.3.3 Aperture Study Results

A convergence plot for the 50.8 mm (2.0 in.) crack with a camera distance of 203 mm (8.0 in.) and an aperture of f/1.4 is shown in Figure 3.15. The camera distance and aperture setting almost exactly match the initial testing performed on the C(T) specimen, and results in a similar convergence seen in previous testing. This convergence plot is representative of the remaining seven combinations of camera distance and aperture, which are presented in Appendix A. Convergence plots for the other conditions displayed more noise near the middle of the crack, but the amount of noise did not seem to vary with aperture setting or camera distance. The aperture of f/2.8 resulted in higher convergence values for all camera distances except for 305 mm (12.0 in.) as shown in Table 3.10.
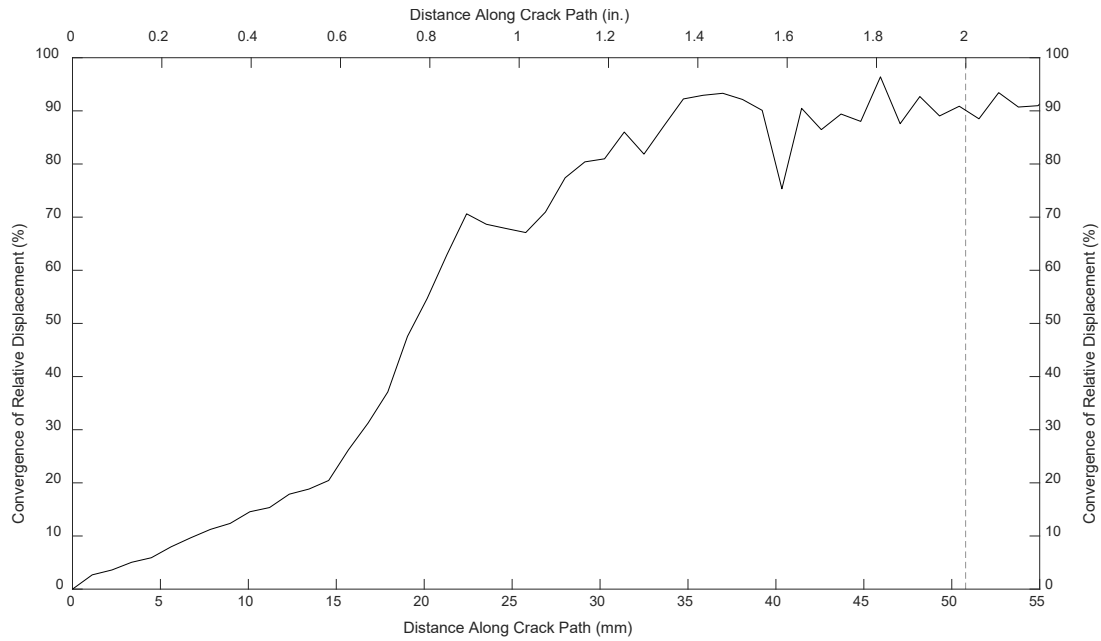
Figure 3.15 Convergence of relative displacement of a 50.8 mm (2.0 in.) crack with a camera distance of 203 mm (8.0 in.) and an aperture of f/1.4 under LC5

Table 3.10 Convergence of 50.8 mm (2.0 in.) crack under varying camera distances and aperture conditions

| Camera to Specimen Distance, mm (in.) | Aperture Setting | |
|---|---|---|
| | f/1.4 | f/2.8 |
| 203 (8.0) | 90.1% | 95.0% |
| 305 (12.0) | 84.9% | 78.1% |
| 457 (18.0) | 74.7% | 87.4% |
| 610 (24.0) | 79.3% | 82.9% |
| Avg. | 82.3% | 85.9% |

Aperture could potentially serve to correct for non-ideal lighting and focus conditions. Additional research will need to be performed to evaluate exactly how much aperture impacts the quality of image focus. Other than this brief investigation, all testing has been performed with an aperture of f/1.4, which is the largest aperture possible on the cameras used for testing. Using a

camera with an automatic focusing lens and an adjustable aperture could help to simplify the test

setup required on a UAV and result in higher quality images.

Chapter 4 Investigation into Open-Source DIC Alternatives

4.1 Open-Source Software Overview

Some of the work towards automating a DIC bridge inspection methodology included

evaluation of available open-source DIC software. Commercially-available DIC software can be

expensive and is not easily adapted to some purposes (Harilal and Ramji 2014). Open-source

software has the potential to allow for more flexible analysis of DIC data. Additionally, open-

source software could allow for different data collection methods, without the need for

specialized or idealized test setups. This is important for the development of an accessible

inspection system. While much of the investigation into open-source software involved reading

literature about the different alternatives, some viable open-source alternatives were identified

and assessed using the existing data sets.

Open-source DIC alternatives can be used for 2D or 3D analysis. DIC post-processing

can use a subset-based (local) approach or a finite element-based (global) approach (Wang and

Pan 2016). Local DIC breaks the area of interest into independent reference subsets and

determines the change between the original and deformed image using a local shape function.

Global DIC divides the area of interest into a series of nodes solved simultaneously to ensure

displacement continuity. The Correlated Solutions VIC software utilizes a local DIC algorithm

for determining displacements. Local DIC is used in most commercial software due to the high

accuracy, high efficiency, and easy implementation of subset-based algorithms. Global DIC is

beneficial because it maintains continuity in the data and results in more accurate displacement

results with less gaps in the data.

<u>4.2 Open-Source Software Alternatives</u>

      The International DIC Society (2018) has identified several open-source programs that have been developed by the research community and made available to fellow researchers. Of the options presented, seven emerged as potentially viable alternatives for use in automated bridge inspections: *Ncorr*, Augmented Lagrangian DIC (*ALDIC*), DICengine (*DICe*), *pyDIC*, *py2DIC*, *pyxel*, and *YaDICs*. While each were feasible for analyzing fatigue cracks on steel bridge members, only three alternatives were investigated deeper due to incompatible operating systems, lack of knowledge of the software language, or lack of software documentation to assist with use. A summary of the analysis and approach methods as well as the programming languages used by the different DIC alternatives is presented in Table 4.1.

Table 4.1 Comparison of open-source DIC software

| Software | Analysis | Approach | Language |
|----------|----------|----------|----------|
| Ncorr | 2D | Local | MATLAB |
| ALDIC | 2D | Local and Global | MATLAB |
| DICe | 2D and 3D | Local or Global | C++ |
| pyDIC | 2D | Local | Python |
| py2DIC | 2D | Local | Python |
| pyxel | 2D | Global | Python |
| YaDICs | 2D and 3D | Local and Global | C++ |

*4.2.1 Ncorr*

      *Ncorr* is a 2D DIC program developed by the Georgia Institute of Technology in Georgia, United States (Blaber et al. 2015). Designed to address a lack of user-friendly alternatives, *Ncorr* is written entirely in MATLAB and features a high-quality graphical user interface (GUI). It introduces a Eulerian to Lagrangian conversion to analyze areas of

discontinuities in displacement fields. When discontinuities are detected, the software creates a region of interest and performs DIC on that area. Interpolation and a nonlinear optimization algorithm then determine the best fit for the areas with missing data. This has the potential to prove useful in images with poor focus or lighting conditions or with gaps in data due to non-ideal speckle pattern application. The built in user interface also includes contour plotting tools for visualizing the data quickly. This software was successfully used to analyze in-plane and out-of-plane cracks.

*4.2.2 ALDIC*

Developed by the California Institute of Technology in California, United States, *ALDIC* is a 2D DIC code also written in MATLAB (Yang and Bhattacharya 2020). It combines the speed and non-iterative analysis of local DIC and the displacement compatibility and smoothness of global DIC approaches. *ALDIC* utilizes subsets locally to determine multiple smaller displacement fields and then applies a compatibility requirement for global analysis to ensure there are no gaps or discontinuities in the displacement field without drastically increasing computation time. Both in-plane and out-of-plane cracks were successfully analyzed using *ALDIC*.

*4.2.3 DICe*

*DICe* is a 2D and 3D DIC alternative written in C++ developed by the Sandia National Laboratories in New Mexico, United States (Turner 2015). It allows the user to choose between local and global DIC analysis methods and can also be applied in the tracking of rigid body motion. Like *Ncorr*, it is presented with an intuitive GUI, but does not feature the easy to use contour plotting options. Instead, output strain and displacement fields must be visualized using

separate software or a free open-source data visualization application such as ParaView. *DICe* was used in the analysis of both in-plane and out-of-plane cracks.

*4.2.4 pyDIC*

   *pyDIC* is a 2D DIC alternative written in Python developed at the Ensil-Ensci Engineering School in Limoges, France. It uses a local analysis with a built-in noise reduction function to produce smoother strain fields. *pyDIC* leverages a number of Python libraries such as *OpenCV* that must be installed in order for the software to work. This software was used to analyze in-plane cracks, but the displacement field output data was found to not be suitable for fatigue crack detection. Furthermore, *pyDIC* has limited instruction documentation, so this issue was unable to be resolved.

*4.2.5 py2DIC*

   *py2DIC* was developed by the Geodesy and Geomatics Division of Sapienza University of Rome, in Rome, Italy (Belloni et al. 2019). As with *pyDIC*, it performs local, 2D DIC analysis and leverages other Python libraries, including *OpenCV*, while also including a GUI that allows the user to change a number of options. The analysis of the in-plane crack was not successful due to the presence of bugs in the code and the incompatibility with newer versions of *OpenCV*. Similar to *pyDIC*, the instruction manual has limited information and was not able to assist in solving this issue.

*4.2.6 pyxel*

   *pyxel* is a global, 2D DIC software developed for Python by the Institut National des Sciences Appliquées de Toulouse in Toulouse, France (Passieux and Bouclier 2019). It relies on the calibration of camera models and external object meshing libraries such as *Gmsh*. Plotting capabilities are not built-in to *pyxel*, but the output is available in forms that are compatible with

other Python libraries such as *Matplotlib* or free software such as *ParaView*. Inexperience with Python and a lack of robust documentation resulted in unsuccessful analysis of the in-plane crack.

### 4.2.7 YaDICs

*YaDICs* is a 2D and 3D DIC alternative that was developed at the Laboratoire de Mécanique de Lille in Lille, France. It was developed for C++ running on a Linux operating system. This alternative combines local and global DIC at different scales in the images similar to *ALDIC*. However, a Linux operating system was not readily available, so no further evaluation was possible.

### 4.3 Open-Source Software Results

To evaluate the open-source DIC alternatives, existing images captured from the in-plane C(T) crack tests and the out-of-plane distortion-induced fatigue girder sub-assembly were used. Three open-source DIC alternatives successfully provided displacement gradients for both scenarios: *Ncorr*, *ALDIC*, and *DICe*. This section describes the procedure for using each of the three alternatives as well as the results obtained from the analysis. For comparison purposes, the output of all three alternatives was exported to MATLAB and plotted as contours.

### 4.3.1 Ncorr Results

Installation instructions for *Ncorr* are provided by the developers. The GUI, shown in Figure 4.1, prompts the user for the reference image and the deformed image(s) to be analyzed. The region of interest and relevant DIC parameters such as subset size and spacing are then defined. For this analysis, a subset size of 20 pixels and a subset spacing of 1 pixel was used. These values were shown to reduce the amount of noise in the displacement data at the cost of

computation time. The contour plots for the full-field *v* displacement of the in-plane crack and

the *u* and *v* displacements of the out-of-plane crack are shown in Figures 4.2 and 4.3.
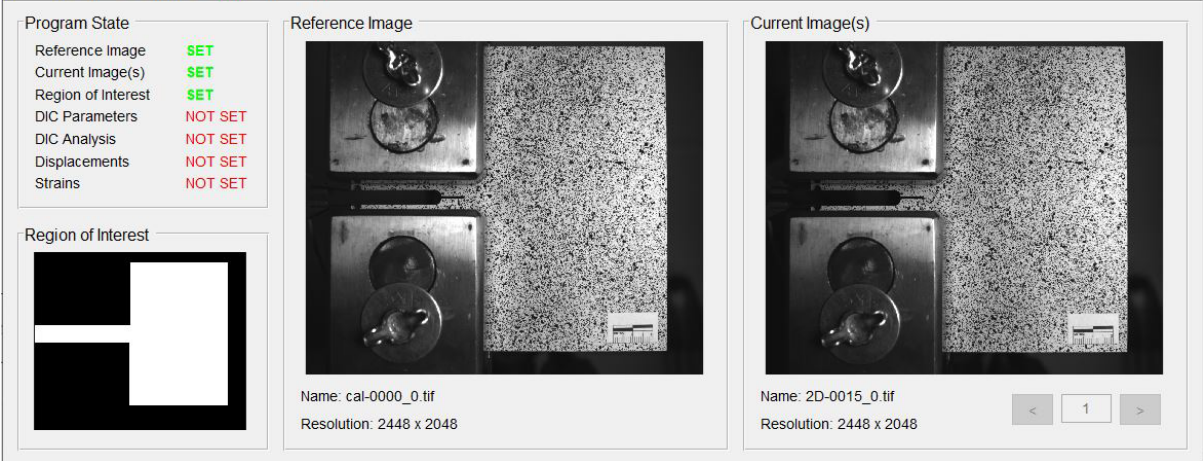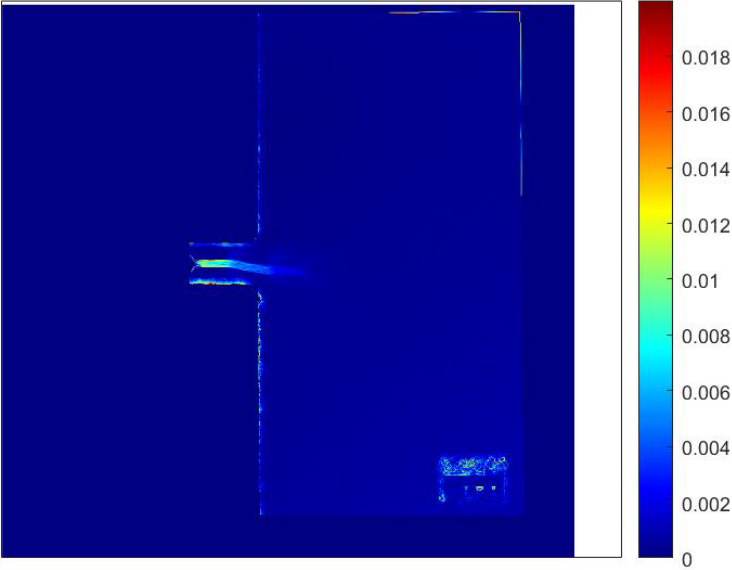


Figure 4.1 Ncorr GUI



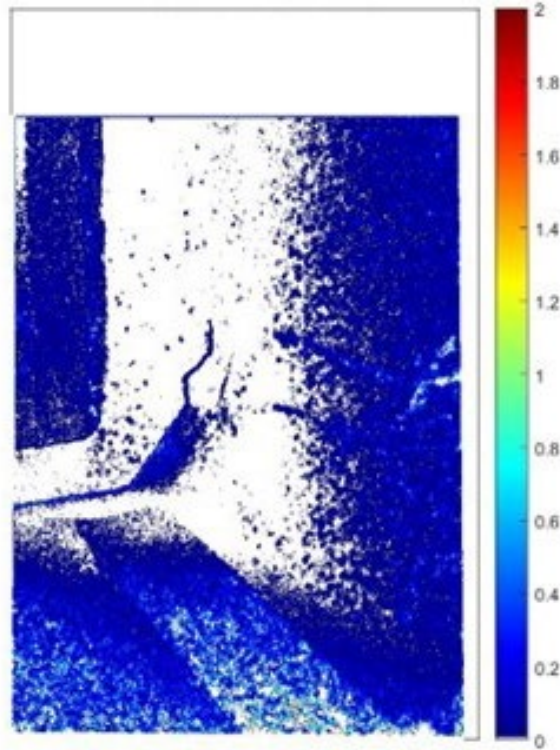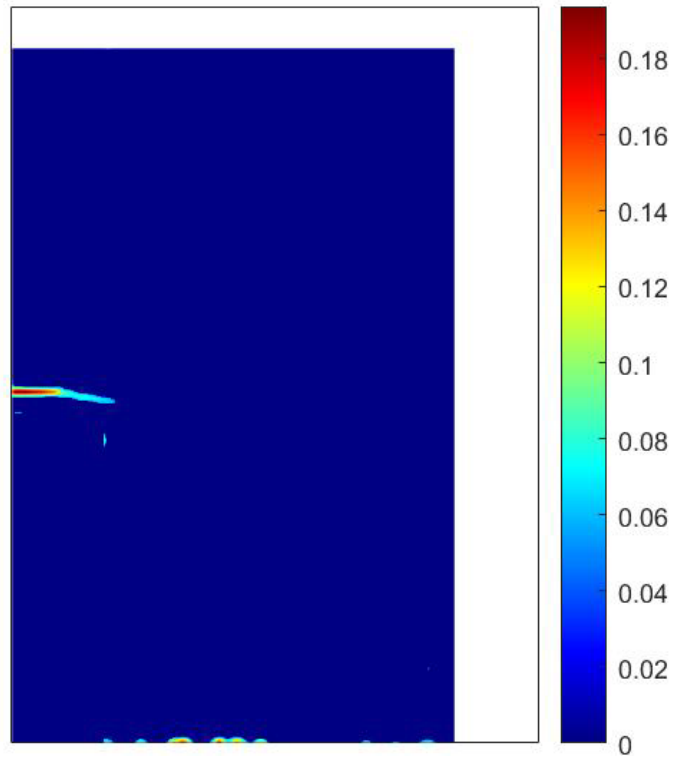Figure 4.2 *Ncorr* in-plane crack displacement gradient

Figure 4.3 *Ncorr* out-of-plane crack displacement gradient

*Ncorr* clearly detects the fatigue cracks for both test set-ups. The C(T) crack tip is slightly ambiguous, but the minimal noise from the surroundings allows for an accurate depiction of the crack. The out-of-plane crack is particularly clear, and the wide region of interest shows the clipped stiffener in the web-gap region, providing context for the output results.

*4.3.2 ALDIC Results*

The MATLAB code for *ALDIC* is separated into nine sections with commentary in the instruction manual providing explanation of each section's function and use. The region of interest and DIC parameters are defined programmatically. In this analysis, a subset size of 20 pixels and a subset spacing of 10 pixels was found to produce minimal noise and an acceptable computation time. Once the code is run successfully, the ResultStrain workspace variable contains full-field displacement data. The contour plots for the full-field *v* displacement of the in-

plane crack and the *u* and *v* displacements of the out-of-plane crack are shown in Figures 4.4 and
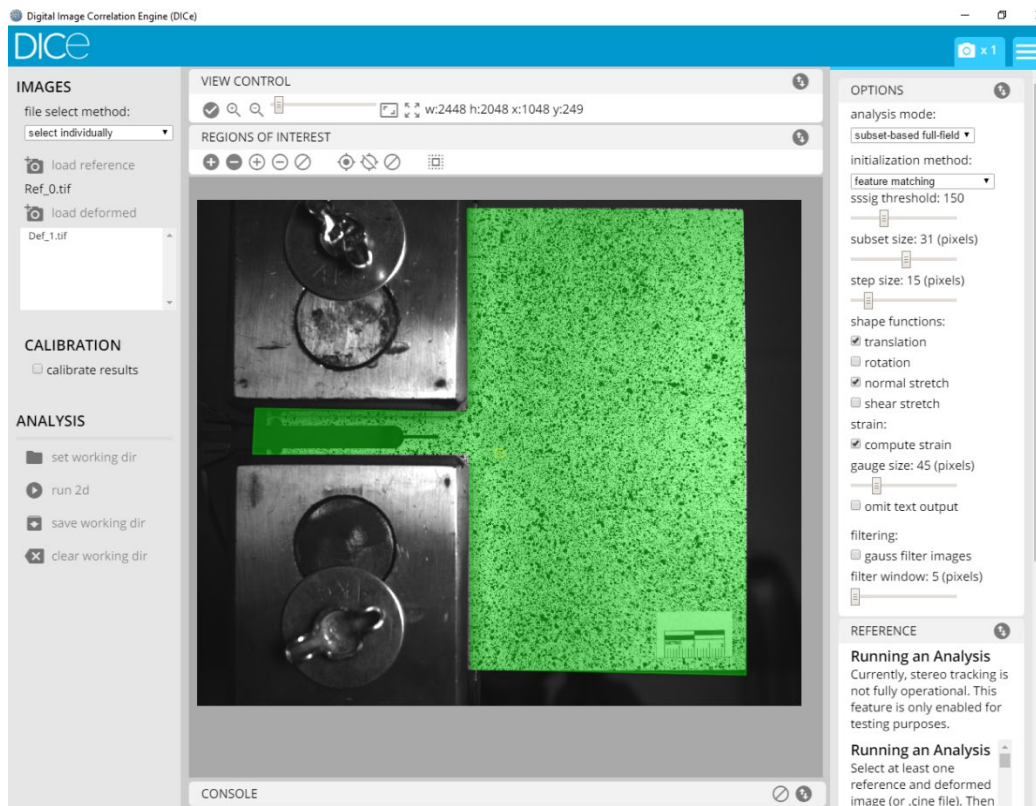
4.5.



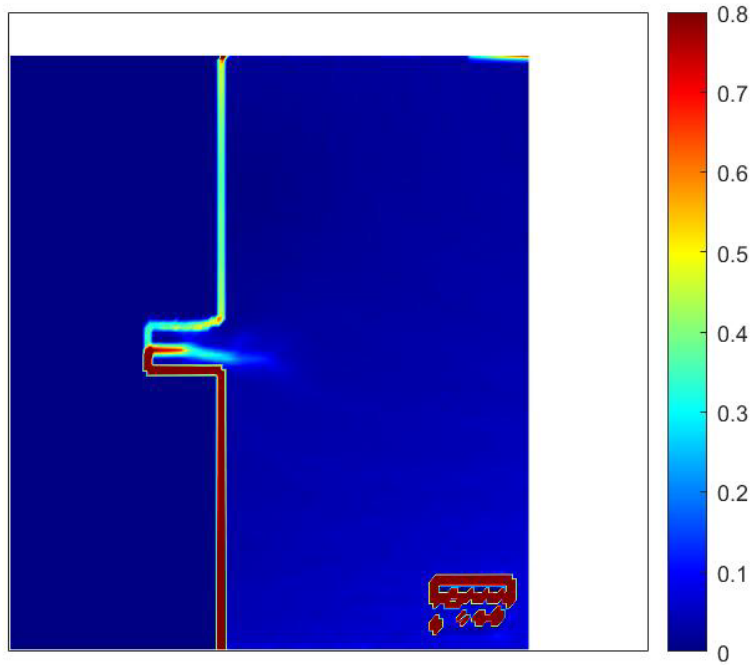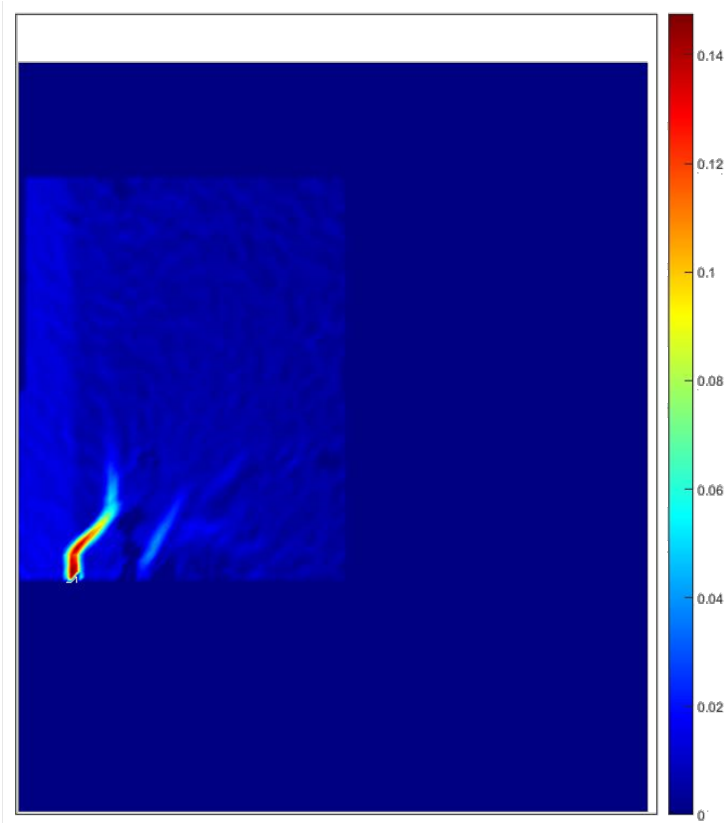Figure 4.4 *ALDIC* in-plane crack displacement gradient
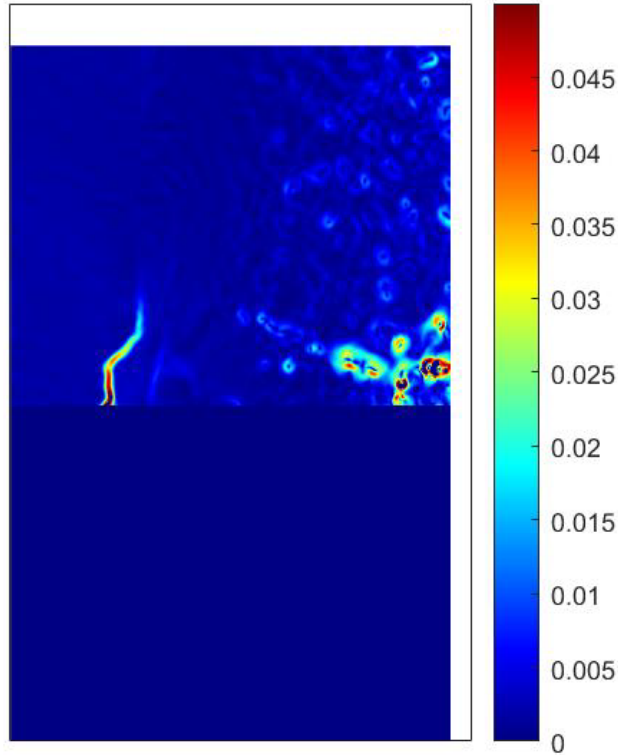
Figure 4.5 *ALDIC* out-of-plane crack displacement gradient

*ALDIC* is able to detect the fatigue crack for both test set-ups. The region of interest is only able to be defined as a rectangular area, causing context around the cracks to be lost. Both crack lengths are also slightly underestimated, with the secondary horizontal crack in the C(T) specimen missing and the secondary vertical crack in the girder sub-assembly having an ambiguous crack tip.

*4.3.3 DICe Results*

After installation, the basic functions of the GUI (see fig. 4.6) are described in the documentation page by the developers. Reference image and deformed image(s) are loaded in and the region of interest is defined using drawing tools. The analysis options, including 2D or 3D and local or global DIC, are clearly visible on the right side of the GUI. For local analysis, the subset size and spacing are easily edited. In this analysis, the default values of 31 pixels and

15 pixels were used for the size and spacing, respectively. These values provided fast

computation and precise displacement fields. The displacement field data is output as a text file,

which was then imported into MATLAB for plotting. The contour plots for the full-field $v$

displacement of the in-plane crack and the $u$ and $v$ displacements of the out-of-plane crack are

shown in Figures 4.7 and 4.8.



Figure 4.6 *DICe* GUI

Figure 4.7 *DICe* in-plane crack displacement gradient



Figure 4.8 *DICe* out-of-plane crack displacement gradient

*DICe* is able to detect both in- and out-of-plane fatigue cracks, but seems to struggle with accurate estimation of crack length. The region of interest for the C(T) specimen is bounded by sharp edges despite not including the clevises which skews the displacement scale greatly. As a result, the crack tip is ambiguous and crack length is difficult to determine. To avoid this issue with the girder sub-assembly, the region of interest must be very narrow, which removes the context of the image. The secondary vertical section of the crack is visible but also ambiguous, once again underestimating crack length.

# Chapter 5 Chapter 5 Conclusions and Future Work

## 5.1 Conclusions

This report summarized the impacts of lighting, focus, camera distance, and aperture setting on a developed digital image correlation methodology for detecting cracks. The crack detection method was developed using in-plane loading data from a C(T) specimen and was verified on a distortion-induced fatigue test specimen. Since the ideal testing conditions the methodology was developed under are not realistic to in-service highway infrastructure, the impact of non-idealized conditions need to be evaluated. Research showed that while lighting and focus conditions have a significant impact on the convergence calculated, the crack is still detectable under tension even in non-ideal conditions.

With ideal focus, light levels less than half of the ideal condition result in images of sufficient quality for DIC analysis. However, even a 5% decrease in focus requires nearly ideal lighting in order to obtain images able to be processed. The lighting and focus testing also indicated that the distance from the camera to the region of interest is the most impactful variable in reducing the variability of convergence. A brief study of aperture settings revealed that an aperture that allows less light, such as f/4 or f/11, is not feasible for DIC applications. Of the two apertures tested, the f/2.8 resulted in increased convergence at the crack tip compared to the f/1.4.

Open-source DIC alternatives were also evaluated to detect fatigue cracks. Of the seven options investigated, three were able to successfully detect both in- and out-of-plane cracks. These three—*Ncorr*, *ALDIC*, and *DICe*—will be further evaluated for potential to be adapted to automated DIC analysis.

The developed crack detection methodology has been validated for both in- and out-of-plane fatigue cracks. An important constraint for applying DIC to crack detection is the complexity of the crack geometry. For DIC to be implemented in the field, the developed methodology must be adequate for the detection of any distortion-induced fatigue crack found on in-service structures. Commonly, distortion-induced fatigue cracks display complex patterns with multiple branches. Further testing using the girder sub-assembly will evaluate the ability of DIC to quantify a complex, branching distortion-induced fatigue crack.

One of the main concerns regarding the developed crack detection methodology is the necessity of the inspector to manually draw orthogonal inspection lines. Future work will expand upon the use of open-source DIC software. Open-source software has the potential to allow for more flexible analysis of DIC data. Additionally, open-source software could allow for different data collection methods, without the need for specialized, ideal test setups. This is important for the development of an accessible inspection system. In addition to the expanded evaluation of open-source DIC software, other vision-based methodologies and machine learning algorithms will be evaluated for potential capability for use in fatigue crack inspection.

Future work will also examine existing deployment mechanisms capable of delivering a vision-based inspection hardware to the area of interest on highway infrastructure. Commercial and research-focused tools will be identified, and strengths and weaknesses of each system will be evaluated for use in highway bridge inspections. Both unmanned aerial vehicles (UAVs) and robotic crawlers will be examined, as well as any other delivery mechanism identified that has potential for bridge inspections. Determining a deployment mechanism is required for the goal of implementing an automated computer vision-based inspection system.

References

Abdel-Qader, I., Abudayyeh, O., & Kelly, M. E. (2003). Analysis of edge-detection techniques for crack identification in bridges. *J. Comp. Civil Eng.*, 17(4), 255-263.

Alipour, M., Washlesky, S. J., & Harris, D. K. (2019). Field Deployment and Laboratory Evaluation of 2D Digital Image Correlation for Deflection Sensing in Complex Environments. *J. Bridge Eng.*, 24(4), 04019010. doi: 10.1061/(ASCE)BE.1943-5592.0001363.

American Society of Civil Engineers (ASCE). (2017). 2017 Infrastructure Report Card – Bridges, https://www.infrastructurereportcard.org/wp-content/uploads/2017/01/Bridges-Final.pdf.

Blaber, J., Adair, B., and Antoniou, A. (2015). Ncorr: Open-Source 2D Digital Image Correlation Matlab Software. *Exp. Mech.*, 55, 1105-1122. doi: 10.1007/s11340-015-0009-1.

Belloni, V., Ravanelli, R., Nascetti, A., Di Rita, M., Mattei, D., & Crespi, M. (2019). py2DIC: A New Free and Open Source Software for Displacement and Strain Measurements in the Field of Experimental Mechanics. *Sensors*, 19(18), 3832. doi: 10.3390/s19183832.

Campbell, L. E., Connor, R. J., Whitehead, J. M., & Washer, G. A. (2020). Benchmark for Evaluating Performance in Visual Inspection of Fatigue Cracking in Steel Bridges. *J. Bridge Eng.*, 25(1). doi: 10.1061/(ASCE)BE.1943-5592.0001507.

Cha, Y. J., Choi, W., & Büyüköztürk, O. (2017). Deep Learning-Based Crack Damage Detection Using Convolutional Neural Networks. *Comp.-Aided Civil Infrastruct. Eng.*, 32(5), 361-378.

Chen, F., Chen, X., Xie, X., Feng, X., & Yang, L. (2013). Full-field 3D measurement using multi-camera digital image correlation system. *Opt. Lasers Eng.*, 51(9), 1044-1052. doi: 10.1016/j.optlaseng.2013.03.001.

Cigada, A., Mazzoleni, P., & Zappa, E. (2014). Vibration monitoring of multiple bridge points by means of a unique vision-based measuring system. *Exp. Mech.*, 54(2), 255-271.

Connor, R. J., & Fisher, J. W. (2006). Identifying effective and ineffective retrofits for distortion fatigue cracking in steel bridges using field instrumentation. *J. Bridge Eng.*, 11(6), 745-752.

Dellenbaugh, L., Kong, X., Al-Salih, H., Collins, W., Bennett, C., Li, J., & Sutley, E. (2020). "Development of Distortion-Induced Fatigue Crack Characterization Methodology using Digital Image Correlation." *J. Bridge Eng.*, 25(9). doi: 10.1061/(ASCE)BE.1943-5592.0001598.

Dhanasekar, M., Prasad, P., Dorji, J., & Zahra, T. (2018). Serviceability Assessment of Masonry Arch Bridges Using Digital Image Correlation. *J. Bridge Eng.*, 24(2), 04018120. doi: 10.1061/(ASCE)BE.1943-5592.0001341.

Federal Highway Administration (FHWA). (2004). *National bridge inspection standards*, Federal Register, 69 (239).

Fisher, J. W. (1984). *Fatigue and fracture in steel bridges. Case studies*. J. Wiley and Sons, Limited; Sussex, England.

Hamam, R., Hild, F., & Roux, S. (2007). Stress Intensity Factor Gauging by Digital Image Correlation: Application in Cyclic Fatigue. *Strain*, 43(3), 181-192. doi: 10.1111/j.1475-1305.2007.00345.x.

Harilal, R., & Ramji, M. (2014). Adaptation of Open Source 2D DIC Software Ncorr for Solid Mechanics Applications. *International Symposium on Advanced Science and Technology in Experimental Mechanics*. doi: 10.13140/2.1.4994.1442.

Helfrick, M. N., Niezrecki, C., Avitabile, P., & Schmidt, T. (2011). 3D digital image correlation methods for full-field vibration measurement. *Mech. Systems and Signal Processing*, 25(3), 917-927. doi: 10.1016/j.ymssp.2010.08.013.

Helm, J. D. (1996). Improved three-dimensional image correlation for surface displacement measurement. *Opt. Eng.*, 35(7), 1911. doi: 10.1117/1.600624.

Hutt, T., & Cawley, P. (2009). Feasibility of digital image correlation for detection of cracks at fastener holes. *NDT & E International*. 42, 141-149. doi: 10.1016/j.ndteint.2008.10.008.

International Digital Image Correlation Society, Jones, E. M. C., & Iadicola, M. A. (Eds.). (2018). A Good Practice Guide for Digital Image Correlation. doi: 10.32720/idics/gpg.ed1.

Kong, X., & Li, J. (2018). Vision-based Fatigue Crack Detection of Steel Structures Using Video Feature Tracking. *Comp.-Aided Civil Infrastruct. Eng.*, 33(9), 783-799.

Küntz, M., Jolin, M., Bastien, J., Perez, F., & Hild, F. (2006). Digital image correlation analysis of crack behavior in a reinforced concrete beam during a load test. *Canadian J. Civil Eng.*, 33(11), 1418-1425. doi: 10.1139/l06-106.

Lee, J. J., & Shinozuka, M. (2006). A vision-based system for remote sensing of bridge displacement. *NDT & E International*, 39(5), 425-431. doi: 10.1016/j.ndteint.2005.12.003.

Lorenzino, P., Beretta, G., & Navarro, A. (2014). Application of Digital Image Correlation (DIC) in resonance machines for measuring fatigue crack growth. *Frattura ed Integrità Strutturale*. 30, 369-374. doi: 10.3221/IGF-ESIS.30.44.

Nowell, D., Paynter, R. J., & Matos, P. F. (2010). Optical methods for measurement of fatigue crack closure: Moiré interferometry and digital image correlation. *Fatigue & Fracture Eng. Mat. & Structures*, 33(12), 778-790. doi: 10.1111/j.1460-2695.2010.01447.x.

Pan, B., Tian, L., & Song, X. (2016). Real-time, non-contact and targetless measurement of vertical deflection of bridges using off-axis digital image correlation. *NDT & E International*, 79, 73-80. doi: 10.1016/j.ndteint.2015.12.006.

Passieux, J., and Bouclier, R. (2019). Classic and Inverse Compositional Gauss-Newton in Global DIC. *Int. J. Num. Methods Eng.*, 119(6), 453-468. doi: 10.1002/nme.6057.

Reagan, D., Sabato, A., & Niezrecki, C. (2018). Feasibility of using digital image correlation for unmanned aerial vehicle structural health monitoring of bridges. *Structural Health Monitoring*, *17*(5), 1056–1072. doi: 10.1177/1475921717735326.

Ribeiro, D., Calçada, R., Ferreira, J., & Martins, T. (2014). Non-contact measurement of the dynamic displacement of railway bridges using an advanced video-based system. *Eng. Structures*, 75, 164-180. doi: 10.1016/j.engstruct.2014.04.051.

Rupil, J., Roux, S., Hild, F., & Vincent, L. (2011). Fatigue microcrack detection with digital image correlation. *J. Strain Analysis Eng. Design*. 46. 492-509. doi: 10.1177/0309324711402764.

Sutton, M. A., Yan, J. H., Deng, X., Cheng, C. S., & Zavattieri, P. (2007). Three-dimensional digital image correlation to quantify deformation and crack-opening displacement in ductile aluminum under mixed-mode I/III loading. *Opt. Eng.*, 46(5), 051003. doi: 10.1117/1.2741279.

Turner, D. Z. (2015.) Digital Image Correlation Engine (DICe) Reference Manual. Sandia Nat. Lab.: Livermore, California, USA. http://dicengine.github.io/dice/.

Vanlanduit, S., Vanherzeele, R., Longo, R., & Guillaume, P. (2008). Investigation of fatigue cracks using digital image correlation. *Emerging Technologies in NDT*. 4, 53-58.

Vanlanduit, S., Vanherzeele, R., Longo, R., & Guillaume, P. (2009). A digital image correlation method for fatigue test experiments. *Opt. Lasers Eng.*, 47(3-4), 371-378. doi: 10.1016/j.optlasend.2008.03.016.

Wang, B., & Pan, B. (2016). Subset-based vs. finite element-based global digital image correlation: A comparison study. *Theoretical and Applied Mechanics Letters*, 6. doi: 10.1016/j.taml.2016.08.003.

Whitehead, J. (2015). "Probability of detection study for visual inspection of steel bridges." Master's Thesis, Purdue University, West Lafayette, IN.

Yamaguchi, T., & Hashimoto, S. (2010). Fast crack detection method for large-size concrete surface images using percolation-based image processing. *Machine Vision and Applications*, 21(5), 797-809.

Yang, J., & Bhattacharya, K. (2020). Augmented Lagrangian Digital Image Correlation (AL-DIC) Code Manual. CaltechDATA. doi: 10.22002/D1.1443.

Yeum, C. M., & Dyke, S. J. (2015). Vision-based automated crack detection for bridge inspection. *Comp.-Aided Civil Infrastruct. Eng.*, 30(10), 759-770.

Yu, S. N., Jang, J. H., & Han, C. S. (2007). Auto inspection system using a mobile robot for detecting concrete cracks in a tunnel. *Automation in Construction*, 16(3), 255-261.

Yuan, Y., Huang, J., Peng, X., Xiong, C., Fang, J., & Yuan, F. (2014). Accurate displacement measurement via a self-adaptive digital image correlation method based on a weighted ZNSSD criterion. *Opt. Lasers Eng.*, 52, 75-85. doi: 10.1016/j.optlaseng.2013.07.016.

Zhang, R., & He, L. (2012). Measurement of mixed-mode stress intensity factors using digital image correlation method. *Opt. Lasers Eng.*, 50(7), 1001-1007. doi: 10.1016/j.optlaseng.2012.01.009.

Zhao Z., & Haldar, A. (1996). Bridge fatigue damage evaluation and updating using non-destructive inspections. *Eng. Fracture Mech.*, 53(5), 775-88.

Zhao, Y., & Roddis, W. M. K. (2004). Fatigue Prone Steel Bridge Details: Investigation and Recommended Repairs, *K-TRAN: KU-99-2, Final Report.* Kansas Department of Transportation, Topeka, KS.

Zou, Q., Cao, Y., Li, Q., Mao, Q., & Wang, S. (2012). CrackTree: Automatic crack detection from pavement images. *Pattern Recognition Letters*, 33(3), 227-238.

Appendix A Light, Focus, and Aperture Testing

Table A.1 shows the light and focus conditions for a distance between the camera of 216 mm (8.5 in.). Table A.2 shows the light and focus conditions for a distance between the camera of 432 mm (17.0 in.).

Table A.1 Light and focus conditions for 216 mm (8.5 in.) camera distance

| Condition | Focus | Focal Length, mm (in.) | Lighting | Light Range, lumens |
|-----------|-------|------------------------|----------|---------------------|
| 1 | Ideal | 216 (8.5) | High | 5850 – 6600 |
| 2 | Ideal | 216 (8.5) | Medium | 4450 – 5000 |
| 3 | Ideal | 216 (8.5) | Low | 2000 – 2350 |
| 4 | Fair | 205 (8.1) | High | 5850 – 6600 |
| 5 | Fair | 205 (8.1) | Medium | 4450 – 5000 |
| 6 | Poor | 195 (7.7) | High | 5850 – 6600 |

Table A.2 Light and focus conditions for 432 mm (17.0 in.) camera distance

| Condition | Focus | Focal Length, mm (in.) | Lighting | Light Range, lumens |
|-----------|-------|------------------------|----------|---------------------|
| 1 | Ideal | 432 (17.0) | High | 5850 – 6600 |
| 2 | Ideal | 432 (17.0) | Medium | 4450 – 5000 |
| 3 | Ideal | 432 (17.0) | Low | 2000 – 2350 |
| 4 | Fair | 410 (16.2) | High | 5850 – 6600 |
| 5 | Fair | 410 (16.2) | Medium | 4450 – 5000 |
| 6 | Poor | 389 (15.3) | High | 5850 – 6600 |

Figures A.1 to A.20 show the convergence of relative displacement for different crack lengths when the camera was 648 mm (25.5 in.) from the specimen. Each figure shows all lighting and focus data for a given load case and crack length. Figures A.21 to A.30 show the convergence plots for a camera to specimen distance of 432 mm (17.0 in.). Figures A.31 to A.40

show the convergence plots for a camera to specimen distance of 216 mm (8.5 in.). The vertical
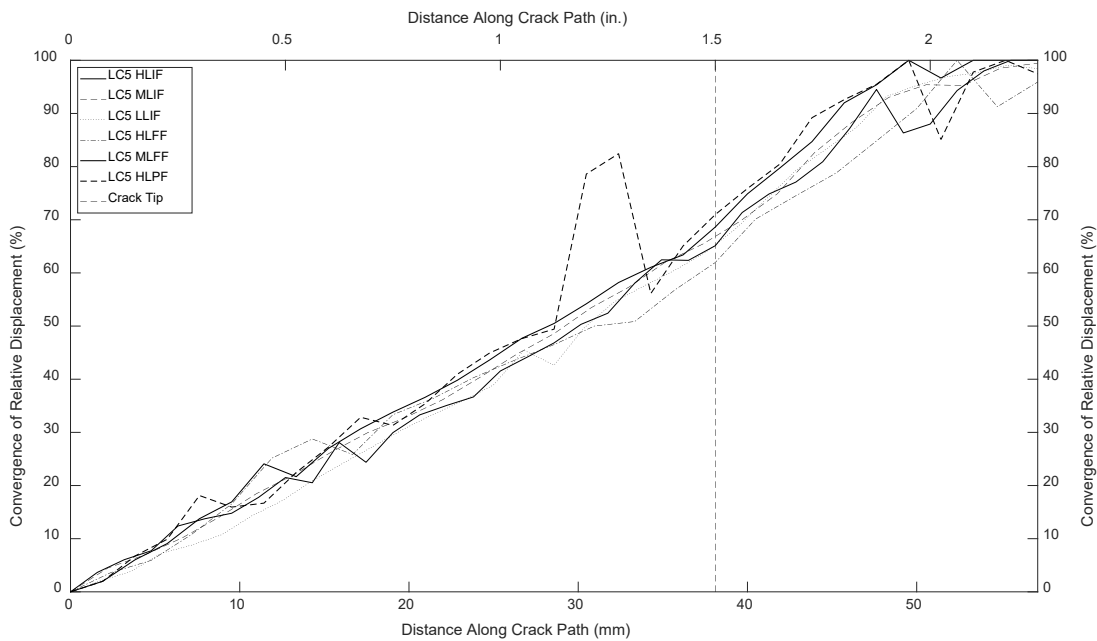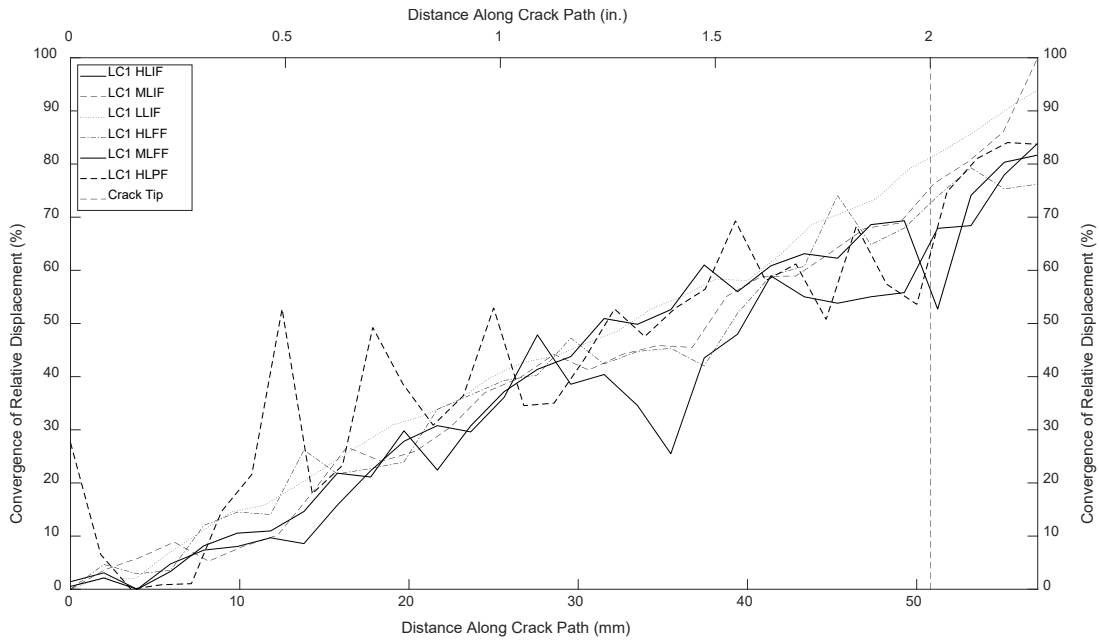
dotted line represents the actual crack length.
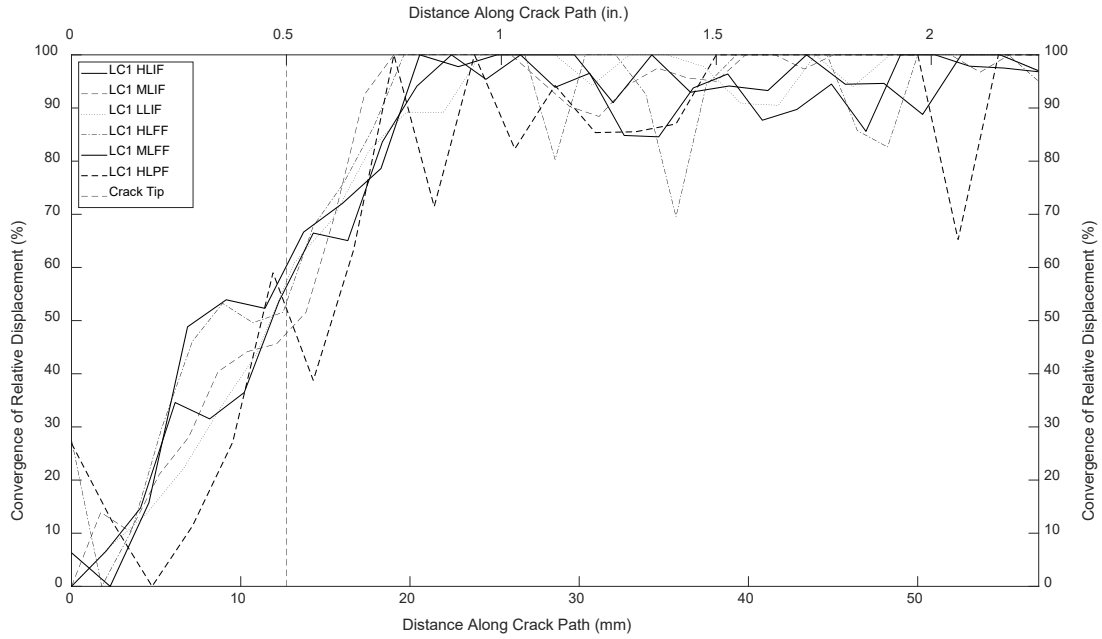


Figure A.1 Convergence of relative displacement of a 12.7 mm (0.5 in.) crack with a camera
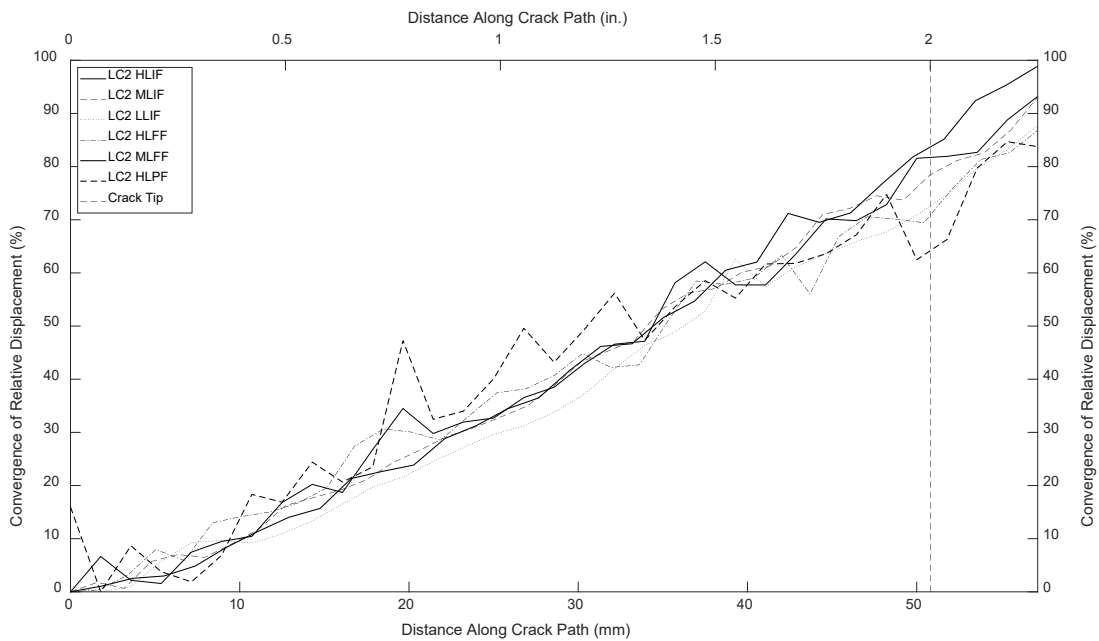distance of 648 mm (25.5 in.) under LC1
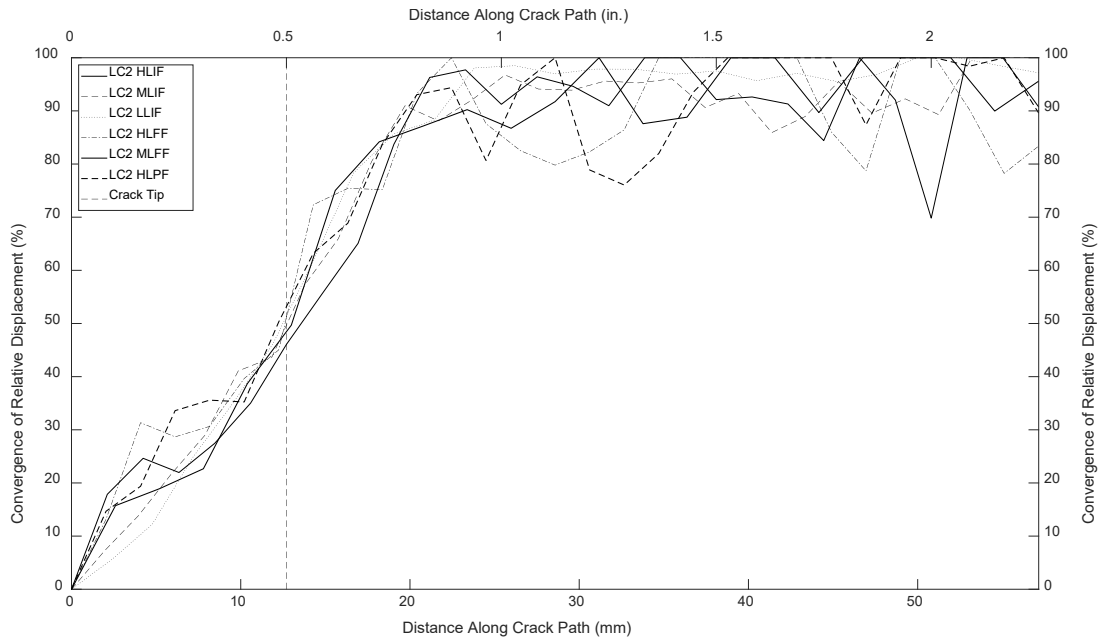
Figure A.2 Convergence of relative displacement of a 12.7 mm (0.5 in.) crack with a camera distance of 648 mm (25.5 in.) under LC2
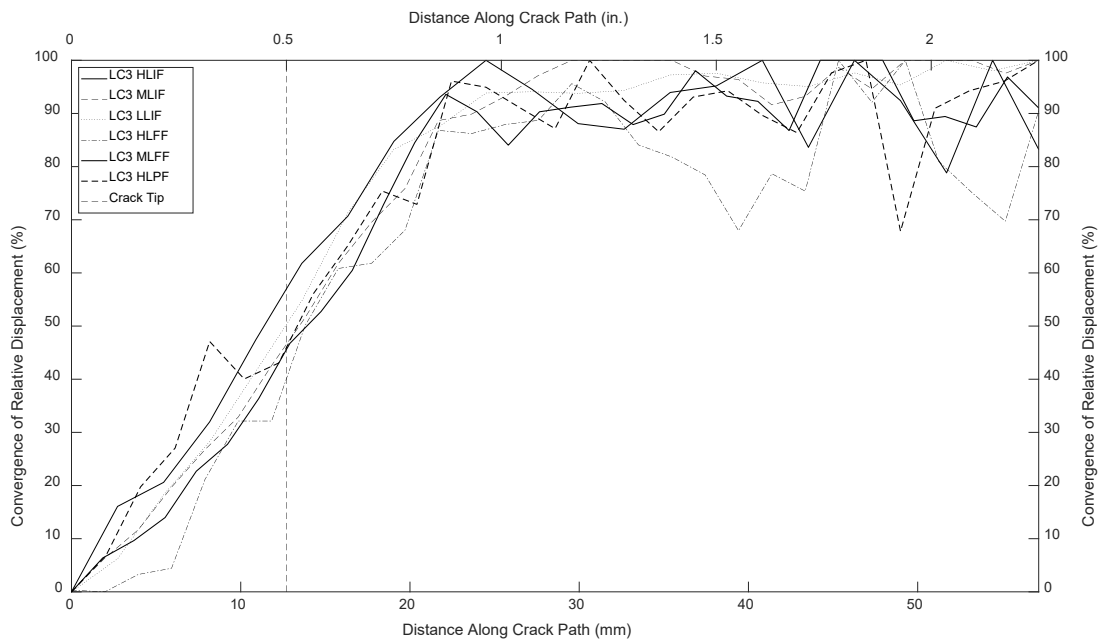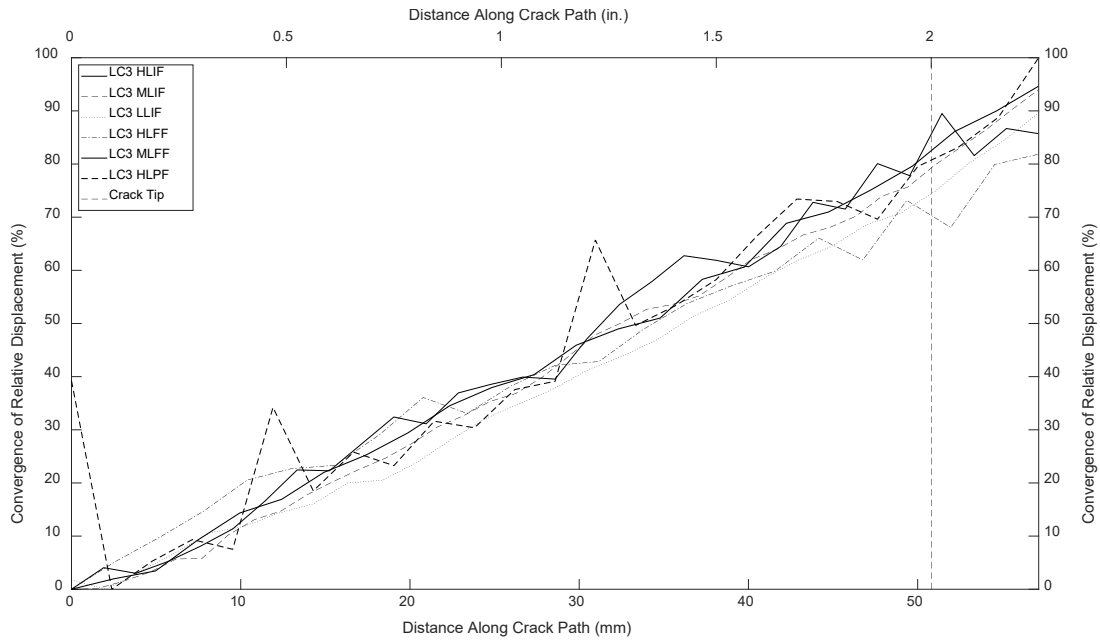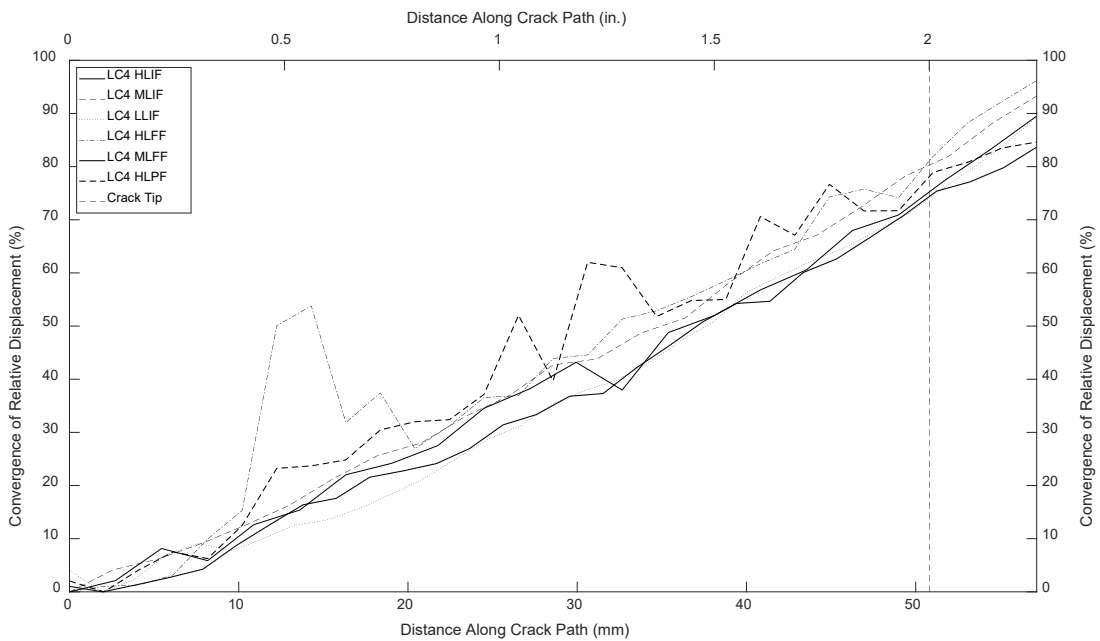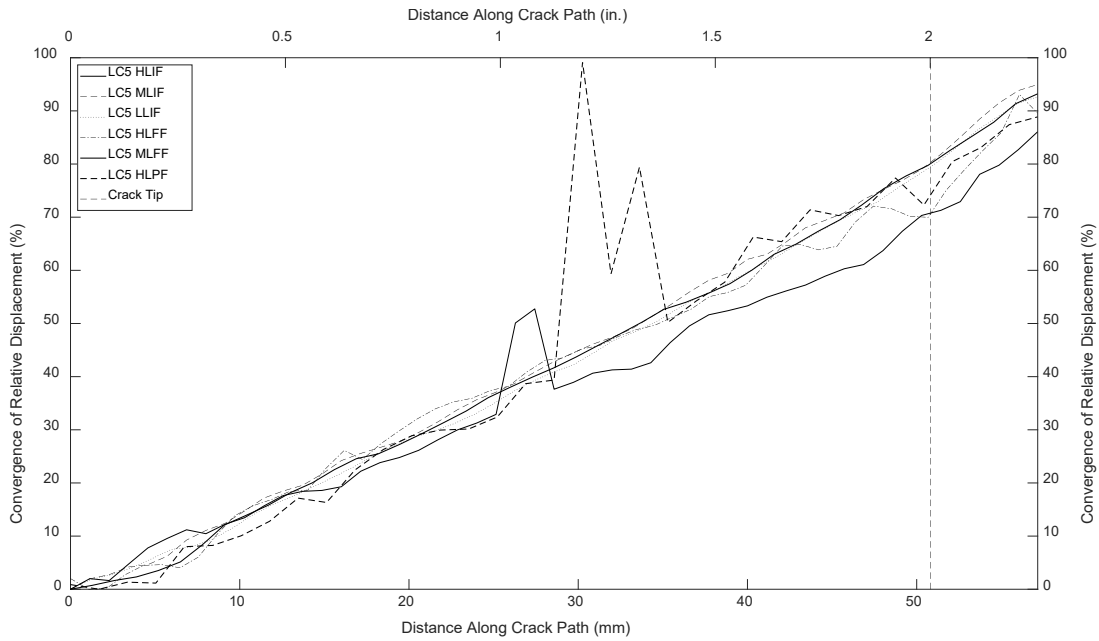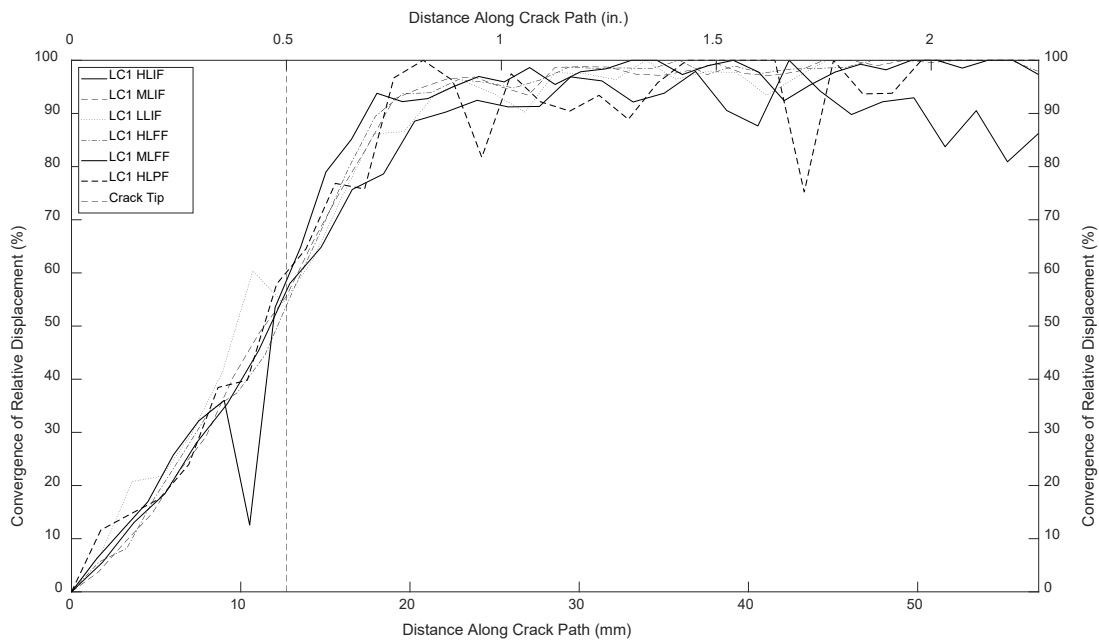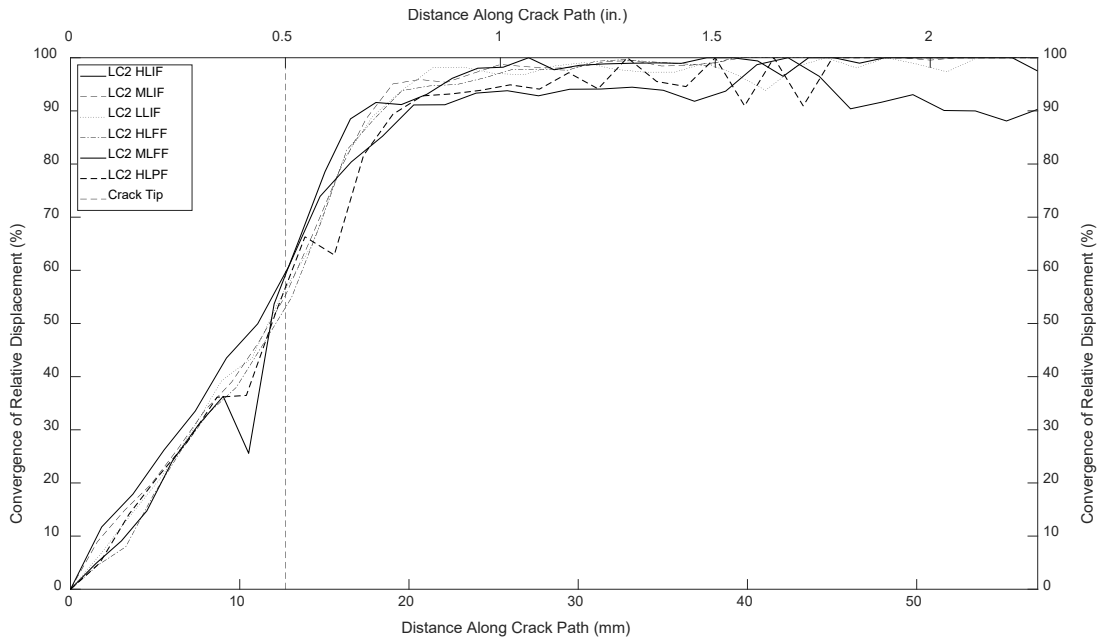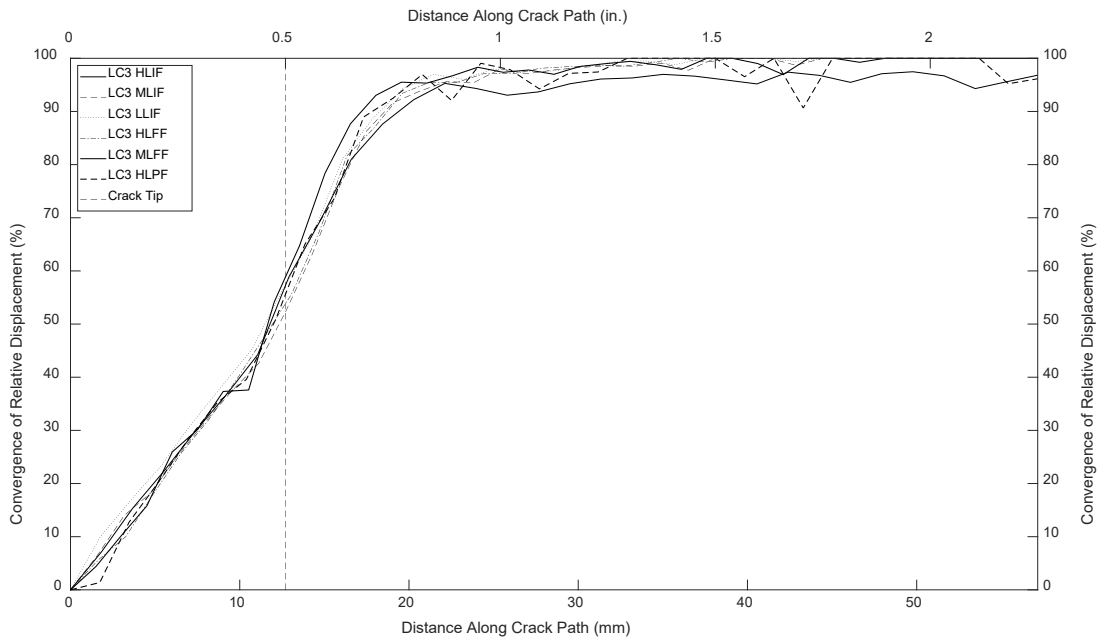


Figure A.3 Convergence of relative displacement of a 12.7 mm (0.5 in.) crack with a camera distance of 648 mm (25.5 in.) under LC3
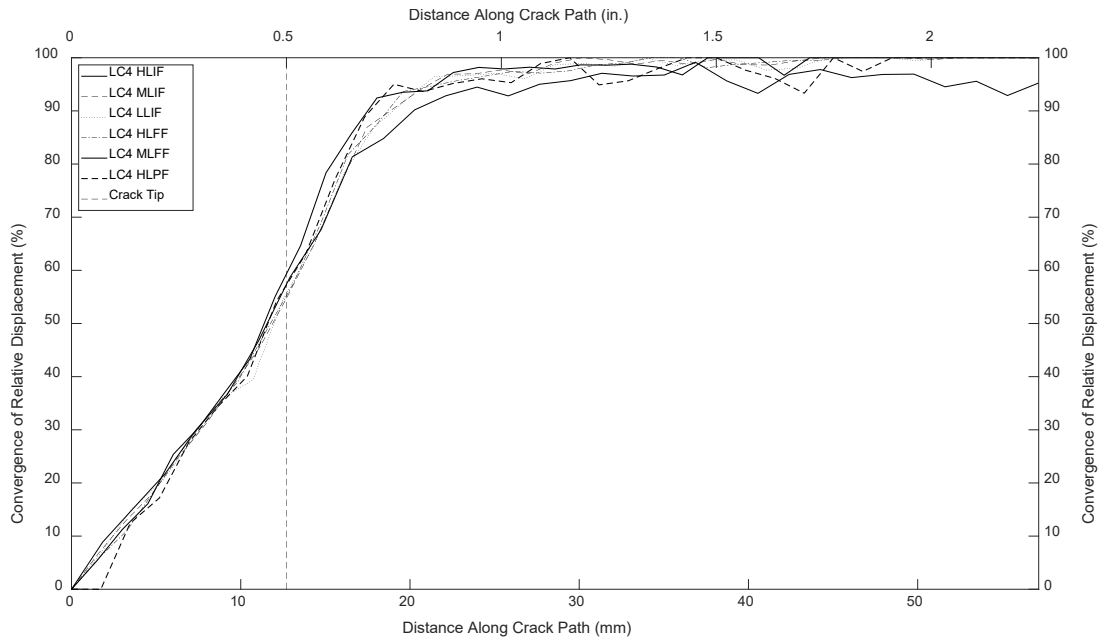
55
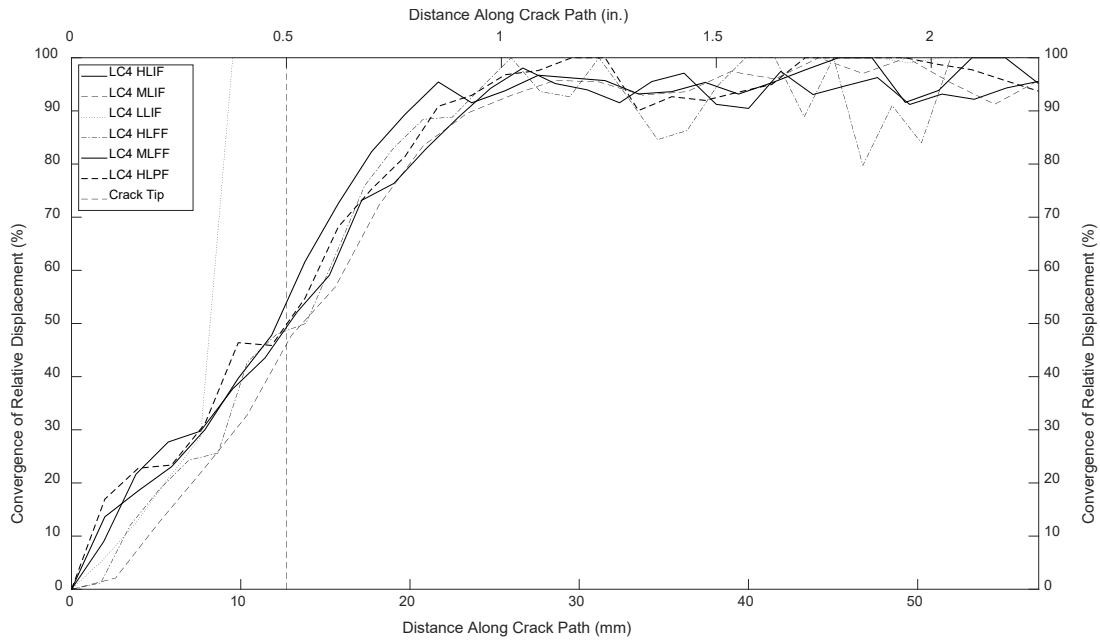
Figure A.4 Convergence of relative displacement of a 12.7 mm (0.5 in.) crack with a camera distance of 648 mm (25.5 in.) under LC4
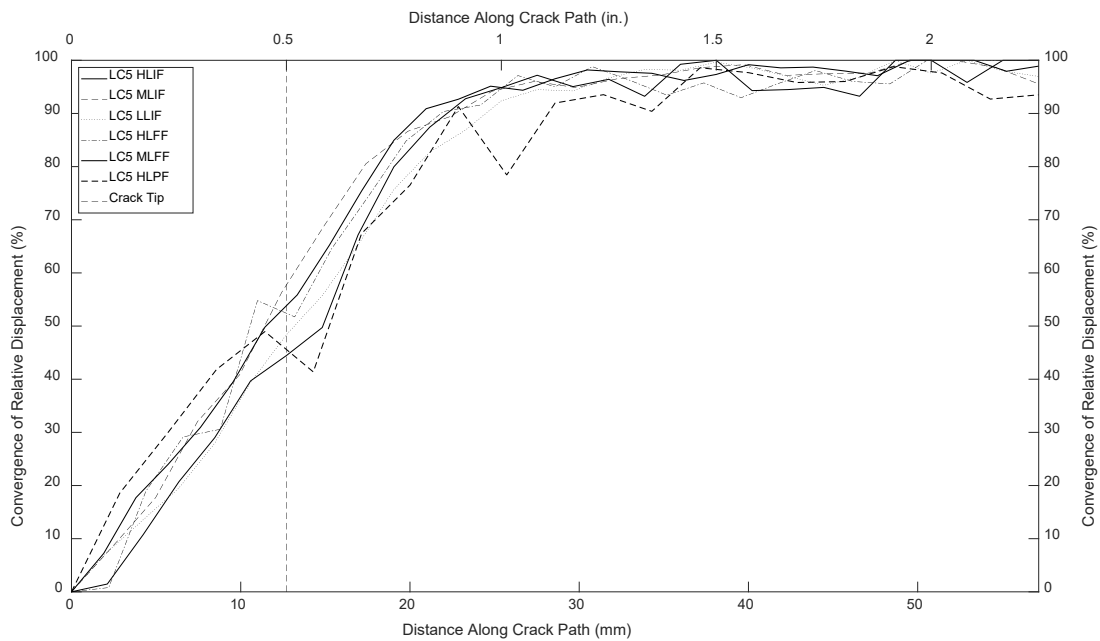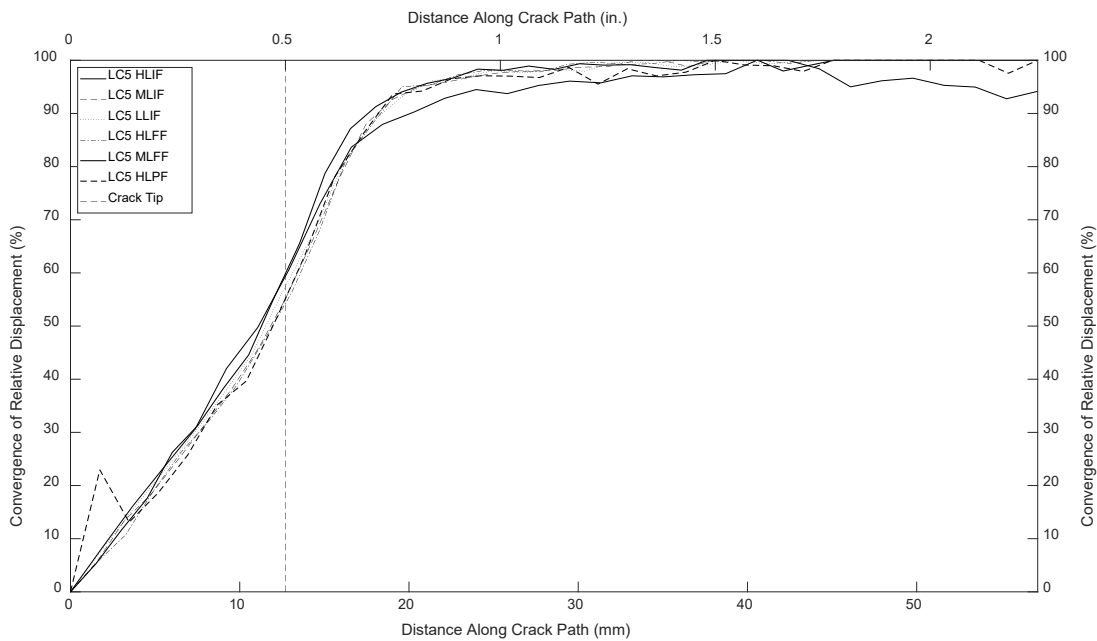


Figure A.5 Convergence of relative displacement of a 12.7 mm (0.5 in.) crack with a camera distance of 648 mm (25.5 in.) under LC5
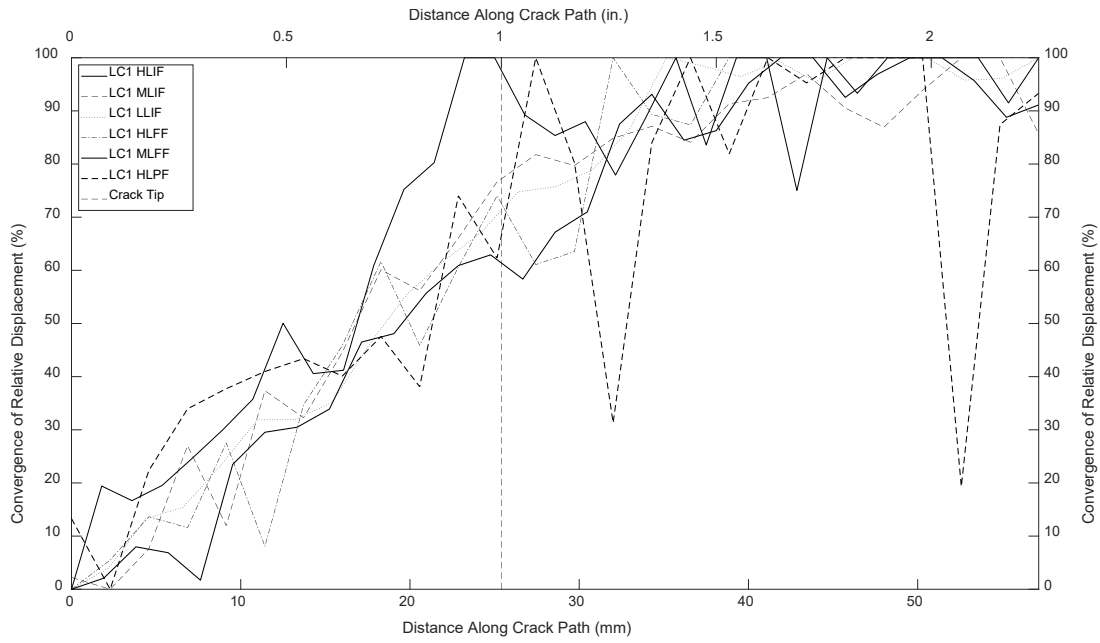
Figure A.6 Convergence of relative displacement of a 25.4 mm (1.0 in.) crack with a camera distance of 648 mm (25.5 in.) under LC1
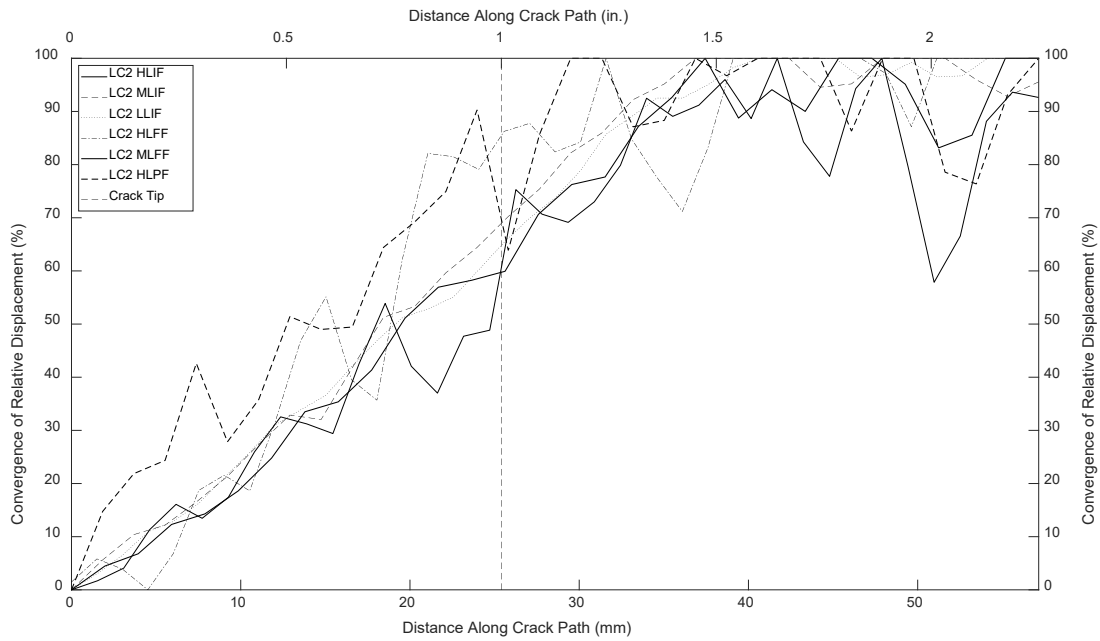


Figure A.7 Convergence of relative displacement of a 25.4 mm (1.0 in.) crack with a camera distance of 648 mm (25.5 in.) under LC2
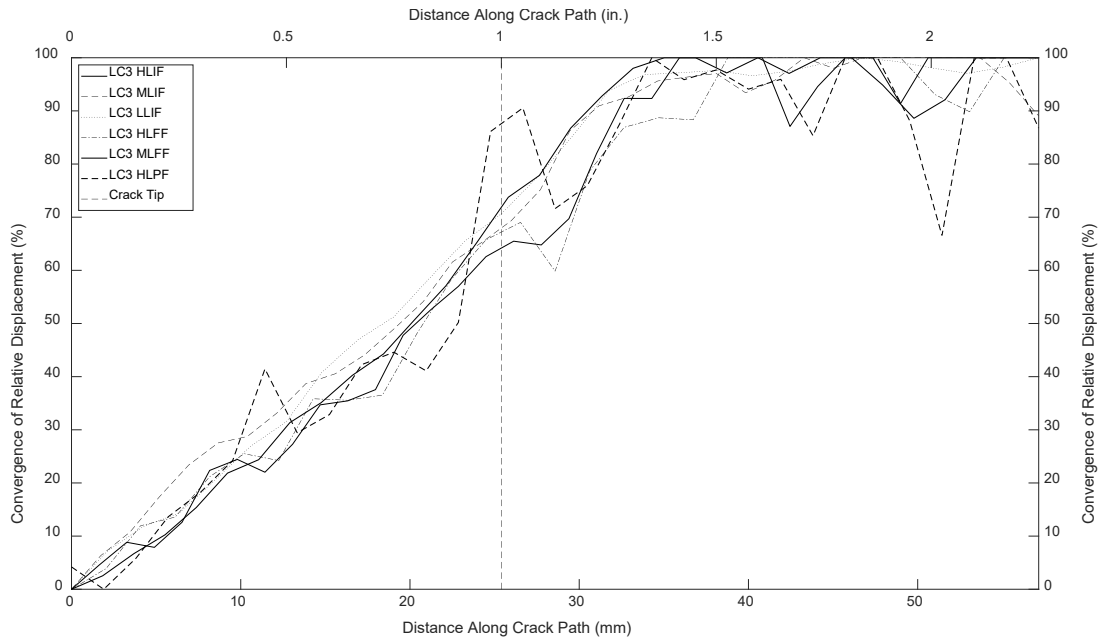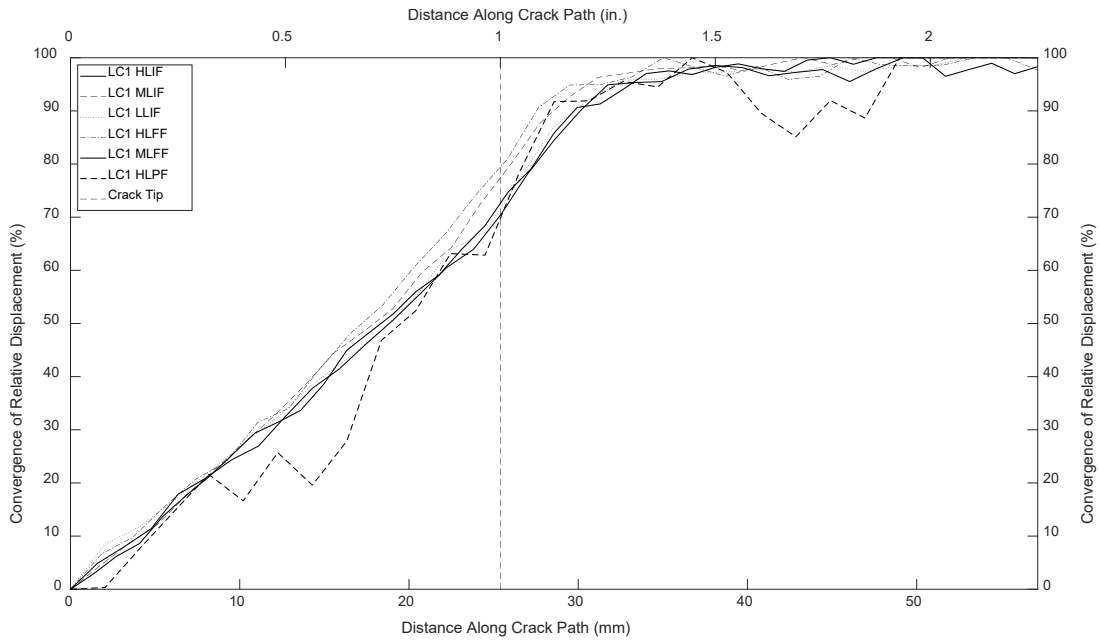
Figure A.8 Convergence of relative displacement of a 25.4 mm (1.0 in.) crack with a camera distance of 648 mm (25.5 in.) under LC3
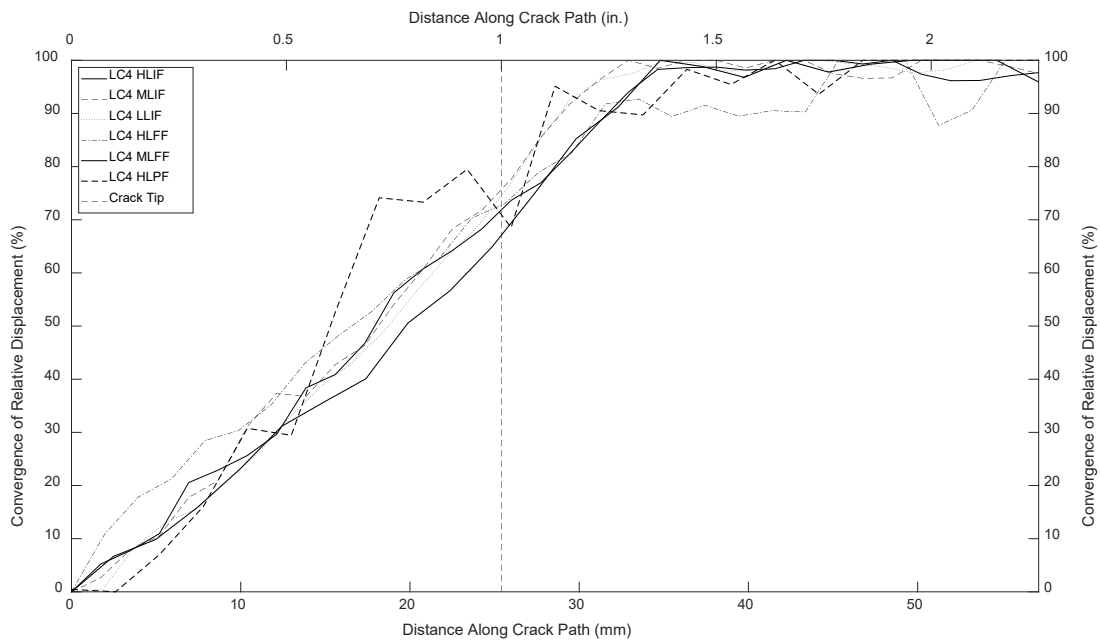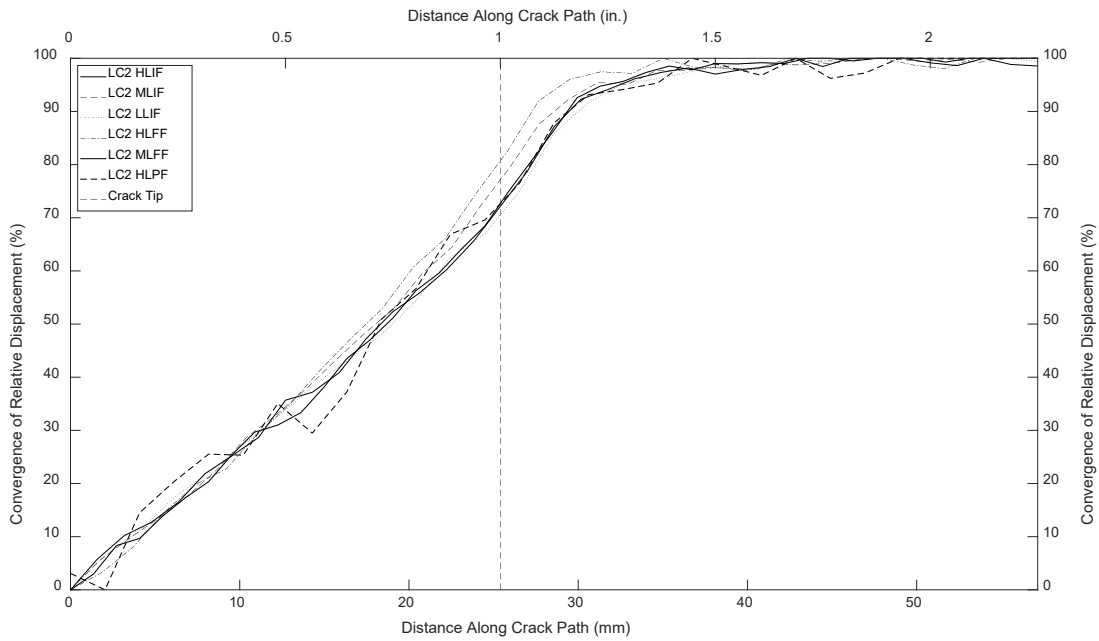


Figure A.9 Convergence of relative displacement of a 25.4 mm (1.0 in.) crack with a camera distance of 648 mm (25.5 in.) under LC4
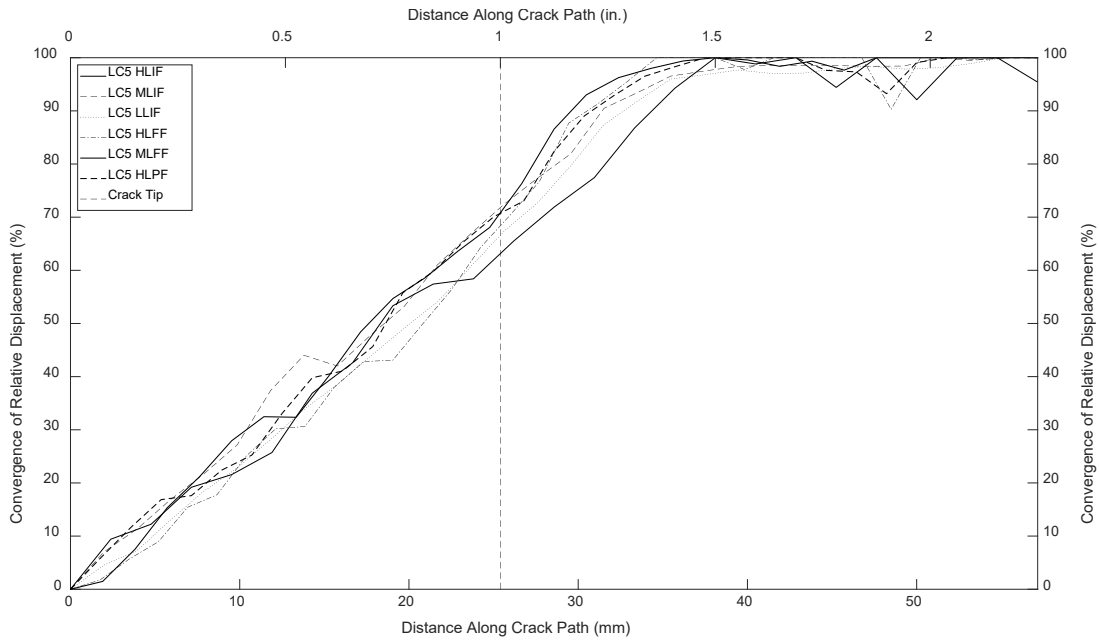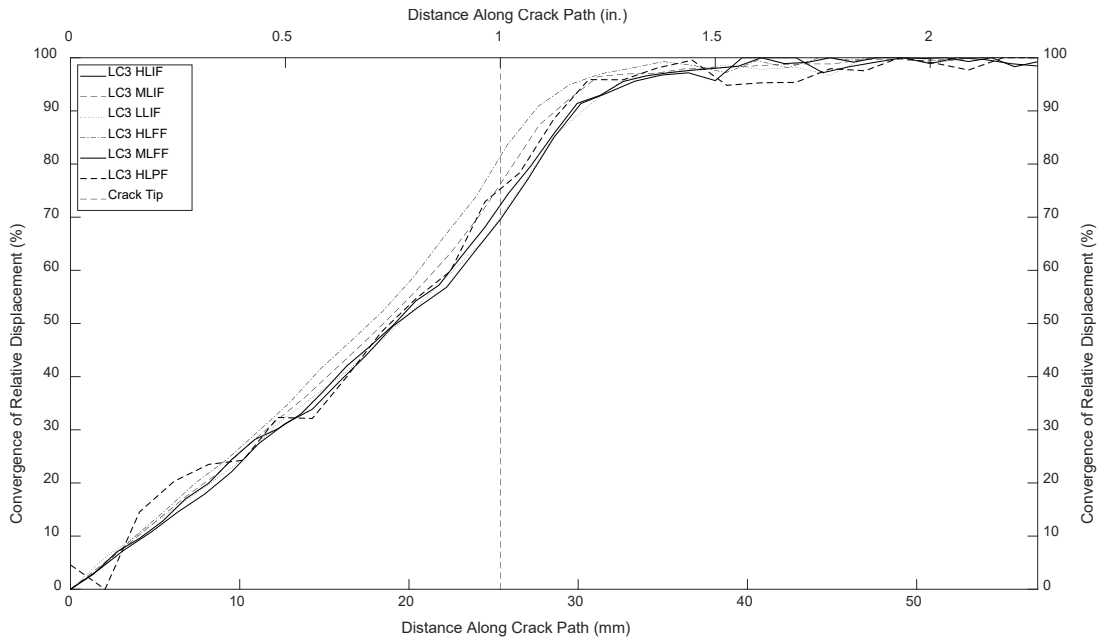
Figure A.10 Convergence of relative displacement of a 25.4 mm (1.0 in.) crack with a camera distance of 648 mm (25.5 in.) under LC5
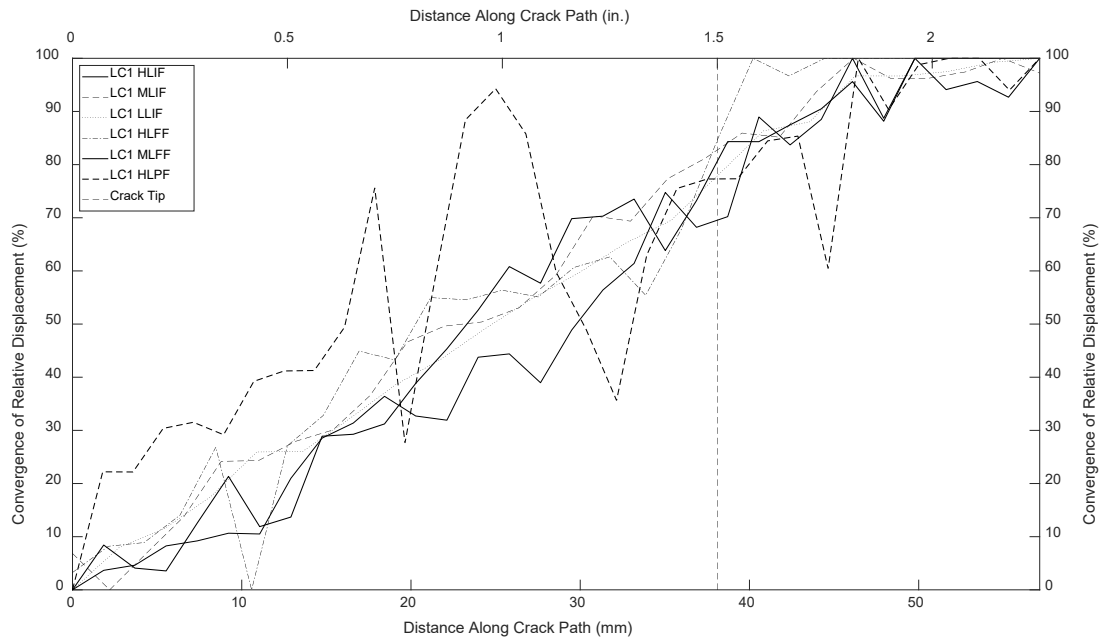


Figure A.11 Convergence of relative displacement of a 38.1 mm (1.5 in.) crack with a camera distance of 648 mm (25.5 in.) under LC1
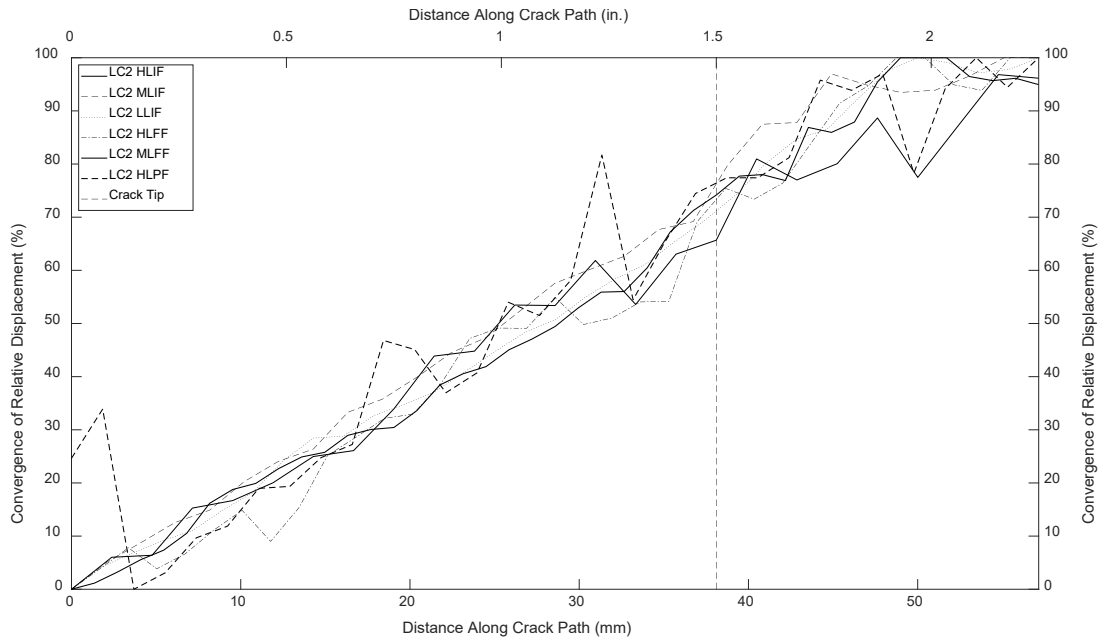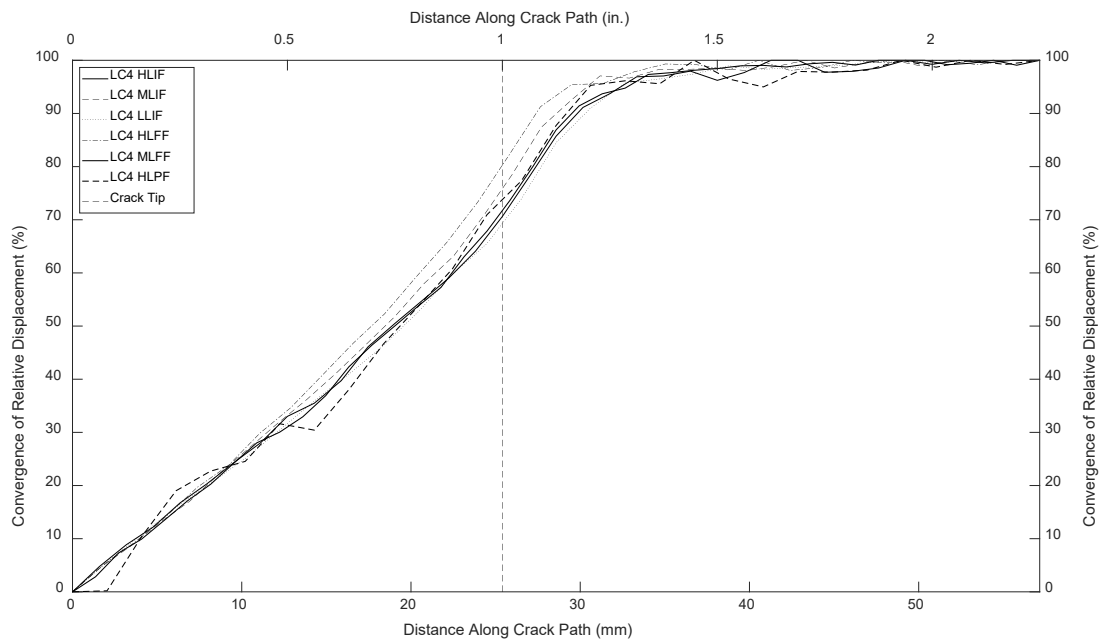
Figure A.12 Convergence of relative displacement of a 38.1 mm (1.5 in.) crack with a camera distance of 648 mm (25.5 in.) under LC2
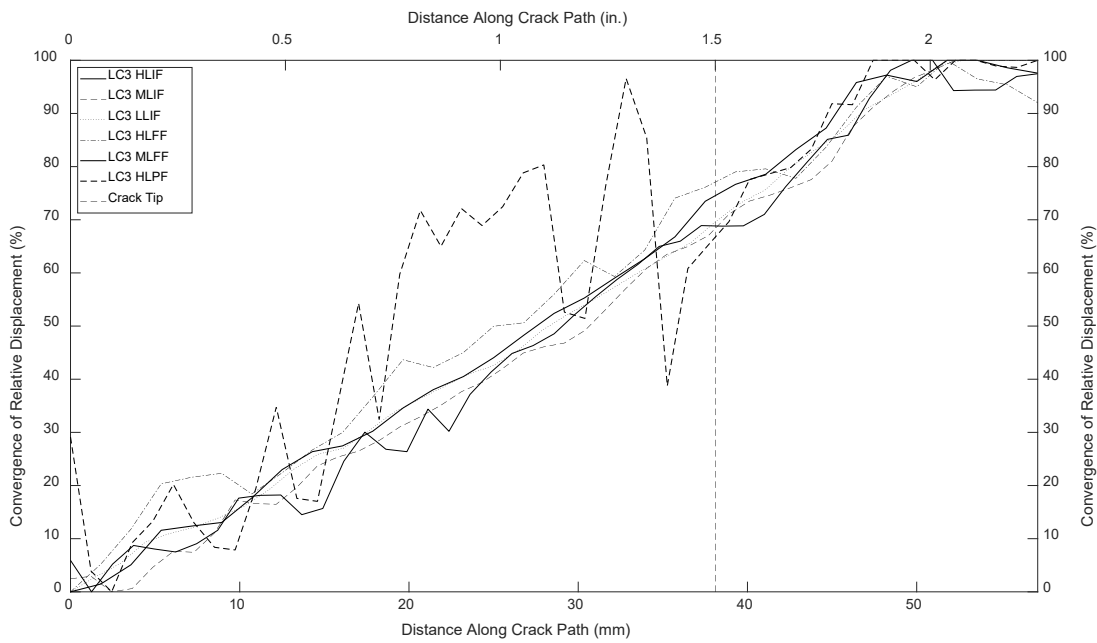


Figure A.13 Convergence of relative displacement of a 38.1 mm (1.5 in.) crack with a camera distance of 648 mm (25.5 in.) under LC3
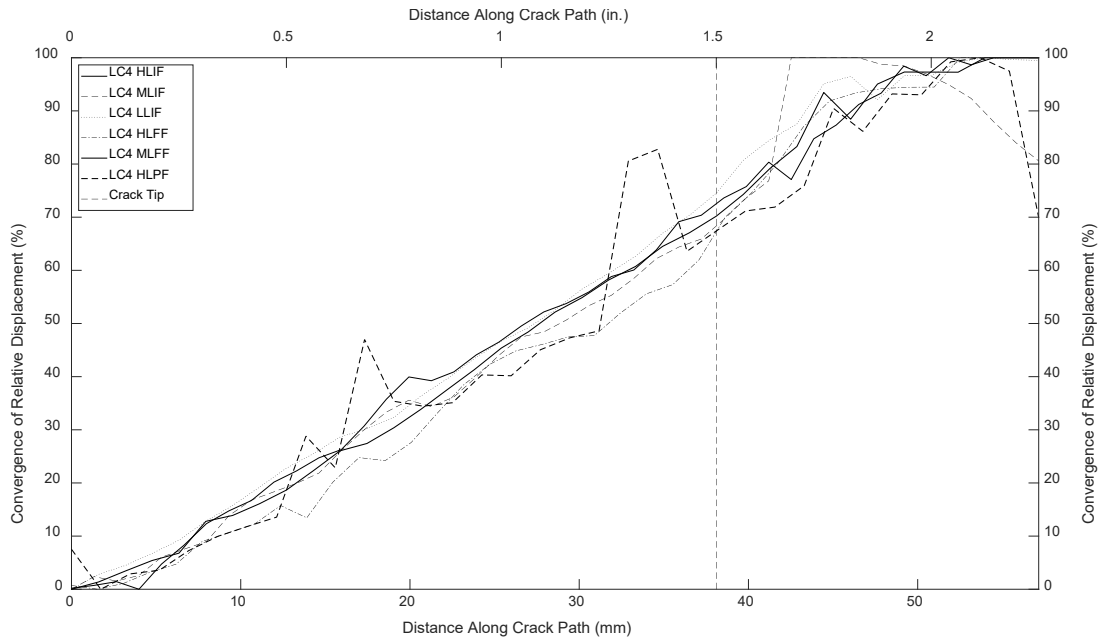
Figure A.14 Convergence of relative displacement of a 38.1 mm (1.5 in.) crack with a camera distance of 648 mm (25.5 in.) under LC4
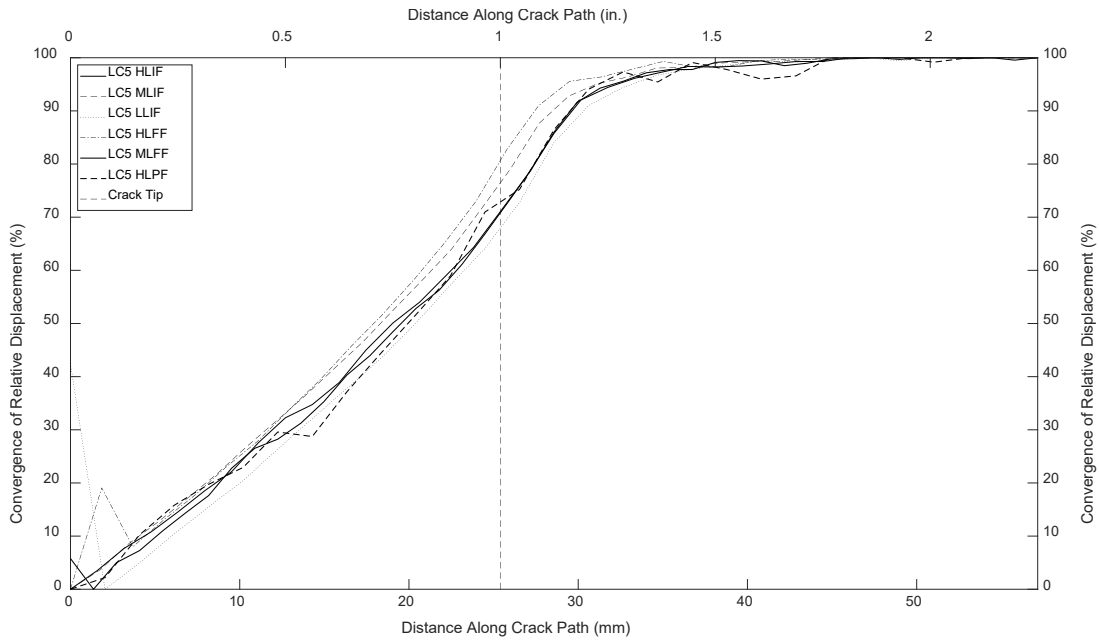


Figure A.15 Convergence of relative displacement of a 38.1 mm (1.5 in.) crack with a camera distance of 648 mm (25.5 in.) under LC5

Figure A.16 Convergence of relative displacement of a 50.8 mm (2.0 in.) crack with a camera distance of 648 mm (25.5 in.) under LC1
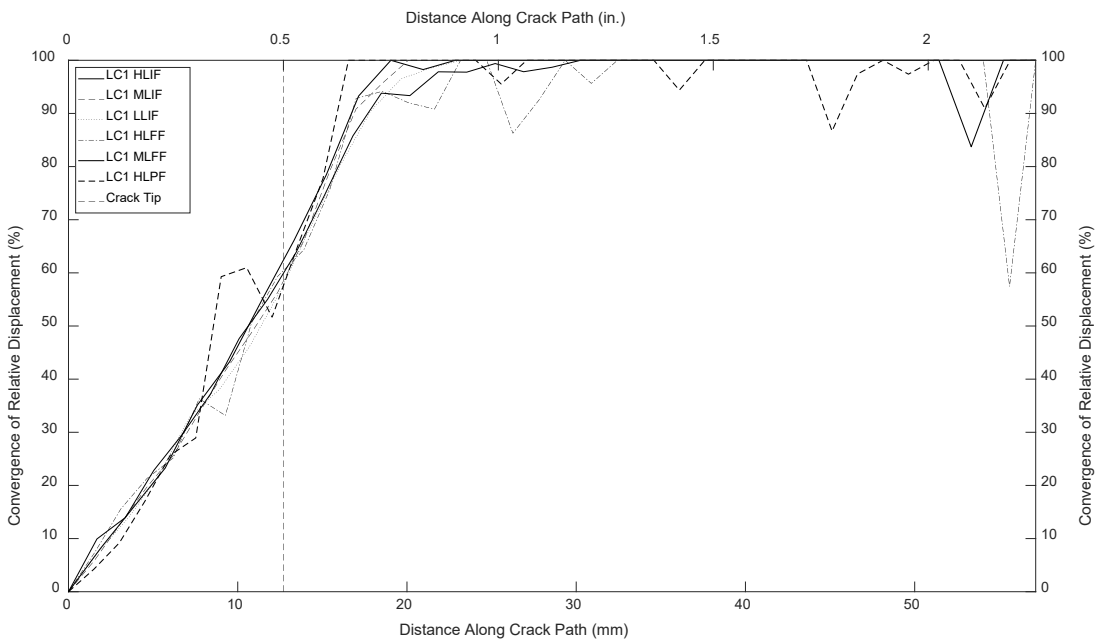


Figure A.17 Convergence of relative displacement of a 50.8 mm (2.0 in.) crack with a camera distance of 648 mm (25.5 in.) under LC2

Figure A.18 Convergence of relative displacement of a 50.8 mm (2.0 in.) crack with a camera distance of 648 mm (25.5 in.) under LC3



Figure A.19 Convergence of relative displacement of a 50.8 mm (2.0 in.) crack with a camera distance of 648 mm (25.5 in.) under LC4

Figure A.20 Convergence of relative displacement of a 50.8 mm (2.0 in.) crack with a camera distance of 648 mm (25.5 in.) under LC5



Figure A.21 Convergence of relative displacement of a 12.7 mm (0.5 in.) crack with a camera distance of 432 mm (17.0 in.) under LC1
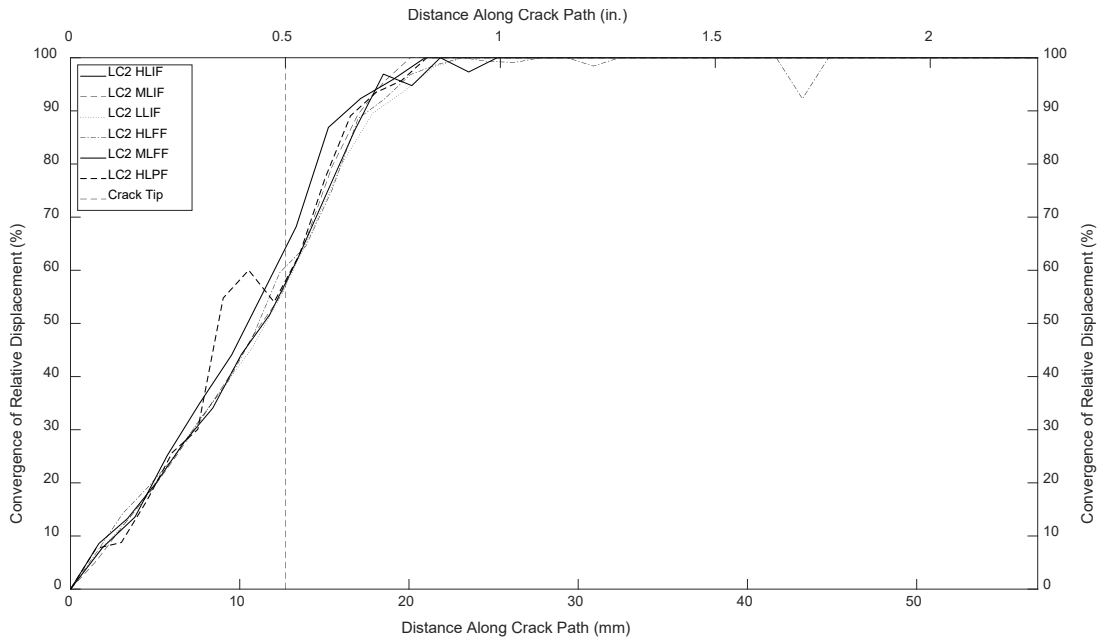
Figure A.22 Convergence of relative displacement of a 12.7 mm (0.5 in.) crack with a camera distance of 432 mm (17.0 in.) under LC2
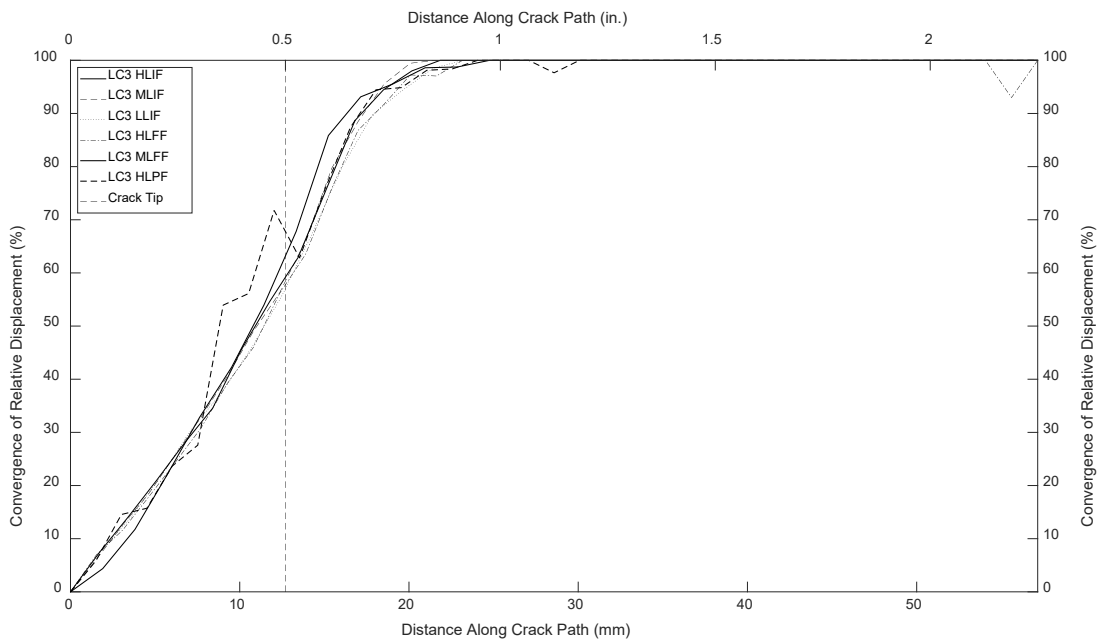


Figure A.23 Convergence of relative displacement of a 12.7 mm (0.5 in.) crack with a camera distance of 432 mm (17.0 in.) under LC3
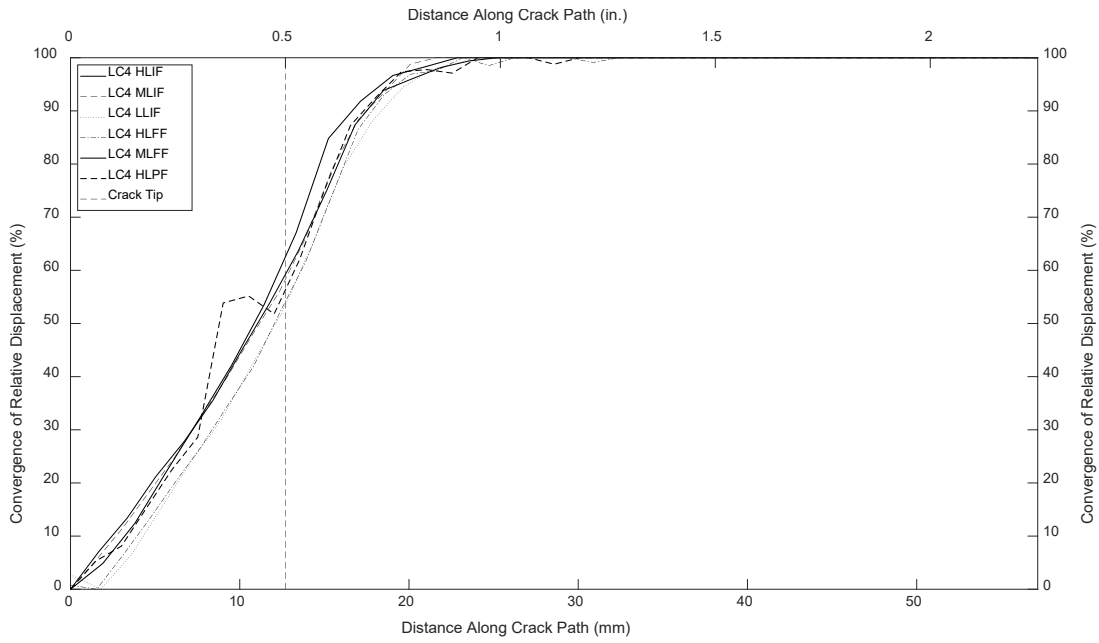
Figure A.24 Convergence of relative displacement of a 12.7 mm (0.5 in.) crack with a camera distance of 432 mm (17.0 in.) under LC4
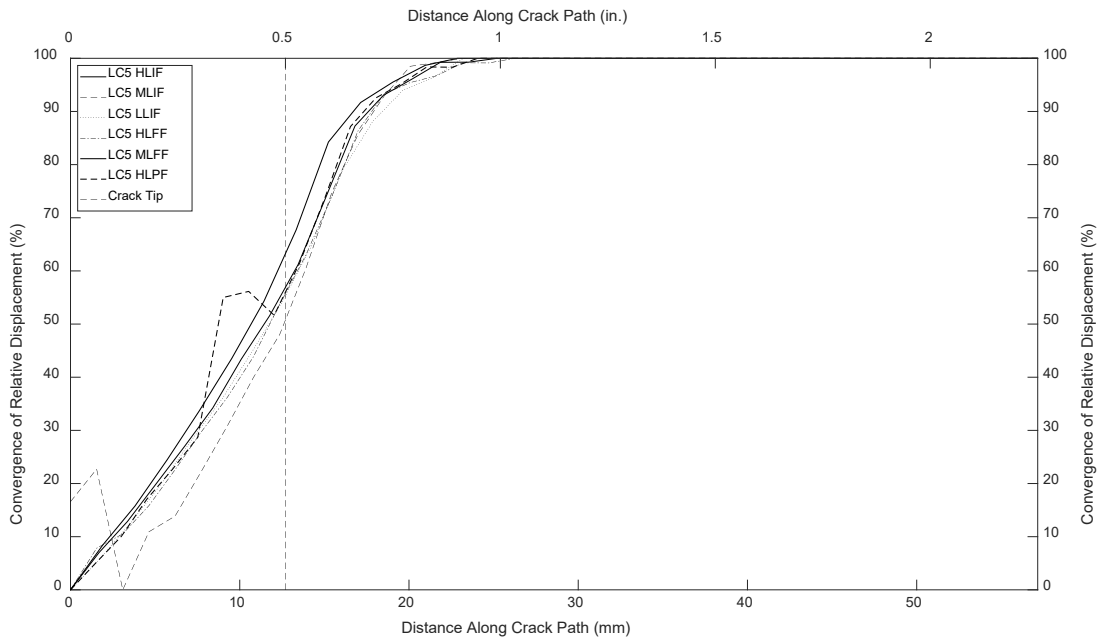


Figure A.25 Convergence of relative displacement of a 12.7 mm (0.5 in.) crack with a camera distance of 432 mm (17.0 in.) under LC5
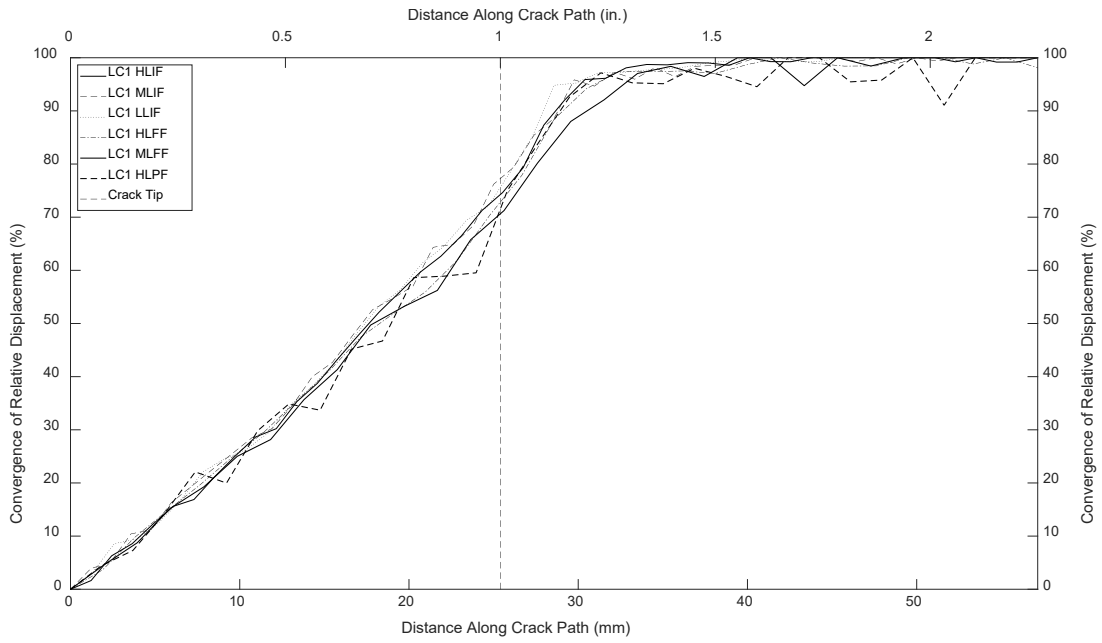
Figure A.26 Convergence of relative displacement of a 25.4 mm (1.0 in.) crack with a camera distance of 432 mm (17.0 in.) under LC1
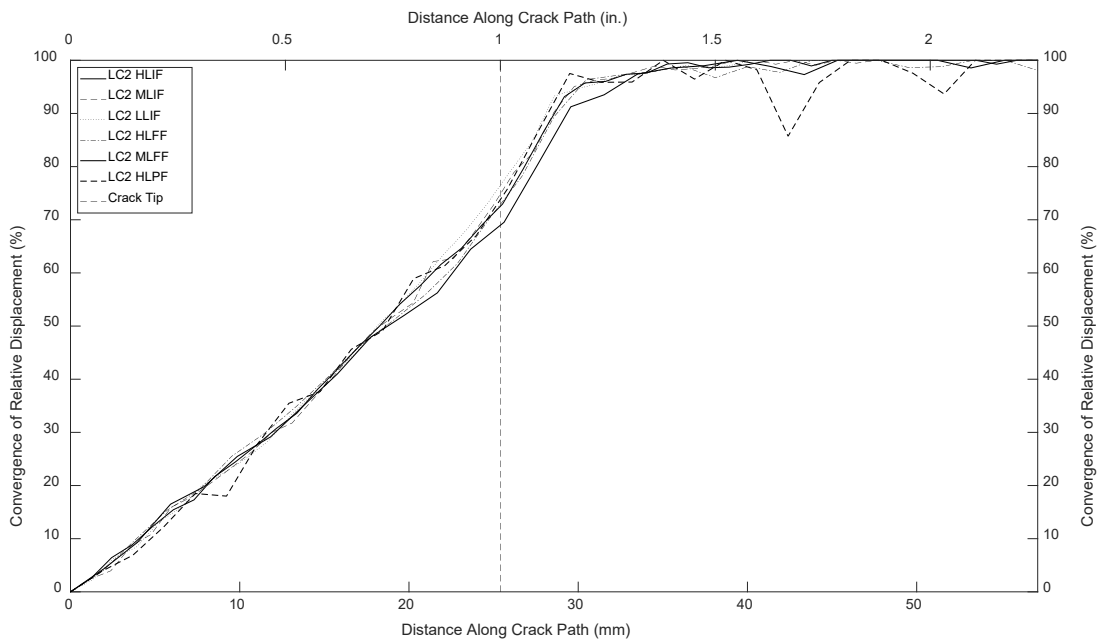


Figure A.27 Convergence of relative displacement of a 25.4 mm (1.0 in.) crack with a camera distance of 432 mm (17.0 in.) under LC2

Figure A.28 Convergence of relative displacement of a 25.4 mm (1.0 in.) crack with a camera distance of 432 mm (17.0 in.) under LC3



Figure A.29 Convergence of relative displacement of a 25.4 mm (1.0 in.) crack with a camera distance of 432 mm (17.0 in.) under LC4

Figure A.30 Convergence of relative displacement of a 25.4 mm (1.0 in.) crack with a camera distance of 432 mm (17.0 in.) under LC5



Figure A.31 Convergence of relative displacement of a 12.7 mm (0.5 in.) crack with a camera distance of 216 mm (8.5 in.) under LC1

Figure A.32 Convergence of relative displacement of a 12.7 mm (0.5 in.) crack with a camera
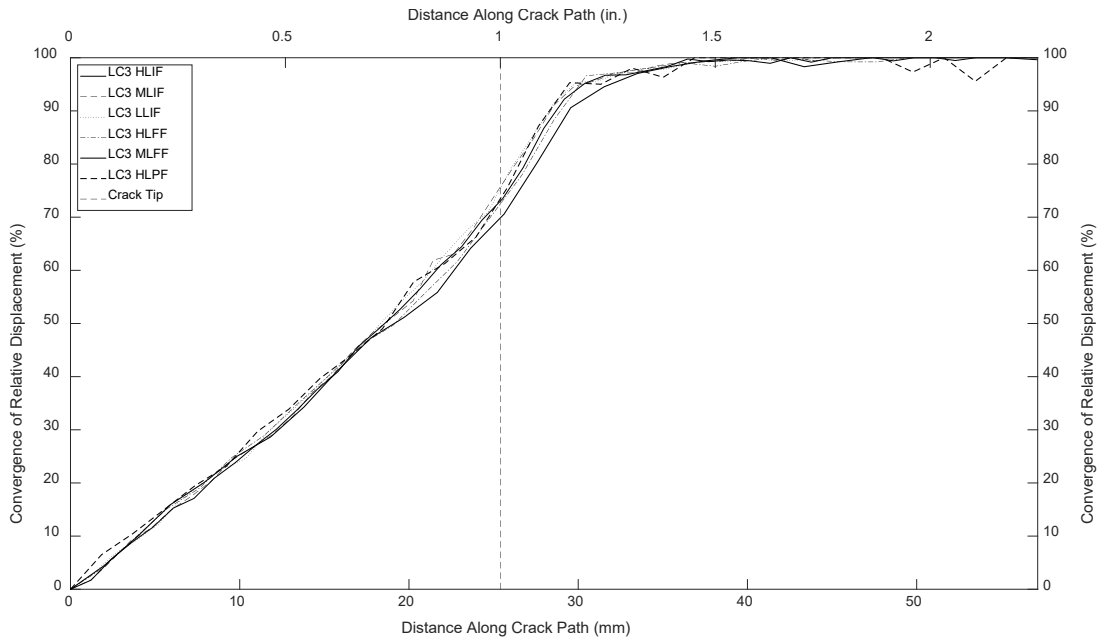distance of 216 mm (8.5 in.) under LC2



Figure A.33 Convergence of relative displacement of a 12.7 mm (0.5 in.) crack with a camera
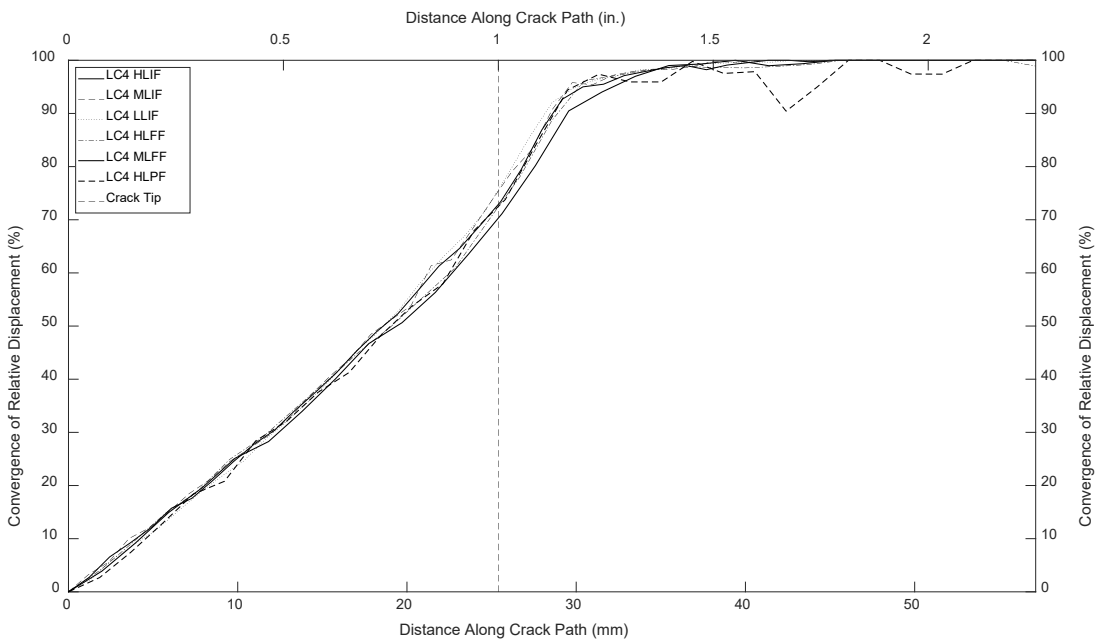distance of 216 mm (8.5 in.) under LC3

Figure A.34 Convergence of relative displacement of a 12.7 mm (0.5 in.) crack with a camera distance of 216 mm (8.5 in.) under LC4
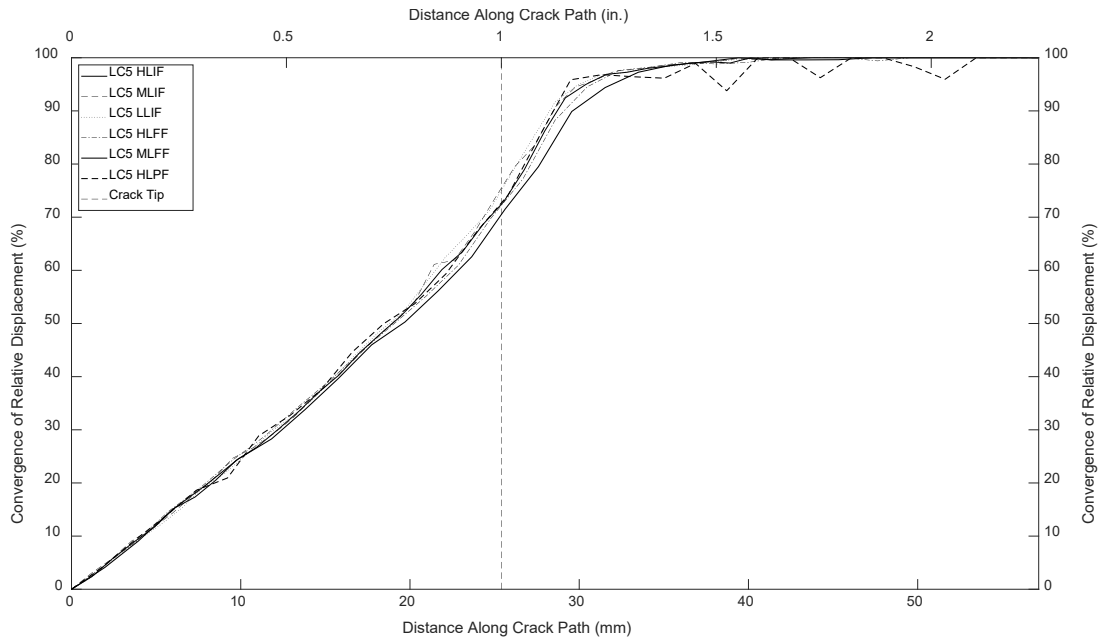


Figure A.35 Convergence of relative displacement of a 12.7 mm (0.5 in.) crack with a camera distance of 216 mm (8.5 in.) under LC5

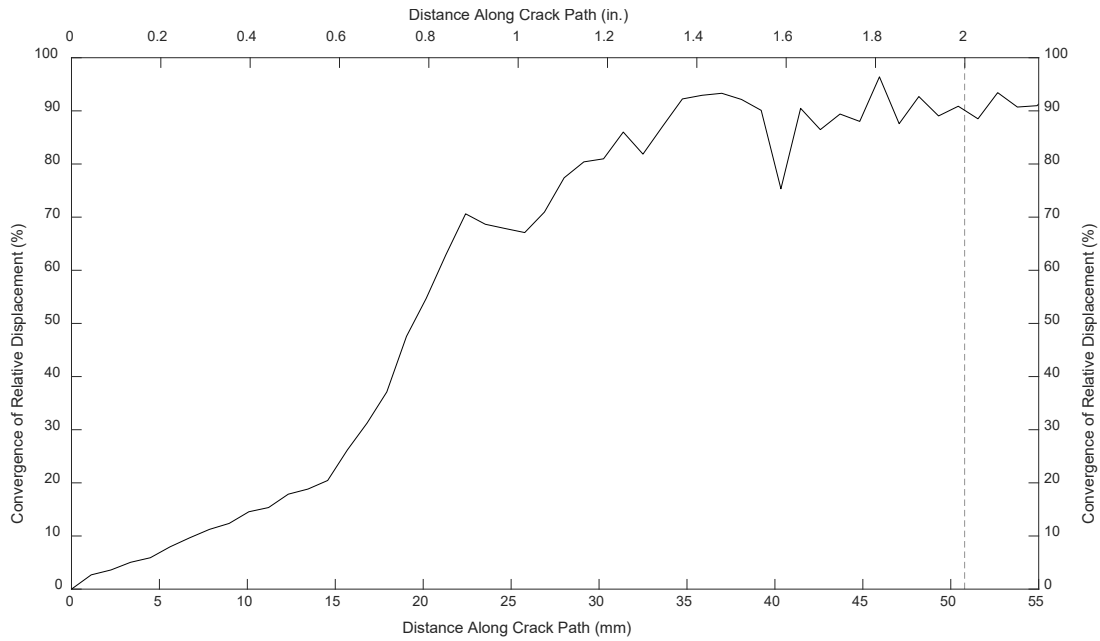Figure A.36 Convergence of relative displacement of a 25.4 mm (1.0 in.) crack with a camera distance of 216 mm (8.5 in.) under LC1



Figure A.37 Convergence of relative displacement of a 25.4 mm (1.0 in.) crack with a camera distance of 216 mm (8.5 in.) under LC2

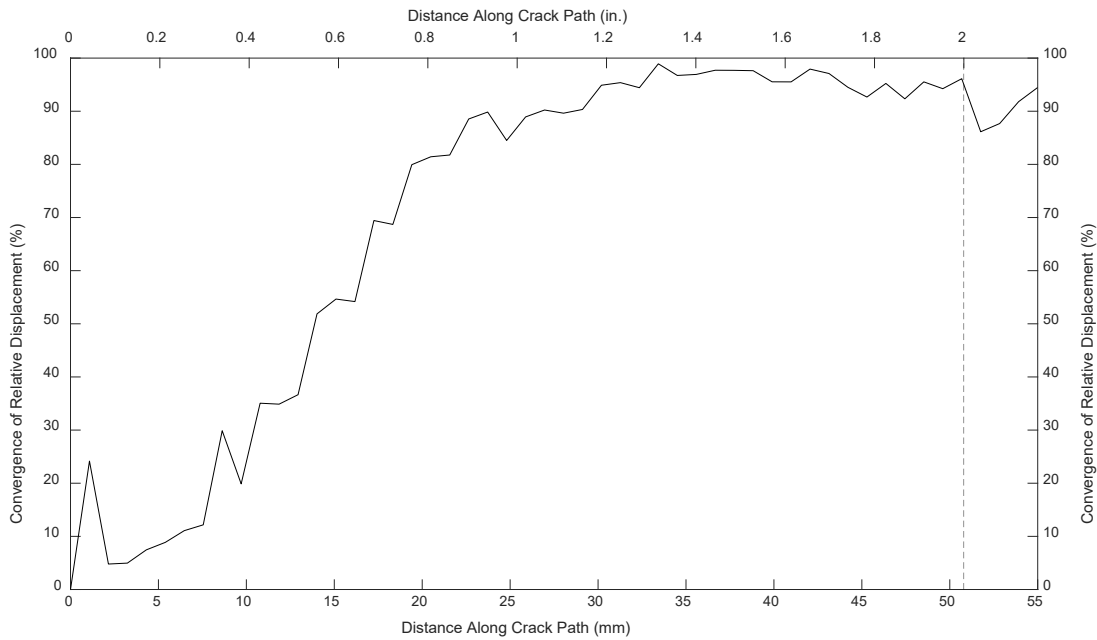Figure A.38 Convergence of relative displacement of a 25.4 mm (1.0 in.) crack with a camera distance of 216 mm (8.5 in.) under LC3



Figure A.39 Convergence of relative displacement of a 25.4 mm (1.0 in.) crack with a camera distance of 216 mm (8.5 in.) under LC4

Figure A.40 Convergence of relative displacement of a 25.4 mm (1.0 in.) crack with a camera distance of 216 mm (8.5 in.) under LC5

Figures A.41 through A.48 show the plots of convergence of relative displacement for different aperture values and camera to specimen distances. The vertical dotted line represents the 50.8 mm (2.0 in.) crack length.

Figure A.41 Convergence of relative displacement of a 50.8 mm (2.0 in.) crack with a camera distance of 203.2 mm (8.0 in.) and an aperture of f/1.4 under LC5



Figure A.42 Convergence of relative displacement of a 50.8 mm (2.0 in.) crack with a camera distance of 203.2 mm (8.0 in.) and an aperture of f/2.8 under LC5
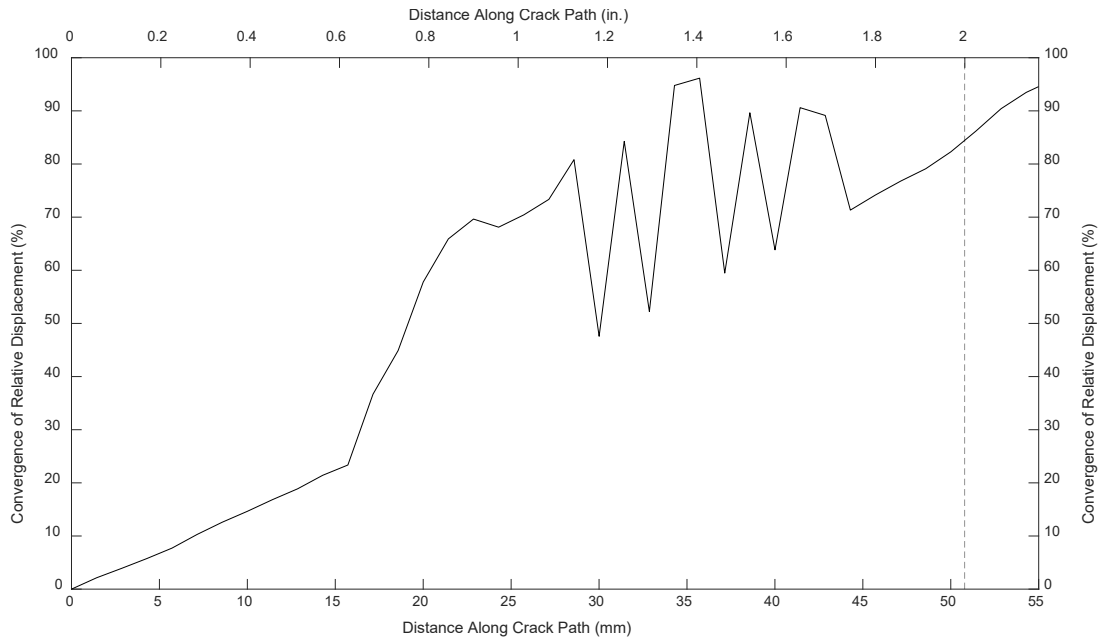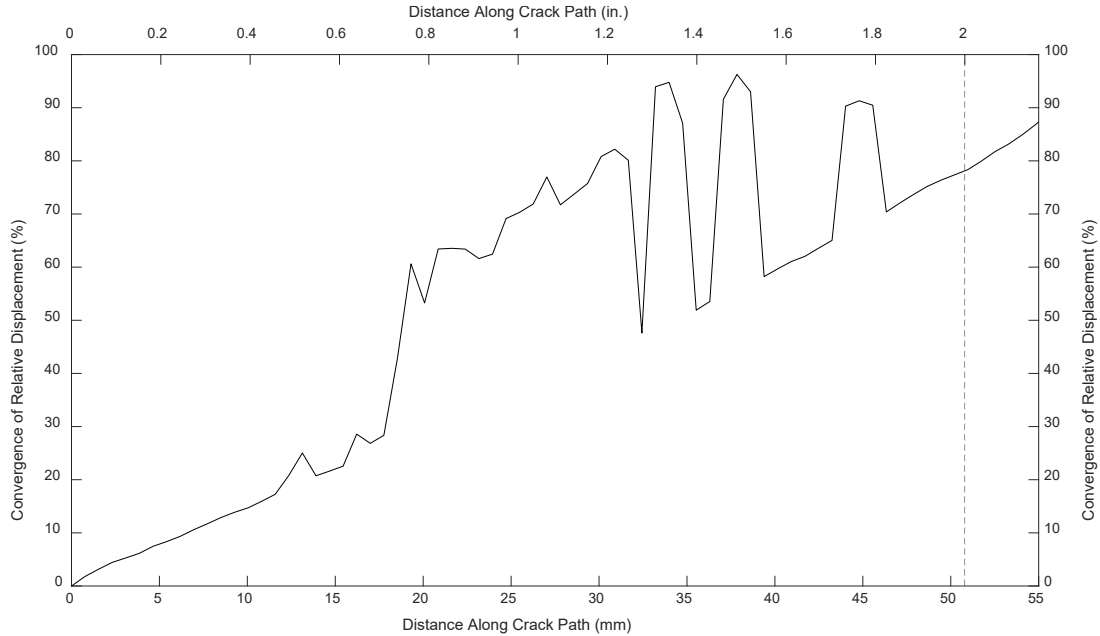
Figure A.43 Convergence of relative displacement of a 50.8 mm (2.0 in.) crack with a camera distance of 304.8 mm (12.0 in.) and an aperture of f/1.4 under LC5



Figure A.44 Convergence of relative displacement of a 50.8 mm (2.0 in.) crack with a camera distance of 304.8 mm (12.0 in.) and an aperture of f/2.8 under LC5
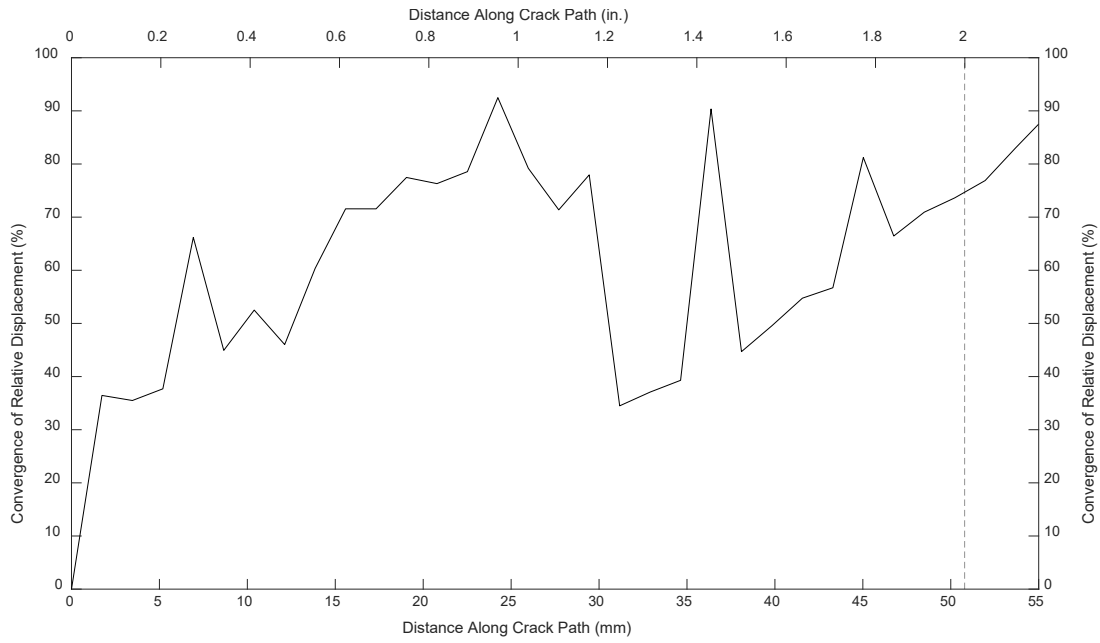
Figure A.45 Convergence of relative displacement of a 50.8 mm (2.0 in.) crack with a camera distance of 457.2 mm (18.0 in.) and an aperture of f/1.4 under LC5
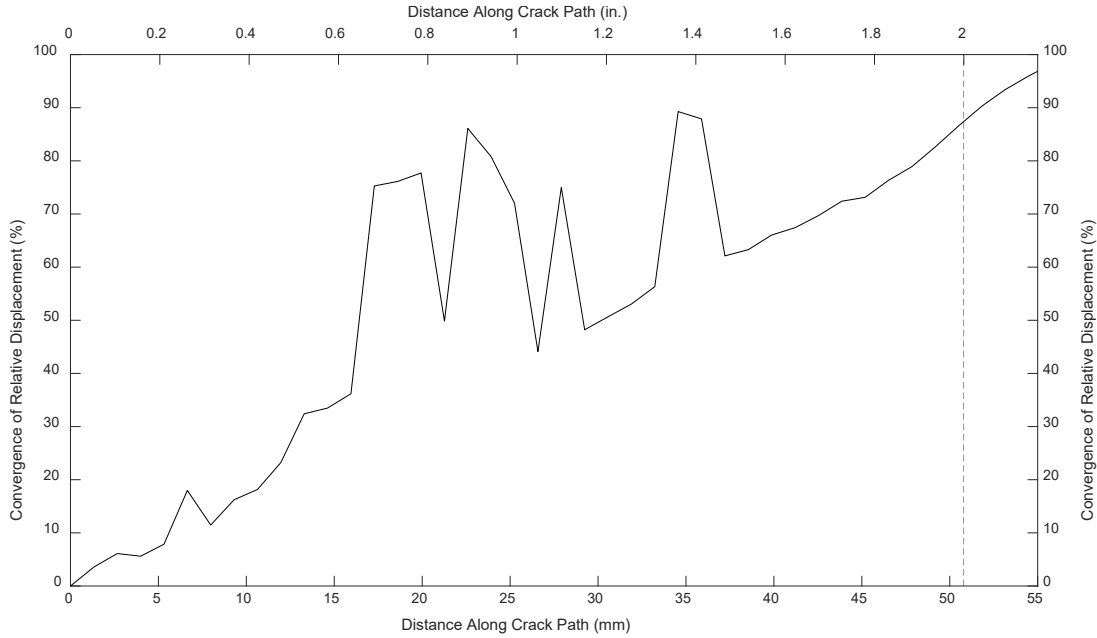


Figure A.46 Convergence of relative displacement of a 50.8 mm (2.0 in.) crack with a camera distance of 457.2 mm (18.0 in.) and an aperture of f/2.8 under LC5
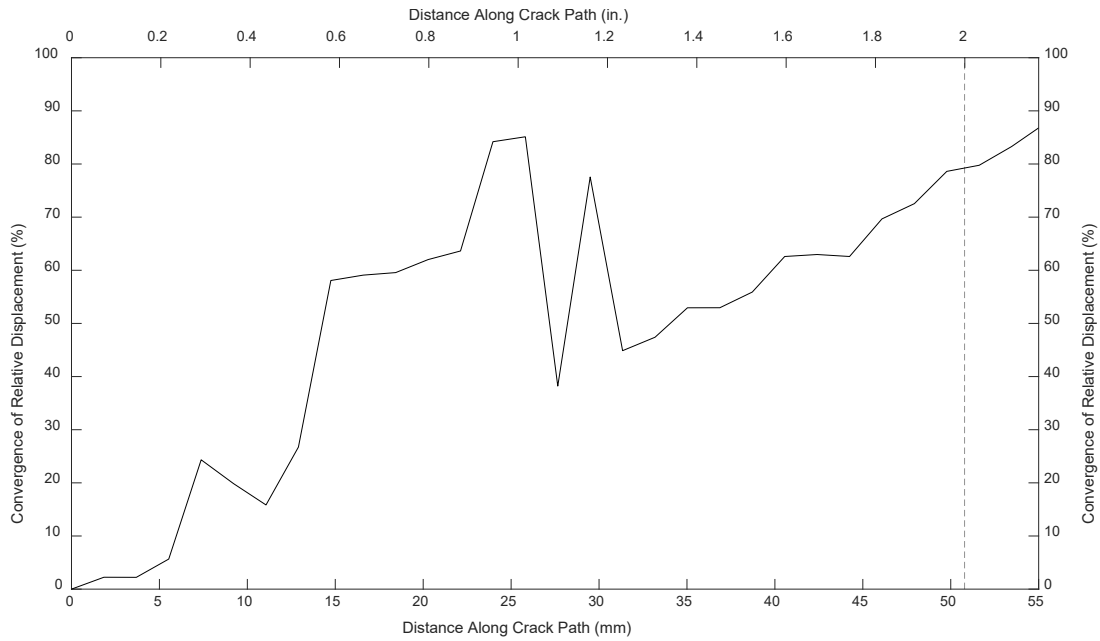
77

Figure A.47 Convergence of relative displacement of a 50.8 mm (2.0 in.) crack with a camera distance of 609.6 mm (24.0 in.) and an aperture of f/1.4 under LC5
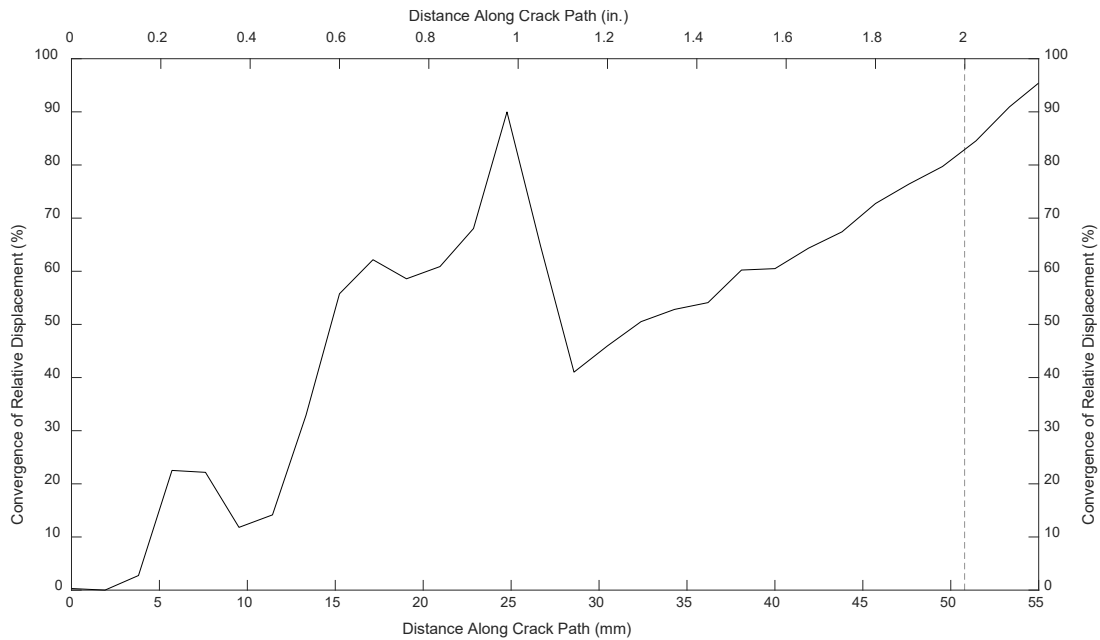


Figure A.48 Convergence of relative displacement of a 50.8 mm (2.0 in.) crack with a camera distance of 609.6 mm (24.0 in.) and an aperture of f/2.8 under LC5